Modelling and Parallel Simulation of Three-Dimensional Ribbing Instability in Symmetric Forward-Roll Coating Processes

by

Mariano Enrique Gurfinkel Castillo

Ingeniero Mecánico, Universidad Simón Bolívar, 1987
Master of Science in Mechanical Engineering, MIT, 1991

Submitted to the Department of Mechanical Engineering
in partial fulfillment of the requirements for the degree of

Doctor of Philosophy

at the

MASSACHUSETTS INSTITUTE OF TECHNOLOGY

December 1994

© Mariano E. Gurfinkel Castillo, 1994. All rights reserved.

The author hereby grants to MIT permission to reproduce and distribute publicly paper and electronic copies of this thesis document in whole or in part, and to grant others the right to do so.

Author ....
Department of Mechanical Engineering
December 13, 1994

Certified by ....
Anthony T. Patera
Professor of Mechanical Engineering, Committee Chairman

Accepted by ....
Ain A. Sonin
Chairman, Departmental Committee on Graduate Students

Eng.

Modelling and Parallel Simulation of Three-Dimensional Ribbing Instability in Symmetric Forward-Roll Coating Processes

by

Mariano Enrique Gurfinkel Castillo

Submitted to the Department of Mechanical Engineering
on December 13, 1994, in partial fulfillment of the
requirements for the degree of
Doctor of Philosophy

Abstract

We analyze the formation, evolution, and spatial persistence of ribbing in coating processes by parallel spectral element simulation of the fully nonlinear, unsteady, three-dimensional, free-surface symmetric forward-roll coating fluid flow problem. The calculations can be interpreted in terms of two well-understood phenomena: the "viscous fingering" instability of a splitting meniscus; and the leveling of viscous films under the effect of surface tension. These two solutions are matched over a transition region of length, L_t, which is on the order of the final coating film thickness. The downstream extent of the leveling region — the distance over which ribs persist, L_ℓ — depends on the fluid properties, the flow conditions, and the wavenumber content of the nonlinear meniscus rib profile.

We present the numerical methods used for our simulations of unsteady highly deformed two-dimensional and three-dimensional free-surface problems; representative results for the evolution of the coating flow from perturbed unstable two-dimensional steady states to stable three-dimensional ribbed steady states; and detailed descriptions of stable three-dimensional ribbed steady states for moderate and highly supercritical capillary numbers, Ca, and for different spanwise periodicity lengths, λ. The model and numerical calculations are consistent with reported experimental observations and linear stability analysis.

Committee: Prof. Anthony T. Patera (Chair)

Prof. Robert A. Brown

Prof. Ain A. Sonin

Acknowledgments

I would like to express my gratitude to Prof. Anthony T. Patera for providing me the opportunity to perform my doctoral research under his guidance. There is much that I learned under his tutelage.

I would also like to acknowledge the many insightful and encouraging comments from the other members of my committee Prof. Robert Brown and Prof. Ain Sonin, and from other members of the Fluid Mechanics Laboratory, Prof. Ascher Shapiro, Prof. Ronald Probstein, Prof. Roger Kamm, Prof. C. Forbes Dewey, Dr. Mark Johnson, and Prof. Doug Hart. I would like to acknowledge the many contributions of Dr. Lee Ho, Dr. Einar Rønquist, Dr. Ed Bullister, and Prof. Paul Fischer.

During my tenure in the Fluid Mechanics Laboratory and more generally at MIT, I have interacted with many. The ever present Dr. Vasan Venugopalan and the answer men: Dr. George Celniker and Dr. Joseph Deck, always available. Kind words go to: Dr. Manuel Ernani Cruz, soon to be Dr. Serhat Yeşilyurt, Dr. Chahid Ghaddar, and all the other members of the Fluid Mechanics Lab (Edwin (some day I'll get it) Ozawa, Richard (what to do in Venezuela) Jacobs, Arthur (what excuse for not running do you have today) Sit, Dr. Fuquan (epa chamo!) Gao, Stefano (basically) Schiaffino, Chunhai (what-sub) Wang, Gregg (welfare) Duthaler, Frank (ride my bike like a crazy man) Espinosa, Barbara (check if Roger is looking) Hamer, mother Kathy, James (Camel) Shin, Naomi (MegaWoman) Chesler, Jim (red-beard) McGrath, Sanjay (four straight) Patel, Dave (Doom, MFD) Danitz, John (Mr. Doom) Dzenitis, Amit (phone call is for you) Dhadwal and all the newer kids Matteo Pedercini, John Otto, Marius Parachivoiu, Hugo Ayala, and those I forget to mention...), that made the years in and out of the fluids lab bearable. A special mention goes to Greta Ward and Dick Fenner for the good laughs and the help.

This work was supported by Fundación Gran Mariscal de Ayacucho (Venezuela), by Intevep S. A., an affiliate of Petróleos de Venezuela, by the Advanced Research Projects Agency under Grant N00014-91-J-1889, and by the Office of Naval Research under Grants N00014-90-J-4124 and N00014-89-J-1610.

To the constants in my life:
my father Mariano Gurfinkel M.,
my mother Laura Castillo de Gurfinkel,
my brother Bernardo José Gurfinkel Castillo,
and my love Rukmani Persaud Ramdharry.

Contents

1 Introduction **23**

1.1 Previous Work 24

1.2 Objectives 32

2 Problem Formulation **35**

2.1 Problem Description 35

2.2 Governing Equations 37

2.2.1 Boundary Conditions at Inflow and Outflow 39

2.3 Governing Parameters 39

3 Nonlinear Modelling of Ribbing **43**

3.1 Description of Mechanism 43

3.2 Model Components 46

3.2.1 Leveling of a Viscous Film 47

3.2.2 Transition from Ribbing to Leveling 52

3.3 Approach to the Steady Ribbed State 54

3.4 Summary 55

4 Numerical Methods for Two-Dimensional Flows **57**

4.1 Numerical Procedure 57

4.1.1 Special Treatment of Boundary Condition at Inflow 59

4.2 Remeshing 60

4.3 Extension of Remeshing: Continuation 69

5 **Numerical Methods for Three-dimensional Flows** **71**
5.1 Numerical Methods 71
5.1.1 Treatment of Boundary Condition at Inflow 72
5.1.2 Treatment of Boundary Condition at Outflow 73
5.1.3 Domain Decomposition and Downstream Extent 74
5.2 Remeshing Procedure 74
5.3 Numerical Procedure 79
5.4 Extensions of Remeshing Procedure 81
5.4.1 Mesh Adaptation 81
5.4.2 Continuation 82
5.4.3 General Mesh Refinement 86
5.4.4 Limitations 86
5.5 Limitations of Numerical Methods 87

6 **Two-dimensional results** **89**

7 **Three-dimensional results** **99**
7.1 Nonlinear Evolution to Steady Ribbed States 99
7.1.1 Comparison with Linear Stability 99
7.1.2 Meniscus Evolution Towards the Steady State 101
7.2 Properties of the Steady Ribbed State 107
7.2.1 Meniscus Geometry and Downstream Ribs 109
7.2.2 Transition of Flow Fields: Helical to Leveling 110
7.2.3 Leveling of Ribs 111
7.3 Steady Ribbed States 116
7.3.1 Moderately Supercritical Steady Ribbed States 117
7.3.2 Multiplicity of Steady Ribbed States 122
7.3.3 Highly Supercritical Steady Ribbed States 126
7.3.4 Nonlinear Mode Interaction 126
7.3.5 The Limit $\lambda \to \infty$ and End Effects 129
7.3.6 Transition Region and Leveling of Ribs: Revisited 131

8 Conclusions **133**

8.1 Guidelines for Future Work 134

List of Figures

1-1 Schematic of a forward-roll film coating device: two rollers of diameter D^*, counter-rotating at angular speed ω^*, entrain fluid of viscosity μ^*, density ρ^*, and surface tension σ^*, through a metering gap of width H^*. 24

1-2 Lubrication theory approximations for the two-dimensional domain: (a) Original geometry; (b) geometry resulting from "matching" two one-dimensional flow regions proposed by Pearson[50] and (c) "parabolic" meniscus region proposed by Pitts & Greiller[51] 25

1-3 Schematic of the growth (or decay) of a disturbance on an interface with a positive (negative) normal pressure gradient. 30

1-4 Schematic of the dependence for a fixed geometry, D^*/H^*, of the eigenmode growth rate, γ^*, on the eigenmode wavenumber, $\beta = \pi H^*/\lambda^*$, for: subcritical ($Ca < Ca_c$), critical ($Ca = Ca_c$), and supercritical ($Ca > Ca_c$) capillary numbers. 31

2-1 Two-dimensional domain Ω^* and boundaries: $\partial\Omega_1^*$, inflow; $\partial\Omega_2^*$, roller; $\partial\Omega_3^*$, outflow; $\partial\Omega_4^*$, free surface; and $\partial\Omega_5^*$, symmetry. 36

2-2 Three-dimensional domain Ω^* and boundaries: $\partial\Omega_1^*$, inflow; $\partial\Omega_2^*$, roller; $\partial\Omega_3^*$, outflow; $\partial\Omega_4^*$, free surface; and $\partial\Omega_5^*$, symmetry. 36

3-1 Schematic showing regions of ribbing flow geometry and flow field: I Meniscus; II Transition; III Leveling Film; IV Leveled Film. 44

3-2 Pressure distribution along the symmetry plane for a flooded roller pair. The negative pressure at x_s is due to the free-surface-curvature induced pressure jump. 44

3-3 Characteristic flow field generated near a free-surface disturbance subject to a positive pressure gradient normal to the interface. The fluid moves away from the troughs toward the crests. 45

3-4 Leveling of a thin viscous film ($h_o^* \ll \lambda^*$). The main flow is in the (r^*, z^*) plane (r^* is normal to the surface of the roller), driven by surface-tension-induced pressure gradients in the z^* direction. 48

3-5 Time constant associated with the surface-tension-driven leveling of a disturbance on a viscous film as a function of the wavenumber β_f. . 51

3-6 Schematic of characteristic flow fields: (a) meniscus region, (b) leveling region. 54

4-1 Example of interruption of solution procedure during evolution from (a) one steady state ($D = 200$, $Ca = .1$) to a new desired steady state ($D = 200$, $Ca = 1$) due to a (b) greatly distorted mesh with a vanishing Jacobian. 61

4-2 Representative information of mesh template for a two-dimensional domain discretization. 62

4-3 Step R1 of the two-dimensional remeshing procedure applied to the greatly distorted mesh of Fig. 4-1 : extract relevant free-surface information (position of the free surface mesh nodes). 62

4-4 Step R3 of the two-dimensional remeshing procedure: position mesh nodes (a) on the rollers, and (b) on the mid-plane. (To aid in visualization, steps R5 and R6 were also performed.) 63

4-5 Position of internal element-edge nodes relative to the edge boundary nodes: (a) on the rollers, (b) edge template, and (c) on the mid-plane. 65

4-6 Step R4 of the two-dimensional remeshing procedure: discretize the free surface extracted in step R1, and position mesh nodes based on the edge boundary nodes and the downstream position. 66

4-7 Step R6 of the two-dimensional remeshing procedure: Blending algorithm for the position on the internal mesh (collocation) nodes for: (a) near quadrangular element, and (b) high aspect ratio element 67

4-8 Example of remeshing for a not overly deformed domain. The original and final meshes are overlaid. 68

4-9 Remeshing of greatly distorted elements: top–original mesh; bottom–new mesh. 68

4-10 Remeshing-continuation for a change in roller separation. 69

5-1 Typical three-dimensional discretization of an extruded two-dimensional domain: sixty spectral elements arranged in four levels. 75

5-2 Discretization template for mesh consisting of 7 levels in the spanwise direction. 76

5-3 Three-dimensional domain and corresponding template slices (6) of the domain consisting of 15 elements in 1 level using interpolants of 5th order. 78

5-4 Schematic of re-entrant rib geometry for which the remeshing procedure can not be used since the rib geometry is not a single valued function of z. 80

5-5 Evolution to a steady three-dimensional ribbed-state displaying the adaptive spanwise template, for $\lambda = 10$, $D = 200$ and $Ca = 3.14$. . . 83

5-6 Example of continuation scheme to generate initial condition for $\lambda = 15$ (b) based on the steady-state for $\lambda = 10$ (a). The initial condition was integrated until a steady-state was achieved (c), for $\lambda = 15$, $D = 200$ and $Ca = 3.14$. 84

5-7 Example of continuation scheme to generate initial condition with two ribs of total spanwise length λ (b) based on the replication of the steady ribbed state for spanwise length $\lambda/2$ (a) for $D = 200$ and $Ca = 3.16$. 85

5-8 Example of continuation used for verification of the steady three-dimensional ribbed-state for $\lambda = 10$, $D = 200$, and $Ca = 3.14$ obtained using $\{15, 6, 5\}$ by continuation using a higher resolution, in this case $\{15, 7, 7\}$. 86

6-1 Two-dimensional steady meniscus geometries as the rollers are brought closer together: for (a) $D = 40$, (b) $D = 200$, and (c) $D = 1000$, as a function of capillary number: $Ca = .0316$, .1, .316, 1, 3.16, 100. . . . 90

6-2 Two-dimensional steady meniscus geometries for equal gaps using different rollers: for (a) $D = 40$, (b) $D = 200$, and (c) $D = 1000$, as a function of capillary number: $Ca = .0316$, .1, .316, 1, 3.16, 100. . . . 91

6-3 Characteristic flow fields: (i) $Ca = .1$ – recirculation zone, (ii) $Ca = 1$ – no recirculation zone, for (a) $D = 40$, (b) $D = 200$, and (c) $D = 1000$. 92

6-4 Two-dimensional steady meniscus geometry for full domain – no imposed symmetry – as a function of the capillary number $Ca = .05 \rightarrow 100$ and $D = 200$. 93

6-5 Non-dimensional volume flowrate, Q, as a function of Ca for $D = 40$ ($\diamond$), $D = 200$ ($\square$), and $D = 1000$ ($\circ$). 95

6-6 Film split location, x_s^{2D}, as a function of $Ca = .0316$, .1, .316, 1, 3.16, 100 for $D = 40$ ($\diamond$), $D = 200$ ($\square$), and $D = 1000$ ($\circ$). 95

6-7 Position of first stagnation point downstream from nip, x_o^{2D}, as a function of Ca for $D = 40$ ($\diamond$), $D = 200$ ($\square$),and $D = 1000$ ($\circ$). 96

6-8 Film split location, x_s^{2D}, as a function of Ca for $D = 200$: this study $\diamond$; Coyle et al[12] $\times$. First stagnation point downstream from nip, x_o^{2D}: this study $\square$, Coyle et al[12] $+$. 97

7-1 Evolution of the meniscus amplitude at the midplane, measured by A_s (∘) for $D = 40$, $Ca = 15$, and $\lambda = 9$, from the slight perturbation to the unstable two-dimensional steady state geometry. A least squares fit of the data for $t \in [2, 18]$ results in a growth rate of $\gamma = .0107$ as indicated by the solid line which is in agreement with that reported by Coyle et al[14] . The growth of the disturbance as it approaches the steady state determined using a least squares fit is given by .0292 in the interval $t \in [15, 40]$ and is in agreement with the value of .0233 given by Eq. (3.16). The resolution used to obtain this result was $\{15, 4, 5\}$. 102

7-2 Evolution of the meniscus profile at the midplane, $\partial\Omega_4 \bigcap \partial\Omega_5$, for $D = 200$, $Ca = 5$, and $\lambda = 15$, from the slight perturbation to the unstable two-dimensional steady state position $x_s^{2\mathrm{D}}$, to the three-dimensional stable steady state: $t = 0$, 20, 30, 40, 50, 58.4, 61.6, 64.2. 104

7-3 Time evolution from the perturbed unstable two-dimensional steady state profile to the three-dimensional stable steady state, for $D = 200$, $Ca = 5$, and $\lambda = 15$, of the meniscus profile amplitude at the midplane, $A_s = \left(\max x_s^{3\mathrm{D}} - \min x_s^{3\mathrm{D}}\right)/2$, and of the first three Fourier modes of the profile A_m, associated with $\beta = m\,2\beta_c = m\pi/\lambda$ for $m = 1, 2, 3$. (Note the fluctuation near the steady state is due to a remesh from six to seven levels.) 106

7-4 Evolution to a steady three-dimensional ribbed-state for $\lambda = 10$, $D = 200$, and $Ca = 3.14$ obtained using "high" resolution throughout the simulation, $\{15, 7, 7\}$. The steady state is identical to the steady ribbed-state shown in Fig. 5-5 obtained using adaptivity in the z direction allowing for lower resolutions during the transients. 108

7-5 View of spanwise periodic stable three-dimensional steady ribbed free-surface geometry for $D = 200$, $Ca = 5$, and $\lambda = 15$. 109

7-6 Steady free-surface profiles for $D = 200$, $Ca = 5$, and $\lambda = 15$, as a function of downstream position: $\theta = 12°$, $13°$, $14°$, $15°$, $16°$, $17°$, $18°$, $19°$. (Note that the sharp profile for $\theta = 12°$ is an artifact of the radial projection.) 111

7-7 Evolution of rib amplitude A (○) for $D = 200$, $Ca = 5$, and $\lambda = 15$, as a function of the roller angle θ. The effect of the outflow boundary condition is clear: $A \rightarrow 0$ as $\theta \rightarrow \theta_{\partial\Omega_3} \cong 22.63°$. 112

7-8 Steady free-surface (or on $\partial\Omega_5$) spanwise velocity, u_3, profiles at different downstream positions for $D = 200$, $Ca = 5$, and $\lambda = 15$: $\theta = 9°$, $10°$, $11°$, $13°$, $15°$. 112

7-9 Characteristic spanwise velocity, u_3, contours for $D = 200$, $Ca = 5$, and $\lambda = 15$, for: (a) Meniscus region, $\theta = 11°$; (b) Transition region, $\theta = 13°$; (c) Leveling Region, $\theta = 15°$. Legend: Grey $u_3 > 0$; Black $u_3 < 0$; arrows indicate direction of flow. 113

7-10 Dependence of rib amplitude A (○), and of the amplitude of the profile Fourier modes with wavenumber $\beta_{f_{\mathrm{IV}}} = m\,2\,\pi\,f_{\mathrm{IV}}\lambda = m\,2\,f_{\mathrm{IV}}\,2\,\beta_c$, $m =$ 1 (◇) , 2 (□) , 3 (△) , and 4 (▽) , as a function of roller angle θ for $D = 200$, $Ca = 5$, and $\lambda = 15$. 114

7-11 Leveling region length, L_ℓ, for the rib, (○), and the first four Fourier modes of the rib profile associated with wavenumbers $\beta_{f_{\mathrm{IV}}} = m\,\frac{2\pi f_{\mathrm{IV}}}{\lambda} = m\,2\,f_{\mathrm{IV}}\,2\,\beta_c$, $m = 1$ (◇) , 2 (□) , 3 (△) , and 4 (▽) for $D = 200$, $Ca = 5$, and $\lambda = 15$. 115

7-12 Steady state profiles of $\partial\Omega_4 \bigcap \partial\Omega_5$ for $D = 200$, $\lambda = \lambda_c = 30$ and $Ca =$ .5, .75, 1, 1.77, 3.16, and 5. The ribs exhibit increasing amplitude, A_s, and harmonic content with increasing Ca (roller velocity). 118

7-13 Amplitude of the Fourier modes of the steady-state profiles of $\partial\Omega_4 \bigcap \partial\Omega_5$ for $D = 200$, $\lambda = 30$, and $Ca = .5$ (○), .75 (◇), 1 (□), and 1.77 (▽) as a function of the corresponding Fourier mode wavenumber $\beta = m\,\beta_c$. 118

7-14 Amplitude of the Fourier modes of the steady-state profiles of $\partial\Omega_4 \bigcap \partial\Omega_5$ for $D = 200$, $\lambda = 30$, and $Ca = 3.16$ (○) and 5 (◇) as a function of the corresponding Fourier mode wavenumber $\beta = m\,\beta_c$. 119

7-15 Steady state profiles of $\partial\Omega_4 \bigcap \partial\Omega_5$ for $Ca = .5$, $D = 200$, $\lambda = \frac{30}{2^{n-1}}$, and $z \in [0, \lambda]$ for $n = 1, \ldots, 3$. 120

7-16 Steady state profile of $\partial\Omega_4 \bigcap \partial\Omega_5$ for $D = 200$ and $Ca = .5$ for $\lambda = 2\,\lambda_c = 60$ (solid line) and initial condition based on an intermediate unsteady-state for $\lambda = \lambda_c = 30$ (dashed line). The profile was obtained by replicating the $\lambda = \lambda_c = 30$ geometry and translating it to fit the domain of depth $\lambda = 60$. 121

7-17 Steady-State profiles of $\partial\Omega_4 \bigcap \partial\Omega_5$ for $Ca = .75$, $D = 200$, $\lambda = \frac{30}{2^{n-1}}$, and $z \in [0, \lambda]$ for $n = 1, \ldots, 3$. 123

7-18 Steady-State profiles of $\partial\Omega_4 \bigcap \partial\Omega_5$ for $Ca = 1$, $D = 200$, $\lambda = \frac{30}{2^{n-1}}$, and $z \in [0, \lambda]$ for $n = 1, \ldots, 4$. 123

7-19 Steady-State profiles of $\partial\Omega_4 \bigcap \partial\Omega_5$ for $Ca = 1.77$, $D = 200$, $\lambda = \frac{30}{2^{n-1}}$, and $z \in [0, \lambda]$ for $n = 1, \ldots, 4$. 124

7-20 Steady state profile of $\partial\Omega_4 \bigcap \partial\Omega_5$ for $D = 200$ and $Ca = .5$ for $\lambda = \lambda_c = 30$ (solid line) and initial condition based on an intermediate unsteady-state for $\lambda = \lambda_c/2 = 15$ (dashed line). The profile was obtained by replicating the $\lambda = \lambda_c = 15$ geometry and translating it to fit the domain of depth $\lambda = 30$. 125

7-21 Steady-State profiles of $\partial\Omega_4 \bigcap \partial\Omega_5$ for $Ca = 3.16$, $D = 200$, $\lambda = \frac{30}{2^{n-1}}$, and $z \in [0, \lambda]$ for $n = 1, \ldots, 5$. 127

7-22 Steady-State profiles of $\partial\Omega_4 \bigcap \partial\Omega_5$ for $Ca = 5$, $D = 200$, $\lambda = \frac{30}{2^{n-1}}$, and $z \in [0, \lambda]$ for $n = 1, \ldots, 5$. 127

7-23 Leveling region length, L_ℓ, of the Fourier modes of the rib profile as a function of spanwise wavenumber, $\beta_{f_{\rm IV}} = \frac{2\pi\, f_{\rm IV}}{\lambda}\, m$, for $D = 200$, $\lambda = 30/2^{n-1}$, and capillary number $Ca = 1$, $n = 1$ (◎), 2 (◈), 3 (⧈), 4 (◬), and $Ca = 5$, $n = 1$ (○), 2 (◇), 3 (□), 4 (△), 5 (▽). 132

List of Tables

4.1 Position of element-edge boundary nodes: (a) on the rollers, and (b) on the mid-plane. 64

4.2 Position of element-edge boundary nodes on the free surface ($\partial\Omega_4$). . 66

5.1 Templates for the z position of the element-edge boundary nodes as a function of the number of levels: (a) 2 levels, (b) 3 levels, (c) 4 levels, (d) 5 levels, (e) 6 levels, (f) 7 levels, (g) 8 levels. 77

6.1 Flowrate, Q, and position of the splitting meniscus, x_s^{2D}, in the limit of $Ca \gg 1$. 96

7.1 Transition length, L_t, for the spanwise velocity profile and that of the individual Fourier modes of the spanwise velocity profile, L_{t_m}, of wavenumber $\beta = m\pi/15$ and $m = 1, \ldots, 5$ for $D = 200$, $Ca = 5$, and $\lambda = 15$. 110

Chapter 1

Introduction

The coating of continuous webs is an important manufacturing process which finds wide application in the photographic and publishing industries. Although much effort is devoted to developing and studying processes for the production of uniform films, a major cause of defects, the three-dimensional hydrodynamic phenomenon known as "ribbing," or "ribbing line instability," is not yet completely understood. Ribbing is characterized by a spanwise waviness of the film free surface[1, 14, 51, 59] that extends downstream with the web, and in most applications, renders the finished product useless.

This thesis studies ribbing in the symmetric forward-roll coating device depicted in Fig. 1-1. In the forward-roll coating process, two counter-rotating rollers entrain and meter fluid onto a web. During normal operation, a continuous uniform film is produced; however, if the speed of rotation of the rollers or the viscosity of the fluid is increased, or the surface tension of the fluid-gas interface is decreased, ribs appear and persist downstream on the film[14, 51, 59]. The rotating speeds for which ribbing is encountered in symmetric forward-roll coating are un-economically slow and thus other industrial coating processes have been developed. These other processes[8, 13, 6, 10, 11, 31, 34, 42, 43, 45, 52, 59, 4, 19, 27, 32] may also exhibit ribbing, but at higher coating speeds; we choose to study forward-roll coating since it does not involve the analysis of static or dynamic contact lines[44, 24, 69, 22, 21, 23, 17, 30, 39, 34, 40, 61, 60, 55, 29] , and ribs are readily obtainable.

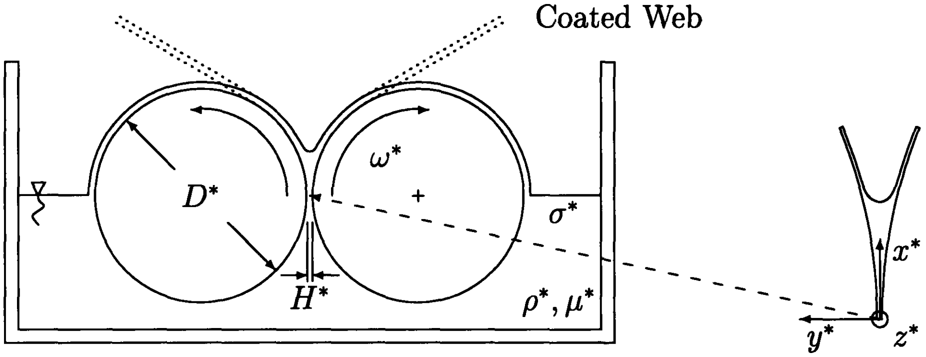

Figure 1-1: Schematic of a forward-roll film coating device: two rollers of diameter D^*, counter-rotating at angular speed ω^*, entrain fluid of viscosity μ^*, density ρ^*, and surface tension σ^*, through a metering gap of width H^*.

1.1 Previous Work

Coating processes in general, and ribbing in particular, have been the object of numerous research efforts. Early experimental studies consisted of characterizing the ribs produced during spreading as a function of the clearance between the spreader (roller or wedge) and the coating surface, and the advance speed of the spreader. From the practical point of view, determining the conditions for the onset of ribs proved of greater utility.

Pearson[50] presents an analysis of coating flows in terms of lubrication theory and linear stability theory to explain why some uniform coating flow regimes are unstable. The approach identified two distinct regions of the flow field, the region upstream of the splitting meniscus and the region downstream of the splitting meniscus. The flow field in both regions was assumed one-dimensional; this approximation is equivalent to considering the problem shown in Fig. 1-2 (b). Since the two flow fields do not match, *ad hoc* boundary conditions were put forth in order to solve the two-dimensional (non-ribbing) problem: the meniscus was assumed to form at the first stagnation point downstream of the nip. Based on these approximations, the two-dimensional problem was solved. Pearson[50], then studied the growth of small lateral disturbances

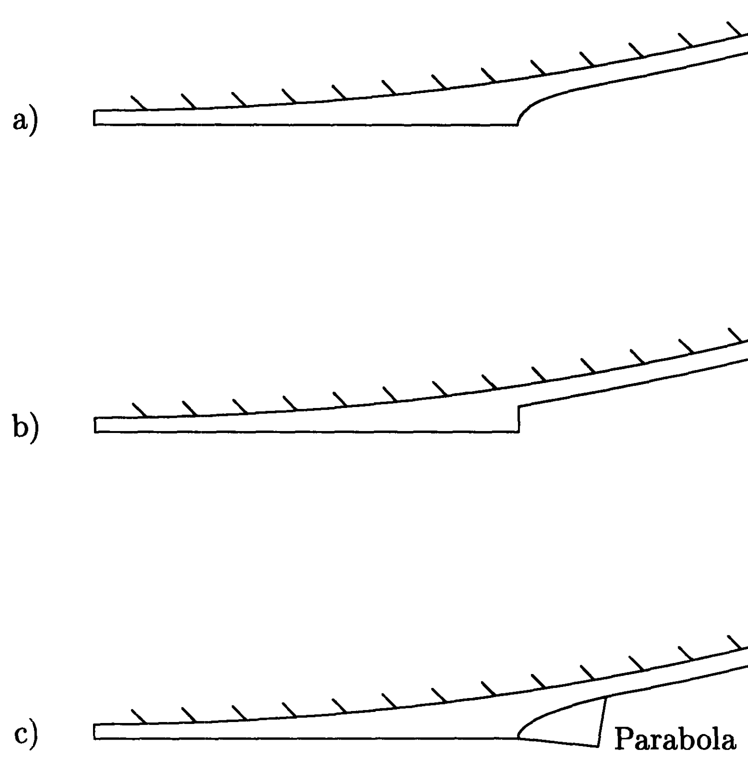

Figure 1-2: Lubrication theory approximations for the two-dimensional domain: (a) Original geometry; (b) geometry resulting from "matching" two one-dimensional flow regions proposed by Pearson[50] and (c) "parabolic" meniscus region proposed by Pitts & Greiller[51].

in order to predict onset, and to attempt to predict the wavenumber of the resulting ribbing. Rough agreement was reported over a limited range of advance speeds despite the crude approximations performed. Greater errors were incurred for high advance speeds for which the "one-dimensional" lubrication theory approximations fail.

Pitts & Greiller[51] studied the flow of thin films between rollers. Naturally, they first studied the "even flow regime" and then tried to determine the critical conditions in which "ripples" first appear. From their experiments, they concluded that, to a very close approximation, the "even flow regime" meniscus is "parabolic over a large portion of its profile" as shown in Fig. 1-2 (c). In their analysis they used this observation to simplify the local meniscus geometry and predict the meniscus location. With regard to ribbing, they studied the effects of a small perturbation to the free surface in the spanwise direction and arrived at a stability criterion in terms of the pressure gradient normal to the free-surface that is a function of the local free-surface in-plane curvature. Using their model for the base states, and using linear stability theory, they arrive at critical values of the governing parameters. They also tried to determine the onset of ribbing through experimental observation for a limited range of the governing parameters and compared them to their analytical predictions. Their predictions for the onset of ribbing have limited success due to the inherent errors of their approximations.

Both Pearson[50] and Pitts & Greiller[51] identified the characteristic capillary number as a governing dynamic parameter. The capillary number, Ca, is defined as $Ca = \mu^* V^* / \sigma^*$ where V^* is the characteristic tangential velocity of the spreader, and μ^* and σ^* are the viscosity of the fluid and the surface tension of the fluid-gas interface (here, and in what follows, superscript * indicates a dimensional quantity). As previously mentioned, the range of Ca studied by Pearson[50] and Pitts & Greiller[51] was limited, and thus their results and conclusions are not general.

Mill & South[47], studying rotating rollers, performed a more thorough experimental attempt at predicting the onset of ribbing covering a slightly wider range of clearance (given in this case by roller separation) than Pitts & Greiller[51]. Attempts at characterizing the ribbed state were also made, though the conclusions are not general. Beyond criticality, they first observe a rapid increase in the wavenumber of the observed ribs. Above $Ca = 2.4$, the wavenumber of the observed ribs became independent of the Ca and varied "solely with geometrical parameters of the system, i. e. roller radius and gap". The results they present include, however, variations of the wavenumber with increasing Ca in the range where they state there are no more variations. For specific coating "windows" given by specific ranges of Ca, stable ribs were not obtained, but rather, a continuous meandering of ribs was observed.

Taylor[65] first studied the deposition of fluid on the wall of a tube when a viscous liquid is blown from an open-ended tube. In this problem, the capillary number, now based on the speed of advance of the interface, is again a governing parameter. Taylor identified three possible flow regimes, two of which exhibit recirculation regions (analogous regimes are observed in symmetric forward-roll coating processes). Taylor[66] then went on to study cavitation of a viscous fluid in narrow passages. The main problem studied was that of eccentric lubricated bearings. Based on creeping flow type approximations, Taylor proposed an expression that relates the flow rate (or final coating thickness) to the pressure at the point of smallest clearance between the rotating cylinders. Based on this result, Taylor determined the position of the meniscus as a function of Ca and the clearance (like Pearson[50] and Pitts & Greiller[51], Taylor too had to assume something at the interface). Taylor identified the difficulty of applying lubrication theory near the fluid-gas interface where the flow field is two-dimensional. This clearly explains the limitations of the work of Pearson[50] and Pitts & Greiller[51] that are based on flow field or boundary condition simplifications based on nearly parallel lubrication flows. With regard to the three-dimensional problem, Taylor identifies two types of cavitation, "separated" cavitation, in which the flow is mainly two-dimensional, and cavitation in which air fingers appear making the flow three-dimensional. The equivalence with ribbing in the free-surface geometries is clearly seen. Taylor also reports on measurements made to determine the onset of the three-dimensional flow regime for the cylindrical apparatus and on the influence of gravitational effects on the onset.

Savage[62], in the context of cavitation in lubrication, studied in detail the different models proposed by others (Swift-Stieber, Hopkins, Taylor, and Coyne & Elrod[15, 16]) to approximate the boundary conditions at the free surface. The boundary conditions are used in conjunction with lubrication theory to predict the location of the free surface and the resulting flow field. Savage does not answer the question of which is the correct model (that is, if any is the correct model), but instead, goes on to study the stability of the cavity-fluid interface without specifying any particular geometry but based on the conditions put forth by Coyne & Elrod[15, 16], which build on the work of Taylor[66]. Savage[62] confirms the original stability result of Pitts & Greiller[51], but then goes one step further and, based on lubrication theory, proposes a more general stability criterion which relates the capillary number to the position of the two-dimensional meniscus. The criterion proposed by Savage[62] for stability of a uniform cavity interface to small perturbations is

$$\frac{d}{dx^*}\left(p^* + \frac{\sigma^*}{a^*}\right) < 0 \tag{1.1}$$

where p^* and a^* are the fluid pressure at the interface and the in-plane radius of curvature of the interface, respectively. The derivative with respect to x^* is also evaluated at the interface. Savage[62] also performs a more complete analysis of steady small-amplitude wavy interfaces which is in good agreement with experimental observations near criticality but grossly overestimates the wavenumber of the observed ribs for greatly supercritical Ca. In later work, Savage[63] revisited the models for the free-surface boundary conditions, determined their range of applicability, and used them to make predictions for forward-roll coating such as coating thickness in the limit of creeping flows.

Dowson & Taylor[19] reviewed, in the context of cavitation in bearings, the formation of cavities, and the boundary conditions that can be applied at the cavity interfaces. They conclude that the Reynolds condition and the separation condition perfected by Coyne & Elrod[15, 16, 19, 63] are the most appropriate for analyses that attempt to predict the location of the interface. The Sommerfeld and Gümbel[19, 63] solution fields do not predict the interface location accurately, but are useful for roughly estimating separating forces in journal bearings. Dowson & Taylor[19] also review the prediction of the number of "streamers" that arise in cavitation and the approximate stability conditions described above.

Gokhale[28] studied the lubrication flow between counter-rotating rollers. By means of barrier functions that bound the pressure from above and below, Gokhale proposed an even tighter stability criterion compared to that of Savage[62], but still could not predict onset since the condition proposed is necessary for stability, but not sufficient.

The description of the mechanism for ribbing, as mentioned above, dates back to the work of Pearson[50] and Pitts & Greiller[51]; other descriptions are given by Savage[62], Ruschak[59], and Coyle[11] and can be readily understood by looking at the criteria for stability. Briefly stated, the splitting meniscus and roller curvature cause a non-negative pressure gradient normal to the meniscus free-surface; from arguments forwarded by Saffman & Taylor[61] to explain viscous fingering, it can then be shown[11, 51, 62] that, in the presence of this positive pressure gradient normal to the free surface, and in the *absence* of surface tension, disturbances to the free surface tend to grow. Figure 1-3 shows a perturbation, of amplitude ε, to an interface where there is a macroscopic pressure gradient normal to the free surface, $\partial p/\partial n$. The pressure difference $p_b - p_c$ indicates if the perturbation will grow or decay; in the absence of surface tension forces, the pressure difference is $p_b - p_c \sim 2\,\varepsilon\,\partial p/\partial n$; thus, the perturbation will grow if $\partial p/\partial n$ is positive. Surface tension, acting through both "in plane" and "out of plane" curvature, will, however, oppose this growth; hence the capillary number as the critical parameter governing the ribbing instability. An instability criterion that incorporates the out-of-plane curvature is reviewed by Coyle[11] and is given by

$$\frac{d}{dx^*}\left(p^* + \frac{\sigma^*}{a^*}\right) - \sigma^*\left(\frac{\pi\, H*}{\lambda^*}\right)^2 > 0 \qquad (1.2)$$

where λ^* is the wavelength of the disturbance, p^* is the fluid pressure at the interface and a^* the in-plane curvature at the interface.

The analogy between ribbing and viscous fingering is readily visualized by considering that air (the less viscous fluid) is blown into the coating fluid (the more viscous fluid) that occupies the space between the rollers and analyzing the problem with a reference frame attached to the interface.

Ruschak[57, 58] and Coyle et al[12] use lubrication theory and matched asymptotic expansions to predict the two dimensional base states in the limit of vanishing gap to roll diameter, $H^*/D^* \to 0$. The use of matched asymptotic expansions allows for the correct imposition of boundary conditions between the distinct flow regions, here divided into inner and outer problems, in contrast to the *ad hoc* matching conditions

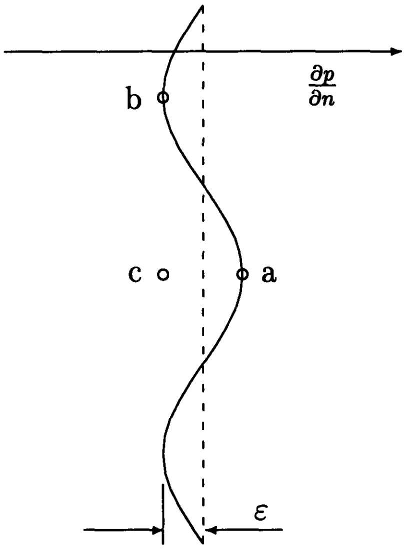

Figure 1-3: Schematic of the growth (or decay) of a disturbance on an interface with a positive (negative) normal pressure gradient.

imposed by Pearson[50], or the simplifications of the meniscus geometry performed by Pitts & Greiller[51]. To obtain the outer problem, the equations are appropriately scaled and the ratio of the gap to the diameter, H^*/D^*, is used as the small parameter for the expansions. Lubrication theory is appropriate for the outer problem since the streamlines are nearly parallel. In contrast, the inner problem remains two-dimensional; the leading order problem reduces to $H^*/D^* \rightarrow 0$, the splitting flow between two parallel plates. The inner problem was solved numerically by Ruschak[57] using the finite element method and then matched to the outer problem.

For arbitrary H^*/D^*, full numerical approaches must be considered due to the two-dimensionality of the flow field and the free-surface-induced nonlinearity. Coyle et al[12] combine the finite-element method and Newton-iteration solution procedure to compute two-dimensional flow geometries and flow fields for forward-roll coating for a wide range of H^*/D^*; their reported results are in very good agreement with experiment.

On the basis of these (correct) two-dimensional states, Ruschak[58] (for small

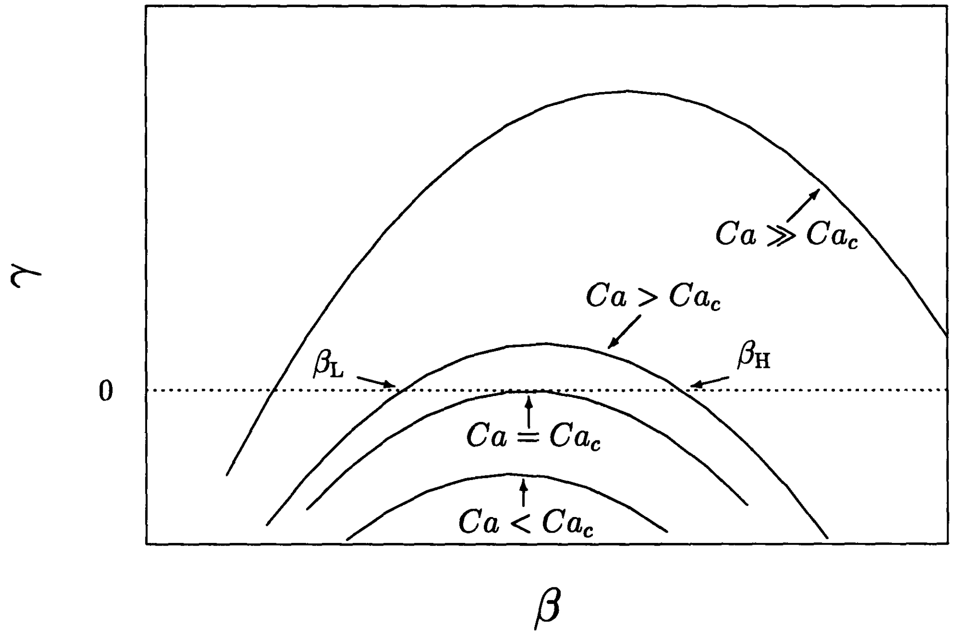

Figure 1-4: Schematic of the dependence for a fixed geometry, D^*/H^*, of the eigenmode growth rate, γ^*, on the eigenmode wavenumber, $\beta = \pi H^*/\lambda^*$, for: subcritical ($Ca < Ca_c$), critical ($Ca = Ca_c$), and supercritical ($Ca > Ca_c$) capillary numbers.

H^*/D^*) and Coyle et al[14] (for general H^*/D^*) present numerical solutions to the unsymmetric eigenvalue problem for the growth rates of infinitesimal three-dimensional disturbances. The stability of two-dimensional base states, for a fixed D^*/H^*, to three-dimensional disturbances of given spanwise wavelength, λ^*, is determined by the capillary number $Ca = \mu^* V^*/\sigma^*$, where μ^*, σ^*, and $V^* = \omega^* D^*/2$ are the viscosity and surface tension of the fluid, and the tangential velocity of the rollers, respectively. The critical capillary number, Ca_c, for a given geometry, D^*/H^*, is defined as the minimum capillary number, Ca, for which the greatest growth rate, γ^*, over all disturbance wavelengths, λ^*, vanishes. The associated critical eigenfunction has a wavelength, λ_c^*, and a wavenumber, β_c, related by $\beta_c \equiv \pi H^*/\lambda_c^*$ (note we nondimensionalize the wavenumber with respect to the half-gap, $H^*/2$). In addition, linear stability theory indicates that, for supercritical capillary numbers, $Ca > Ca_c$, a continuous range of wavenumbers, $[\beta_{\mathrm{L}}(Ca), \beta_{\mathrm{H}}(Ca)]$ is unstable[14], where $\beta_{\mathrm{L}}(Ca)$ and $\beta_{\mathrm{H}}(Ca)$ are low and high wavenumber cutoffs, respectively (see Fig. 1-4). Linear stability theory accurately identifies the onset of ribbing[14, 47, 50, 51, 58] as the growth of infinitesimal three-dimensional disturbances to the two-dimensional steady "base" states. The linear stability results presented by Coyle et al[14] are in very good agreement with experimental observations for the onset of ribbing[14, 47, 51] confirming that the instability (disregarding imperfections such as end effects) is a supercritical bifurcation[20]. Coyle et al[14] present their experimental results combined with the previous experimental results of other investigators and clearly show the limited range of Ca and configurations of the previous studies and their overall agreement in predicting onset.

1.2 Objectives

Despite the agreement between the linear stability analysis of Coyle et al[14] and experimental observations of the onset of ribbing, several important issues remain outstanding. This thesis addresses the following:

1. Previous work can not explain experimental observations of ribs over the entire roller surface, or on the web far downstream from the meniscus. The mechanisms outlined above indicate that the source of the instability (the free-surface normal pressure gradient) is not present on the rolls; indeed, Coyle et al[14] report eigenfunctions which (spatially) decay rapidly in the downstream direction. In addition, the eigenfunctions determined using linear stability analysis do not exhibit the mechanisms required for the dowstream leveling of the finite amplitude ribs as explained in detail in Chapter 3. These results indicate that the presence, or more precisely, spatial persistence, of ribs cannot be explained solely in terms of linear stability arguments.

2. Previous work, in particular linear stability theory, can not address the nonlinear evolution, interaction, and resulting spatial structure of finite-amplitude ribs. The wavenumber content and amplitude of the resulting finite amplitude meniscus disturbances must be determined to study the nonlinear evolution and

spatial structure of the resulting finite amplitude downstream ribs.

Understanding the mechanism for the growth, spatial persistence and, relatedly, the amplitude of ribs is critical to the design of effective coating procedures, and to the selection of optimal operating parameters: it is the persistence of ribs of finite amplitude, and not simply the meniscus-local presence of free-surface waviness, that determines the quality of the finished product.

This thesis proposes numerical methods for the study of the nonlinear evolution and spatial structure of ribs in symmetric forward-roll coating flows and proposes a framework for understanding the formation, evolution, and spatial persistence of ribs that sheds light on the seeming contradictions between previous analytical work and experimental observations. In particular, we formulate the problem in Chapter 2; present the "model" for ribbing in Chapter 3; discuss the numerical methods in Chapter 4; reproduce existing results for two-dimensional forward-roll coating in Chapter 5; present new results for three-dimensional finite amplitude ribs in Chapter 6; and briefly state our conclusions in Chapter 7.

Chapter 2

Problem Formulation

2.1 Problem Description

The symmetric forward-roll coating device depicted in Fig. 1-1 consists of two cylinders of equal diameter D^* separated by a gap H^* counter-rotating at the (same) angular rate ω^*. In the analysis that follows, we consider a reduced problem on the symmetrized domain, Ω^*, shown in Figs. 2-1 and 2-2 for the two-dimensional and three-dimensional cases, respectively. The domain Ω^* has a boundary $\partial\Omega^* = \bigcup_{i=1}^{5} \partial\Omega_i^*$, comprising five parts: $\partial\Omega_1^*$, inflow; $\partial\Omega_2^*$, roller; $\partial\Omega_3^*$, outflow; $\partial\Omega_4^*$, free surface; and $\partial\Omega_5^*$, symmetry. The domain considered extends up to (at inflow) where the cylinders are closest[12] — the nip region — and extends sufficiently downstream of the nip (at outflow) so that the film profile and the pressure become uniform or, at least, change very slowly.

Our assumption (like that of Coyle et al[12, 14]) of symmetry about the $y^* = 0$ plane, $\partial\Omega_5^*$, improves numerical conditioning, decreases the degrees-of-freedom, and reduces the overall computational time; collateral "full domain" numerical calculations (see Chapters 6 and 7) suggest that both the two-dimensional steady states and the nonlinear three-dimensional free surface evolution are, indeed, y^*-symmetric for the range of Ca of interest.

For the three-dimensional analyses, we limit our considerations to domains that are λ^* periodic in the spanwise (z) direction; one periodic cell of the domain is shown

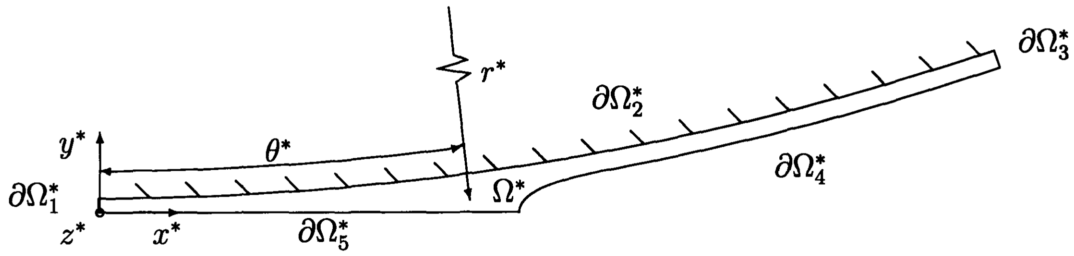
$\partial\Omega_3^*$
r^*
$\partial\Omega_2^*$
y^*
θ^*
$\partial\Omega_4^*$
$\partial\Omega_1^*$
Ω^*
z^*
x^*
$\partial\Omega_5^*$

Figure 2-1: Two-dimensional domain Ω^* and boundaries: $\partial\Omega_1^*$, inflow; $\partial\Omega_2^*$, roller; $\partial\Omega_3^*$, outflow; $\partial\Omega_4^*$, free surface; and $\partial\Omega_5^*$, symmetry.

in Fig. 2-2. A periodic domain of finite length, λ^*, does not permit the study of the complete three-dimensional geometry of a forward-roll coating device; in particular, we can not consider end effects, which might give additional insight into the (imperfect bifurcation[14]) nature of the ribbing instability (See Chapter 7).

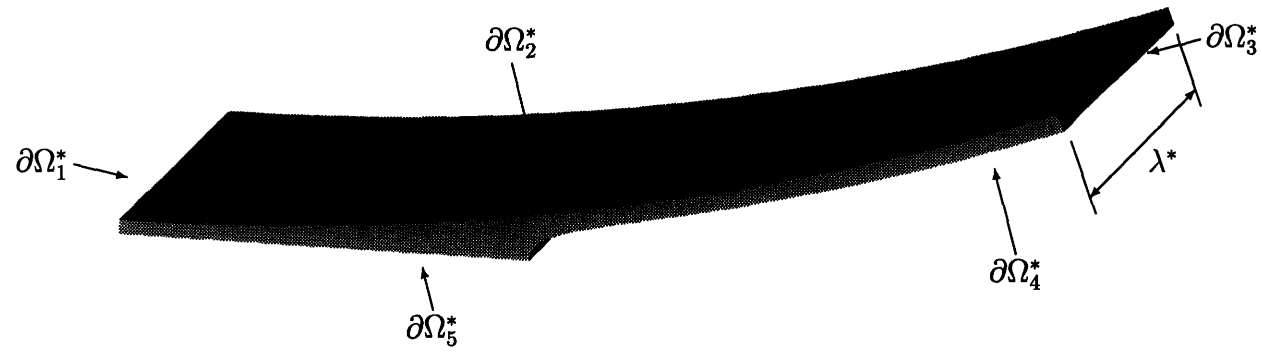
$\partial\Omega_2^*$
$\partial\Omega_3^*$
$\partial\Omega_1^*$
λ^*
$\partial\Omega_4^*$
$\partial\Omega_5^*$

Figure 2-2: Three-dimensional domain Ω^* and boundaries: $\partial\Omega_1^*$, inflow; $\partial\Omega_2^*$, roller; $\partial\Omega_3^*$, outflow; $\partial\Omega_4^*$, free surface; and $\partial\Omega_5^*$, symmetry.

2.2 Governing Equations

We consider the unsteady incompressible creeping flow of a Newtonian fluid of viscosity μ^* and density ρ^* in the time dependent domain Ω^*. The nondimensional (without superscript *) governing equations are then given by

$$Re\, u_{i,t} = -\left(p\right)_{,j}\delta_{ij} + \left(u_{i,j}+u_{j,i}\right)_{,j} \qquad \text{in} \qquad \Omega, \tag{2.1}$$

with boundary conditions

$$\left.\begin{array}{rcl} n_i\left[-p\,\delta_{ij}+u_{i,j}+u_{j,i}\right]n_j & = & p_{\text{nip}} \\ t_i\left[u_{i,j}+u_{j,i}\right]n_j & = & 0 \end{array}\right\} \qquad \text{on} \qquad \partial\Omega_1, \tag{2.2}$$

$$u_i = V\,t_i \qquad \text{on} \qquad \partial\Omega_2, \tag{2.3}$$

$$\left.\begin{array}{rcl} n_i\left[-p\,\delta_{ij}+u_{i,j}+u_{j,i}\right]n_j & = & p_{\text{out}} \\ t_i\left[u_{i,j}+u_{j,i}\right]n_j & = & 0 \end{array}\right\} \qquad \text{on} \qquad \partial\Omega_3, \tag{2.4}$$

$$\left.\begin{array}{rcl} n_i\left[-p\,\delta_{ij}+\left(u_{i,j}+u_{j,i}\right)\right]n_j & = & (1/Ca)\,\kappa \\ t_i\left[u_{i,j}+u_{j,i}\right]n_j & = & 0 \end{array}\right\} \qquad \text{on} \qquad \partial\Omega_4, \tag{2.5}$$

$$\left.\begin{array}{rcl} u_i\,n_i & = & 0 \\ t_i\left[u_{i,j}+u_{j,i}\right]n_j & = & 0 \end{array}\right\} \qquad \text{on} \qquad \partial\Omega_5, \tag{2.6}$$

and periodicity in the spanwise direction for all variables (say ξ),

$$\xi\left(x,y,z,t\right) = \xi\left(x,y,z+\lambda,t\right) \qquad \text{in} \qquad \Omega. \tag{2.7}$$

In addition, the domain Ω is time-dependent, and we thus define a material velocity in order to follow the evolution of the domain Ω. The kinematic condition imposes restrictions on the normal component of the material velocity on the boundary $\partial\Omega_4$; the normal velocity of a material point on the free-surface, $w_i\,n_i|_{\partial\Omega_4}$, must coincide with the corresponding fluid normal velocity, thus $w_i\,n_i|_{\partial\Omega_4} = u_i\,n_i|_{\partial\Omega_4}$. On the other hand, the kinematic condition does not impose restrictions in the tangential direction (we set $w_i\,t_i \equiv 0$ on $\partial\Omega_i$). The reader is referred to more complete descriptions of the possible boundary conditions in the tangential direction in reference[35]. The evolution of the domain is thus governed by:

$$x_{i,t} = w_i \qquad \text{in} \quad \Omega \tag{2.8}$$

with the following (normal) boundary condition imposed by the kinematic condition:

$$\begin{aligned} w_i\, n_i &= u_i\, n_i \quad \text{on} \quad \partial\Omega_4 & (2.9) \\ w_i\, n_i &= 0 \qquad\;\; \text{on} \quad \partial\Omega \setminus \partial\Omega_4 & (2.10) \end{aligned}$$

The previous treatment of the domain gives rise to additional terms that modify Eq. 2.1 which we discuss in Chapter 4.

We use standard Cartesian indicial notation (e.g. $u_{i,j} = \partial u_i/\partial x_j$), where subscript indices range from 1 to 2 or to 3 for the two-dimensional or three-dimensional problem, respectively; κ is twice the mean curvature; n_i is the unit normal on $\partial\Omega$; t_i is the unit tangent (or tangents) on $\partial\Omega$ (in two dimensions, $t_i \times n_i = \hat{z}$); $Re = \rho^*\, V^*\, H^*/\mu^*$ is the Reynolds number; σ^* is the surface tension at the fluid free surface; $Ca = \mu^* V^*/\sigma^*$ is the capillary number; p_{nip} and p_{out} are the pressures imposed at inflow and outflow, respectively; and $V^* = \omega^* D^*/2$ is the tangential speed of the rollers. Length (x_i^*), velocity (u_i^*), time (t^*), and pressure (p^*) are scaled by H^*, V^*, H^*/V^*, and $\mu^* V^*/H^*$, respectively to arrive at their nondimensional counterparts. Both H and V are by definition equal to unity but sometimes are not dropped for clarity.

For future reference, we also introduce several auxiliary coordinates: r and f, to measure the radial position; and s and θ, to measure the downstream position along the rollers. The coordinate r (see Fig. 2-1) measures the distance to the center of the roller, $r = \left(x^2 + (D/2 + H/2 - y)^2\right)^{1/2}$, while f is the distance to the roller surface, $f = r - D/2$. The coordinate θ (see Fig. 2-1) measures position downstream from the nip, $\theta = \arctan\,(x/r)$, while the coordinate s measures the arc length along the roller from the point where the cylinders are closest, $s = r\,\theta$.

2.2.1 Boundary Conditions at Inflow and Outflow

We now discuss the conditions at inflow and at outflow. As regards inflow, we make the simplifying assumption that the region upstream of the nip is flooded[12], and, in addition, that the flow in this region admits adequate approximation by lubrication theory (consistent with the creeping flow assumption in Eq. (2.1)). The pressure at the nip, p_{nip}, is thus only a function of the total volumetric flowrate per unit depth[12, 66]:

$$p_{\text{nip}} = \frac{3}{4}\sqrt{2}\pi \left[1 - \frac{3}{4}Q\right] 2\sqrt{D}, \tag{2.11}$$

where $Q = Q^*/(V^* H^*)$, and Q^* is the total volumetric flowrate per unit depth through the nip. Equation (2.11) must be solved coupled to the fluid flow equations.

Proceeding now to outflow, we note that, sufficiently far downstream of the nip, the film profile and the pressure become uniform. The domain considered extends a finite arclength $s_{\partial\Omega_3}$ along the roller, equivalent to an angle $\theta_{\partial\Omega_3}$; on $\partial\Omega_3$ (that is, at $\theta = \theta_{\partial\Omega_3}$), we impose

$$p_{\text{out}} = \frac{1}{Ca}\frac{2}{D + 1.3\,H}, \tag{2.12}$$

which is an estimate for the pressure jump across the free surface of the uniform film. This boundary condition is asymptotically correct for $D/H \to \infty$ and $s_{\partial\Omega_3} \to \infty$.

2.3 Governing Parameters

In this problem formulation we neglect advection and gravitational terms, since these effects are, first, typically not important, and second, not necessary to explain and study the basic mechanisms of ribbing. In particular, we concentrate on flows which commonly exhibit ribbing and in which inertial effects are negligible, $Re \ll 1$, as is usually the case in configurations that involve extremely viscous fluids (characteristic values are $H^* = 100\,\mu$m, $D^* = .4$ m, $\mu^* = 20$ Pa s, $\rho^* = 950$ Kg/m^3, $\sigma^* = .05$ N/m, $V^* = 1$ m/s, implying $Re = 5 \times 10^{-3}$, see reference [11]). This allows us to drop the advection term, $Re\, u_j\, u_{i,j}$, from the Navier-Stokes equations in arriving at Eq. (2.1). We do not, however, eliminate the unsteady term, $Re\, u_{i,t}$, since the time constant associated with instability evolution is not known *a priori.* As will be seen in Chapter 7, the time constant is such that the temporal dependence of the problem enters primarily through the movement of the physical domain; thus, in retrospect, the $Re\, u_{i,t}$ term could have been safely discarded, yielding a quasi-steady Stokes problem in a time dependent domain. There are, of course, operating conditions for which inertial effects are not negligible. As mentioned previously, we do not consider such regimes[14, 68].

The ratio of gravitational forces to viscous forces, given by the Stokes number $St = \rho^* g^* \left(H^*\right)^2 / \left(\mu^* V^*\right)$, and the ratio of gravitational forces to surface tension forces, given by the Bond number $Bo = St\, Ca = \rho^* g^* \left(H^*\right)^2 / \sigma^*$, are small in the applications that we consider, and thus we do not include gravity effects (here g^* is the acceleration of gravity) even in the limit of moderately large Ca. Neglecting gravitational (and inertial) effects places restrictions on the gap, H^* we do not consider these cases referred to as the wide-gap regime, in which Re, Bo, and St are order unity [68], since for the applications we are interested, H^* remains small and thus inertial and gravitational effects are not important. Since we solve the full two-dimensional (and three-dimensional) problem instead of the lubrication theory based equivalent, we can consider Ca above the limits of applicability of the lubrication theory approximations ($Ca \sim .01$).

The physical problem is governed by three parameters:

$$D = \frac{D^*}{H^*}, \tag{2.13}$$

$$Ca = \frac{\mu^* V^*}{\sigma^*}, \tag{2.14}$$

$$\lambda = \frac{\lambda^*}{H^*}, \tag{2.15}$$

where D is a geometric quantity that measures the relative importance of roller curvature to roller separation, Ca is the ratio of viscous forces to surface tension forces, and λ is the wavelength of the spanwise periodicity. For the two-dimensional problem, only D and Ca are of interest. Values of D and Ca in actual manufacturing processes can span several orders of magnitude, $D \in [50, 50\,000]$ and $Ca \in [10^{-3}, 10^{3}]$. We will only consider those (intermediate) values of D and Ca for which steady-ribs can be readily observed; we will, however, study a range of λ. Considering a specific value of λ provides a lower bound for the possible wavenumber content, and thus limits the possible wavenumber content to $\beta = m\,\pi\,H/\lambda$ for $m = 1, \ldots, \infty$.

Chapter 3

Nonlinear Modelling of Ribbing

3.1 Description of Mechanism

In this chapter we present a framework for understanding ribbing in terms of two well understood physical phenomena: the growth of disturbances on a splitting meniscus [14, 50, 51, 59, 62], and the leveling of a viscous film under the effects of surface tension[41, 46, 48]. Since the flow fields of these two phenomena are not compatible, we "match" the two regimes by means of a transition region. In total, we describe the ribbing flow free-surface geometry and flow field by the four regions shown in Fig. 3-1. A brief summary of each region follows:

I Meniscus: In this region the pressure gradient normal the free surface is great enough for ribs to grow and develop. The flow field is "helical" in nature: the fluid near the free surface moves toward the crests of the ribs and away from the troughs. As described in Chapter 1, the driving force for this flow pattern is a positive pressure gradient normal to the free surface as shown in Fig. 3-2 which drives the spanwise (tangential) flow described before and shown in Fig. 3-3.

II Transition: In this region the flow field of the meniscus is matched to that of a leveling film. The pressure gradient is not great enough to sustain the helical flow field, which rapidly decays, due to the effects of viscosity, towards the leveling solution. The transition region length is of order unity: $L_t = L_t^*/H^* \sim$

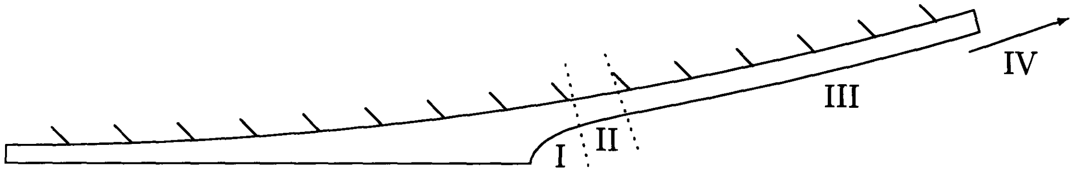

Figure 3-1: Schematic showing regions of ribbing flow geometry and flow field: I Meniscus; II Transition; III Leveling Film; IV Leveled Film.

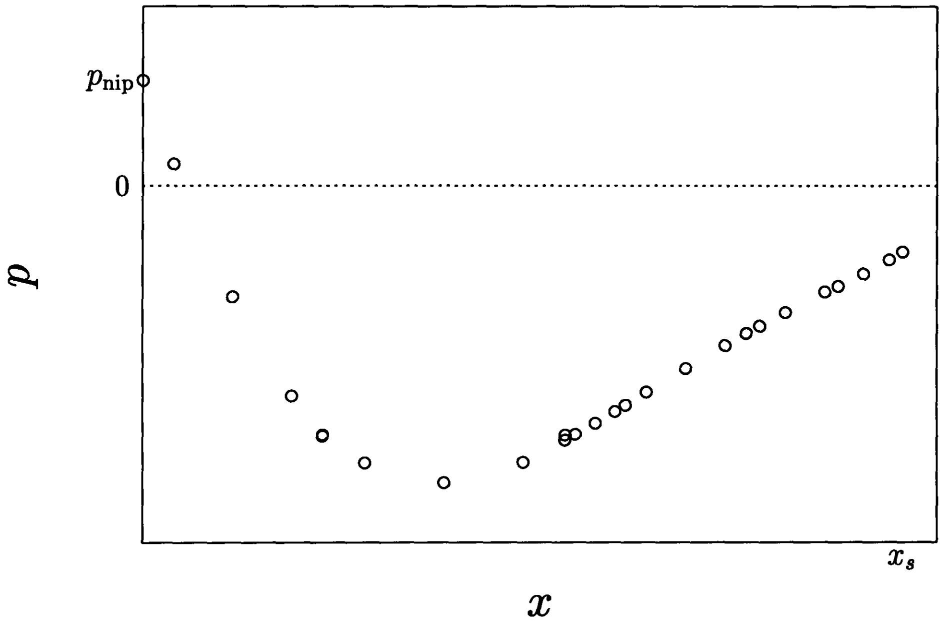

Figure 3-2: Pressure distribution along the symmetry plane for a flooded roller pair. The negative pressure at x_s is due to the free-surface-curvature induced pressure jump.

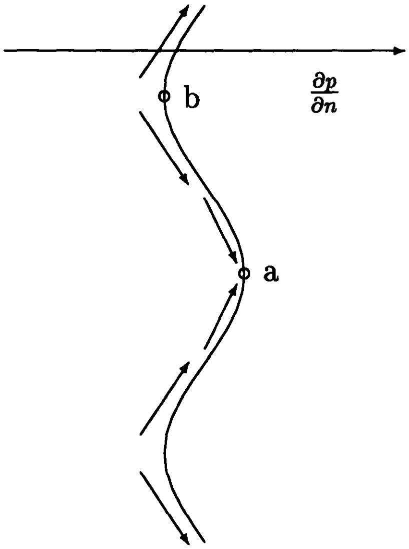
b
$\frac{\partial p}{\partial n}$
a

Figure 3-3: Characteristic flow field generated near a free-surface disturbance subject to a positive pressure gradient normal to the interface. The fluid moves away from the troughs toward the crests.

O(1).

III Leveling Film: In this region there is no appreciable pressure gradient, and thus the ribs level under the effect of surface tension. This region can be extremely long, depending on the wavenumber, β, of the rib disturbance created at the meniscus; the length of this region, $L_\ell = L_\ell^*/H^*$, scales as β^{-4} in the low wavenumber limit, $\beta \to 0$, and as β^{-1} in the high wavenumber limit, $\beta \to \infty$. These results are valid only when gravitational effects are not important, and must therefore be corrected when $Ca \gg 1$ (reduced surface tension effects), since gravitational forces will become comparable to surface-tension-induced forces as measured by the Bond number $Bo \sim$ O(1). Gravity will accelerate leveling, and thus reduce L_ℓ, more so for longer wavelength ribs. Neglecting gravity sets a low-wavenumber cutoff for the ribbed geometries that can be considered accurately.

IV Leveled Film: In this region the film is rib-free and the flow field is one-dimensional. This region is far downstream from the meniscus, since leveling generally occurs over a very long distance.

3.2 Model Components

In what follows, we address the mechanisms associated with the model in more detail: first we discuss the nonlinear nature of ribbing (I); next we evoke film leveling to explain the spatial persistence of ribs (III); finally, we match these two regimes (II) to construct the complete model. The discussion that follows concerns flows for which ribbing is observed.

As described in Chapter 1, for sufficiently large Ca ($Ca > Ca_c$), the two-dimensional solutions are unstable to spanwise perturbations (for a limited range of wavenumbers $\beta \in [\beta_{\mathrm{L}}, \beta_{\mathrm{H}}]$) to the free surface in the meniscus region. As a result of this supercritical bifurcation, an initially small disturbance will evolve into a finite-amplitude rib, the amplitude and structure of which we present (based on numerical results) in Chapter 7. However, the driving pressure gradient normal to the free surface becomes vanishingly small outside the meniscus region, and ribs, therefore, cannot grow either in the transition region or further downstream. This observation is in agreement with the rapidly decaying eigenfunctions found in the linear stability analysis of Coyle et al[14]; this picture is also consistent with the experimental observations of Hasegawa and Sorimachi [33], in which local quenching of the instability in the meniscus region eliminates the instability everywhere downstream. Based on these arguments, we conclude that ribs observed downstream of the meniscus can only originate in the meniscus. Why, then, do perturbations which grow only in the meniscus region persist far downstream?

3.2.1 Leveling of a Viscous Film

In order to understand the spatial persistence, we first look at the physics of leveling. We consider the leveling[41, 46, 48] of a fluid film of mean thickness h_o^* and viscosity μ^* under the effect of surface tension σ^*. At time $t = 0$ the free surface disturbance is of sinusoidal shape of amplitude A_0^* and wavelength λ^*, as depicted in Fig. 3-4. For typical roller configurations, gravity and fluid inertia terms are unimportant (see below). If we assume that the perturbation amplitude is small compared to the wavelength, $A^* \ll \lambda^*$, and that the wavelength is large compared to the film thickness, $\lambda^* \gg h_o^*$, the pressure difference that drives the leveling of the film scales as $\Delta p^* \sim p_a^* - p_b^* \sim \sigma^* A^*/(\lambda^*)^2$, and thus $\Delta p^*/\Delta z^* \sim \sigma^* A^*/(\lambda^*)^3$. Assuming locally fully developed plane Poiseuille flow, the local volume flowrate (per unit s^* depth) in the spanwise direction is then given by $Q_z^* \sim (1/\mu^*)\ (\Delta p^*/\Delta z^*)\ (h_o^*)^3$. As the volume of fluid that must be displaced scales with $\lambda^* A^*$, the time to equilibration scales as

$$\tau^* \sim \frac{\lambda^* A^*}{Q_z^*} \sim \frac{\mu^*}{\sigma^*} h_o^* \left(\frac{\lambda^*}{h_o^*}\right)^4 \quad \left(\text{for } \frac{\lambda^*}{h_o^*} \gg 1\right). \tag{3.1}$$

In the limit of short wavelength disturbances[41, 48] (similar to deep water waves), the time to level scales linearly with the wavelength of the disturbance. In this case, the flow rate associated with the leveling of the ribs is no longer a function of the

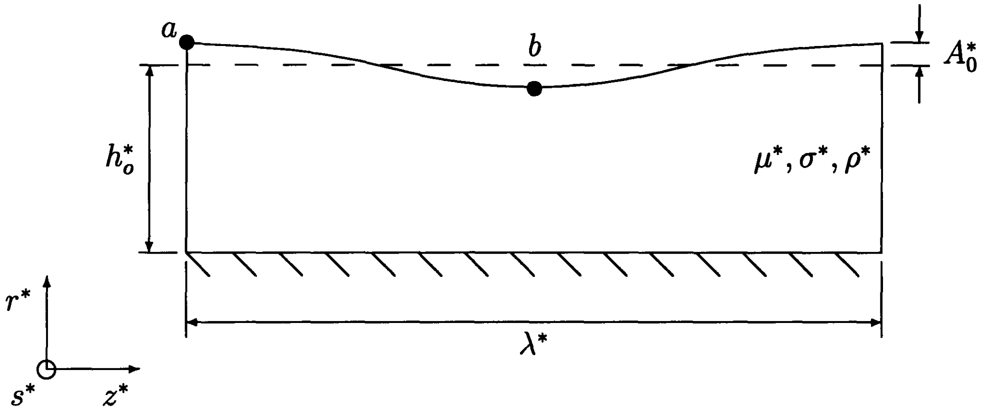
a
b
A_0^*
h_o^*
μ^*, σ^*, ρ^*
r^*
s^*
z^*
λ^*

Figure 3-4: Leveling of a thin viscous film ($h_o^* \ll \lambda^*$). The main flow is in the (r^*, z^*) plane (r^* is normal to the surface of the roller), driven by surface-tension-induced pressure gradients in the z^* direction.

film thickness as is the case with thin viscous films. The film thickness is not the characteristic length associated with the flow field; the characteristic length is now λ^*, resulting in $Q^* \sim (1/\mu^*)\,\sigma^*\,A^*$ and thus

$$\tau^* \sim \frac{\lambda^* A^*}{Q_z^*} \sim \frac{\mu^*}{\sigma^*} h_o^* \left(\frac{\lambda^*}{h_o^*}\right) \quad \text{for} \quad \frac{\lambda^*}{h_o^*} \ll 1. \tag{3.2}$$

Equations (3.1) and (3.2) correspond to kinematic time scales based on conservation of mass arguments for which we neglected inertial terms, both unsteady and advective, throughout. Viscous effects must dominate over both unsteady and advective terms, and we thus require:

$$\tau^* \gg \frac{\rho^* \left(h_o^*\right)^2}{\mu^*} \tag{3.3}$$

and

$$u^* \ll \frac{\mu^* \lambda^*}{\rho^* \left(h_o^*\right)^2}, \tag{3.4}$$

respectively. Combining the previous expressions with Eqs. (3.1) and (3.2) we obtain the following conditions:

$$\frac{\rho^* \sigma^* h_o^*}{(\mu^*)^2} \left(\frac{h_o^*}{\lambda^*}\right)^4 \ll 1 \text{ and } \frac{\rho^*\,\sigma^*\,A^*}{(\mu^*)^2} \left(\frac{h_o^*}{\lambda^*}\right)^4 \ll 1 \tag{3.5}$$

for long wavelength ribs and

$$\frac{\rho^* \sigma^* h_o^*}{(\mu^*)^2} \frac{h_o^*}{\lambda^*} \ll 1 \text{ and } \frac{\rho^*\,\sigma^*\,A^*}{(\mu^*)^2} \frac{h_o^*}{\lambda^*} \ll 1 \tag{3.6}$$

for short wavelength ribs, respectively. We concentrate on small-amplitude ribbed flows for which the ratio Re/Ca is small (this is the case in most ribbed flows, eg as shown before $Re \equiv 10^{-3}$ and $Ca = \mathrm{O}(1)$) thus satisfying both criterions for neglecting inertial terms in the leveling analysis.

Orchard[48] and Khesghi[41] solve the equations of motion exactly for small amplitude disturbances without restrictions on the wavelength; the expression for the time scale associated with leveling in the creeping flow limit, without neglecting gravitational forces acting normal to the free surface, is shown to be

$$\tau^* = 2 \left[\frac{\mu^*}{(h_o^*)^2 \, \rho^* g^* + \sigma^* \, \beta_f^2} \right] \left[h_o^* \, \beta_f \, \frac{1 + \beta_f^2 \, \mathrm{sech}^2 \beta_f}{\tanh \beta_f - \beta_f \, \mathrm{sech}^2 \beta_f} \right] , \tag{3.7}$$

where β_f is the nondimensional wavenumber based on the average film thickness, $\beta_f = 2\,\pi\, h_o^*/\lambda^*$. Here τ is defined such that the evolution of the amplitude of the disturbance is given by $A^*\,(t^*) = A_0^* \,\exp\,(-t^*/\tau^*)$. Equation (3.7) reduces to Eqs. (3.1) and (3.2) in the appropriate limits, as shown in Fig. 3-5. This requires that gravity-induced hydrostatic forces $(\rho^* g^* A^*)$ be small compared to the surface-tension-induced pressure forces $(\sigma^* A^* \,(\lambda^*)^2)$; this is clearly visualized in Eq. (3.7) where both terms appear explicitely. The criterion for neglecting gravitational effects is thus

$$Bo = \frac{(h_o^*)^2 \, \rho^* g^*}{\sigma^* \, \beta_f^2} \ll 1 \tag{3.8}$$

where Bo is called the Bond number, which measures the ratio of gravitational forces to surface-tension-induced forces. As mentioned previously, we concentrate on flows where gravitational and inertial effects are negligible and thus the analysis that follows is for $Bo \ll 1$ (thin films with ribs of wavelengths that are not too great). Neglecting gravitational effects provides a low wavenumber cutoff for the validity of the results. Levelling will be, in general, underestimated compared to an experimental setup since the effects of gravity have been neglected.

To consider the movement of a fluid film entrained by rollers, we must now superimpose on the leveling solution a velocity V^* normal to the plane of the film. Leveling can be interpreted to occur as the film moves in the downstream direction; time in Eqs. (3.1), (3.2), and (3.7), can then be replaced by the distance traveled downstream, s^*, divided by the superimposed velocity, V^*. This neglects the effect of downstream curvature (which is very small) of the free-surface on the leveling rate and on the mean film thickness. From the previous expressions, the length scale in

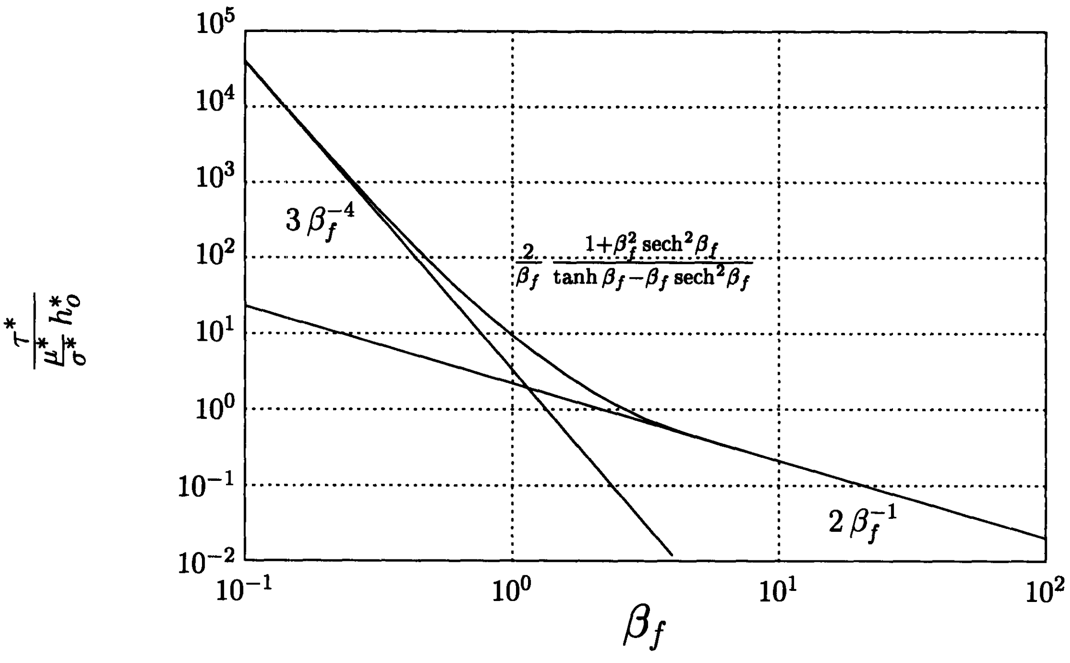

Figure 3-5: Time constant associated with the surface-tension-driven leveling of a disturbance on a viscous film as a function of the wavenumber β_f.

the downstream direction associated with leveling, $L_\ell = L^*_\ell / H^*$, can be estimated as

$$L_\ell = 3\,Ca\,\beta_{f_{\mathrm{IV}}}^{-4}\,f_{\mathrm{IV}} \quad \text{for} \quad \frac{\lambda}{H} \gg 1, \tag{3.9}$$

$$L_\ell = 2\,Ca\,\beta_{f_{\mathrm{IV}}}^{-1}\,f_{\mathrm{IV}} \quad \text{for} \quad \frac{\lambda}{H} \ll 1, \tag{3.10}$$

where f_{IV} is the leveled film thickness, trivially calculable once Q, the volume flowrate per unit depth, is known and $\beta_{f_{\mathrm{IV}}}$ is the wavenumber of the rib based on the leveled film thickness f_{IV}, $\beta_{f_{\mathrm{IV}}} = 2\pi\,f_{\mathrm{IV}}/\lambda$. A value of $Q \cong 1.3$ can be used as an estimate in forward-roll coating, as described in Chapter 6. Here L_ℓ is defined such that the film amplitude decays as $\exp(-s/L_\ell)$, where s is the distance along the roller.

Equations (3.7), (3.9), and (3.10) show two characteristics of leveling that we will use to explain the spatial persistence of ribs. Firstly, viscosity hinders the leveling process; this is in contrast to the decay of a *velocity* perturbation, in which the decay rate is increased by increasing viscosity. Secondly, the distance over which leveling takes place, L_ℓ, decreases monotonically with the wavenumber of the perturbation as shown in Fig. 3-5. If wavenumber interactions are negligable (as should be the case for small amplitude ribs) we expect that as the ribbed film proceeds downstream, the high wavenumber components of the disturbance will decay at a faster rate than the low wavenumber components.

3.2.2 Transition from Ribbing to Leveling

The two flow fields discussed –meniscus and leveling– do not match; in the meniscus region, the fluid is drawn into the crests of the ribs and away from the troughs[14], as shown schematically in Fig. 3-6(I), while in leveling films, fluid is drained from the crests, as shown schematically in Fig. 3-6(III). The eigenfunctions resulting from linear stability analysis indicate growth of the disturbances in the meniscus region and vanishingly small growth downstream and the corresponding underlying flow field but do not (and can not) exhibit the correct flow field for the decay of the ribs downstream. The flow geometries and flow fields are "matched" in what we term the transition region. The helical velocity field will decay under the action of viscosity over a length $L_t = L_t^*/H^*$ which is on the order of the viscous length scale of the film. The length scale over which the meniscus flow field decays can be estimated by considering the equivalent problem of the decay of thermal disturbances in a periodic domain. This problem is almost equivalent to the viscous flow problem of interest. The original helical disturbance, $v\,(0, y, z)$, can be written in the following form

$$v\,(0, y, z) = \mathrm{Re}\left\{\sum_{m=1}^{\infty}\sum_{n=-\infty}^{\infty} a_{mn} \sin\frac{2m\pi y}{h_o} \exp\left(\frac{2\pi inz}{\lambda}\right)\right\} \tag{3.11}$$

which satisfies the equivalent no-slip and no-shear boundary conditions for $y = 0$ and $y = h_o$ respectively. We seek solutions of the form

$$v\,(x, y, z) = \mathrm{Re}\left\{\sum_{m=1}^{\infty}\sum_{n=-\infty}^{\infty} a_{mn} \exp\left(-\frac{x}{\chi_{mn}}\right) \sin\frac{2m\pi y}{h_o} \exp\left(\frac{2\pi inz}{\lambda}\right)\right\} \tag{3.12}$$

to the governing equation

$$\nabla^2 v = 0 \tag{3.13}$$

resulting in

$$\chi_{mn} = \left(\frac{4m^2\pi^2}{h_o^2} + \frac{4n^2\pi^2}{\lambda^2}\right)^{-\frac{1}{2}} \tag{3.14}$$

where χ_{mn} is the length scale associated with the decay (in space) of the disturbance component identified by the subscript pair mn. The largest χ_{mn} corresponds to the most persistent mode (in space) and is equal to

$$\chi = \chi_{11} = \left(\frac{4\pi^2}{h_o^2} + \frac{4\pi^2}{\lambda^2}\right)^{-\frac{1}{2}} = h_o\left(4\pi^2 + \beta_f^2\right)^{-\frac{1}{2}} \tag{3.15}$$

which in the limit of low-wavenumber disturbances ($h_o/\lambda \leq \mathrm{O}\,(1)$), scales with the film thickness h_o. The analogy assumes that the downstream pressure gradient is identically zero in the transition region; in reality, the pressure gradient is not identically zero, just not large enough to support the ribs, and thus we expect that the vortical velocity profiles decay over a distance slightly larger than h_o^*/H^*. On leaving the transition region, the ribs level following the mechanisms outlined above.

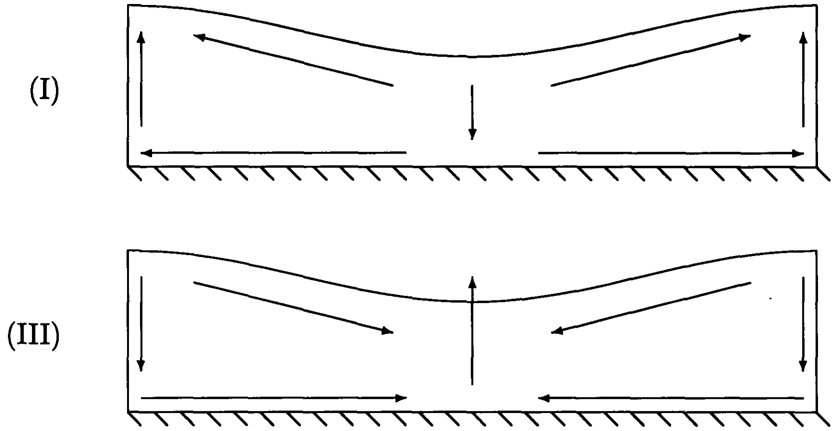

Figure 3-6: Schematic of characteristic flow fields: (a) meniscus region, (b) leveling region.

3.3 Approach to the Steady Ribbed State

We have addressed the growth of disturbances and estimated the time scale for their "linear" growth based on linear stability theory. We have not addressed the final approach to the steady state and its corresponding time scale. The time scale associated with the approach towards the steady state is, in general, longer than that associated with the initial growth of the free-surface disturbance (which is approximately the inverse of the growth rate γ determined by linear stability). The approach to the steady state is governed by pressure gradients due to spanwise free-surface curvature, in contrast to in-plane free-surface curvature which drives the initial disturbance growth. The fluid forces due to the spanwise curvature balance the "new" viscous forces due to the disturbance and thus can be used to estimate the time scale associated with the approach to the steady state. This balance between spanwise-curvature-induced pressure gradients and viscous effects is observed in the leveling of viscous films as described above. This observation can be used to estimate the resulting time scale for the approach to the steady state (equal to $\mathrm{d}A_s/\mathrm{d}t$); τ_{ss} is of the same magnitude of the time scale associated with leveling and is approximately equal to

$$\tau_{ss} = \frac{1}{\frac{dA_s}{dt}} \sim 2\,Ca\,\frac{\lambda}{2\pi}. \tag{3.16}$$

The time constant depends on the harmonic content in the steady state, but the slowest mode should be the dominant factor in determining the time constant.

The previous results indicate that two regimes should likely be observed during the evolution from the unstable two-dimensional steady states to the stable three-dimensional steady-states: first a linear growth followed by the saturation of the growth (as is shown in Chapter 7).

3.4 Summary

The pressure gradient caused by in-plane curvature in the meniscus region generates ribs that move downstream with the rollers. The initial growth (in time) of the ribs (in region I) is determined by the in-plane free-surface curvature (linear stability) while the final non-linear evolution toward the steady-state is governed by the spanwise free-surface curvature. As the ribs proceed downstream, the flow field under the ribs suffers a (spatial) transition (in region II), over a distance order h_o^*/H^*, from the helical nature of the meniscus region to the "convergent" flow field of the leveling film region. Upon leaving the transition region, the ribs begin leveling and persist downstream over a very long length scale (region III), given by Eqs. (3.9) and (3.10). Due to the dependence of the leveling rate on the wavenumber content of the rib profile, the rib profile first becomes monochromatic (still in the leveling region III) and, eventually, uniform far downstream (in region IV).

We now present the numerical methods and the numerical calculations by which we verify and quantify these predictions: the instability of the meniscus; the bimodal growth of the meniscus instability; the coupling between the instability of the meniscus and the ribs observed downstream; the rapid change in the spanwise flow field in the transition region; and the leveling of the ribs.

Chapter 4

Numerical Methods for Two-Dimensional Flows

In this chapter, we present the methods used to generate the steady two-dimensional base states required as a point of departure for the three-dimensional simulations. In the following chapter we present the methods used to obtain the three-dimensional steady ribbed states. In what follows, we summarize the numerical methods adopted, discuss the treatment of any non-conventional boundary conditions, and present the remeshing and continuation algorithms developed.

4.1 Numerical Procedure

For the solution of *steady* ($u_{i,t} \equiv 0$ in Eq. (2.1)) two-dimensional problems we adopt a numerical procedure developed by Ho and Rønquist[38] for the efficient treatment of problems in which surface tension forces dominate inertial contributions ($ReCa \ll 1$). A brief description of the solution algorithm, hereafter referred to as S, follows:

S0 Initialize iteration counter, $\mathrm{S_I} = 0$.

S1 Solve the (spectral element) spatial discretization of Eq. (2.1) subject to the mixed boundary conditions $u_i n_i = 0$ and $t_i \left[u_{i,j} + u_{j,i}\right] n_i = 0$ on the free surface, $\partial\Omega_4$, with the remaining boundary conditions on $\partial\Omega \setminus \partial\Omega_4$ as described by Eqs. (2.2), (2.3), (2.4), and (2.6). The mixed boundary conditions applied correspond to what is observed at a steady state (see step S2).

S2 Compute the residual traction on $\partial\Omega_4$ based on the solution of step S1. The residual traction is defined as $r_i = \tau_{ij}\, n_j - \sigma\, \kappa\, n_i$ where $\tau_{ij}\, n_j$ is the traction on the free surface, and $\sigma\, \kappa$ is the surface-tension-induced pressure jump across the free surface. The residual traction is identically zero for a steady-state solution.

S3 Perform a direct solve of a Poisson problem for the corrections to the free-surface geometry, Δx_i; the free-surface curvature is expressed as a function of the corrections to the free-surface geometry, and the residual traction, r_i, enters as an inhomogeneity to the resulting Poisson problem. This procedure produces a non-zero Δx_i for the mesh node of the free-surface that is common to outflow. The correction of this node is projected onto the plane of outflow thus allowing for changes in the outflow film thickness (while preserving the downstream position of the outflow) as the free-surface node "slides" in the outflow plane.

S4 Extend Δx_i into the interior (and free-surface) of the domain by means of an elliptic (partial-differential-equation) operator. The sliding mesh requires that the mesh nodes at outflow be updated. This will not be the case in the three-dimensional equivalent as discussed in the following Chapter.

S5 Update all the mesh coordinates and iteration counter, $\mathrm{S_I} = \mathrm{S_I} + 1$.

Steps S1 through S5 are repeated until the maximum correction to the free-surface geometry is smaller than a tolerance, say until $\max_{\partial\Omega_4} \Delta x_i < 3.0 \times 10^{-4}$.

The numerical procedure comprises: variational description of the curvature [36, 56]; spectral element spatial discretization [36, 49, 53, 5]; decoupled treatment of the domain geometry; solution of the nonlinear system of discretized momentum equations by Newton-Raphson iteration; direct serial solution of the free-surface curvature solve[38]; and elliptic mesh extension[36]. The variational description of the curvature provides a surface-intrinsic natural (weak) condition for continuity of the surface tangent across elemental boundaries, and does not require either a global coordinate system, orthogonal local coordinate systems, or a C^1 free-surface description; the spectral element spatial discretization provides a high-order representation of both the fluid flow and flow geometry which exploits regularities in the solution, requires less degrees of freedom and has a reduced overall workload (even greater in three-dimensions) than a low-order finite element[64, 2] discretization for a fixed error requirement; the decoupled treatment of the domain geometry and the flow solution reduces the problem size relative to a coupled treatment, and enables fast subproblem solution strategies. In addition, the spectral element domain discretization allows for simpler remeshing techniches due to the structured nature of the mesh.

4.1.1 Special Treatment of Boundary Condition at Inflow

As described in the problem formulation, the boundary condition at inflow, $\partial\Omega_1$ given by Eq. (2.11) relates the pressure at the nip, $p_{\rm nip}$, to the volume flowrate per unit depth through the nip, Q; the latter, however, is not known *a priori*. Equation (2.11) is thus, treated by means of an outer loop, OL; this is possible since the dependence of the final flow geometry on the nip pressure is weak and is consistent with our explicit treatment of the nonlinear operators. Coyle et al[12, 14] added Eq. (2.11) to the system of equations, while other investigators varied the flowrate "manually" until the pressure boundary condition is met at the inlet. The treatment implemented is as follows:

OL0 Assume a value of $Q = 1.3$ to calculate the corresponding pressure at the nip, $p_{\rm nip}$, based on Eq. (2.11). Initialize outer loop iteration, $\mathrm{OL_I} = 1$.

OL1 Solve for the steady-state geometry, flow field, and hence flowrate using the procedure, S, described above.

OL2 Update the outer loop iteration counter and re-compute the pressure at the nip as given by Eq. (2.11) with a new volume flowrate obtained by under-relaxing the flowrate obtained in step OL1 with that of the previous iteration. More precisely, the flowrate that will be used to compute the pressure at inflow in Eq. (2.11), is taken to be:

$$Q = \frac{Q_{\mathrm{OL_I}} + K_{\mathrm{OL}}\, Q_{\mathrm{OL_{I-1}}}}{1 + K_{\mathrm{OL}}} \tag{4.1}$$

where $Q_{\mathrm{OL_I}}$ is the flowrate obtained in step OL1 and $Q_{\mathrm{OL_{I-1}}}$ is the flowrate corresponding to the previous outer loop iteration. The constant K_{OL} is conservatively set to 6. Smaller values can be used for $Ca > 1$ for which the flowrate does not change much.

If steps OL1 and OL2 are repeated until there is no appreciable change in the computed steady flow geometries, say using a stopping criterion based the maximum change of position over all free-surface mesh nodes between two computed steady states ($\max_{\partial\Omega_4} \Delta x_i$): $\max_{\partial\Omega_4} \Delta x_i < 3.0 \times 10^{-4}$, incorrect flow rates are obtained since Eq. (2.11) is not satisfied. This is because the flowrate is a measure of the overall meniscus shape and not due to the "local" meniscus position and thus with very small local changes in the meniscus geometry, greatly varying flow rates can be obtained. Instead of the stopping criterion presented above, we adopt a criterion based on the computed flow rate. If the flow rate difference between two computed steady states differ by less than .05% (in addition to the condition on the free surface geometry described above), the flow geometry is taken to be at a steady state and to satisfy the flooded inflow condition.

4.2 Remeshing

For very large surface deformations the elliptic partial-differential-equation mesh-coordinate extension scheme[35, 36], may yield elements that are nearly singular (indicated by vanishing Jacobians) as observed in Fig. 4-1 (b).

To remedy this problem we initiate automatic remeshing procedures when the iteration counter $\mathrm{S_I}$ exceeds a given value. This open-loop procedure can be further refined by initiating the automatic remeshing only when absolutely required. The

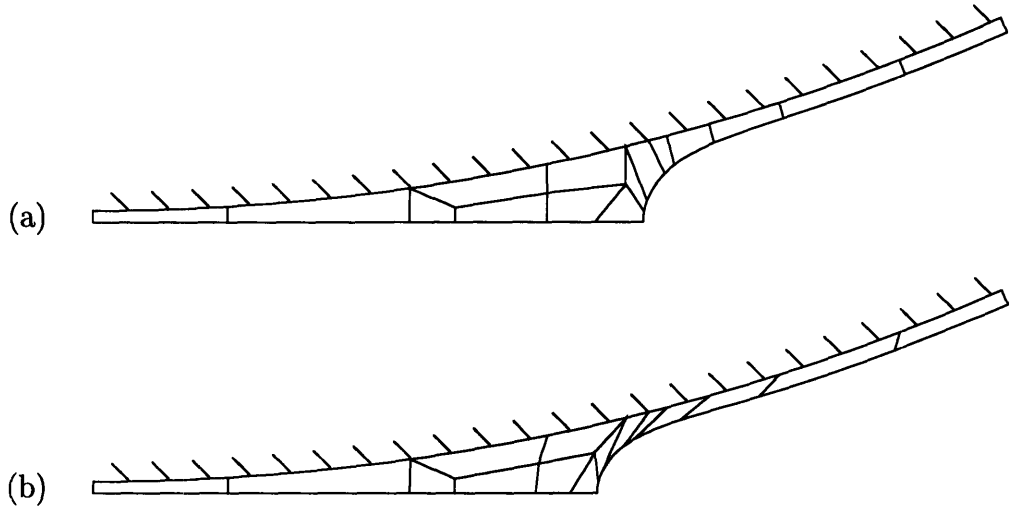

Figure 4-1: Example of interruption of solution procedure during evolution from (a) one steady state ($D = 200$, $Ca = .1$) to a new desired steady state ($D = 200$, $Ca = 1$) due to a (b) greatly distorted mesh with a vanishing Jacobian.

smallest Jacobian over all elements can be used as a measure of the quality of the mesh; when the Jacobian falls below a given threshold, indicating impending problems, the remeshing procedure can be executed. This closed-loop strategy was not necessary, though, since the computational cost of remeshing is small allowing for remeshing even when not required. During the remeshing procedure, a new spectral element mesh is constructed based on a template (see Fig. 4-2), which provides the connectivity information between elements, and the current mesh, which provides the geometry, and, in particular, the position of the meniscus. The steps of the remeshing procedure implemented, R, are described in more detail in what follows:

R1 Extract necessary information from the current mesh: the position, x_s and θ_s, of the mesh node where the free surface meets the symmetry plane; the piecewise polynomials that define the free surface ($\partial\Omega_4$); and the film thickness at outflow, $f_{\partial\Omega_3} = r_{f_{\partial\Omega_3}} - D/2$, as shown in Fig. 4-3.

R2 Compute the desired position of the outflow boundary ($\partial\Omega_3$), given by $\theta_{\partial\Omega_3} = \theta_s + 10\pi/180$ or $\theta_{\partial\Omega_3} = 1.5\,\theta_s$, which ever is greater, and an estimate for the

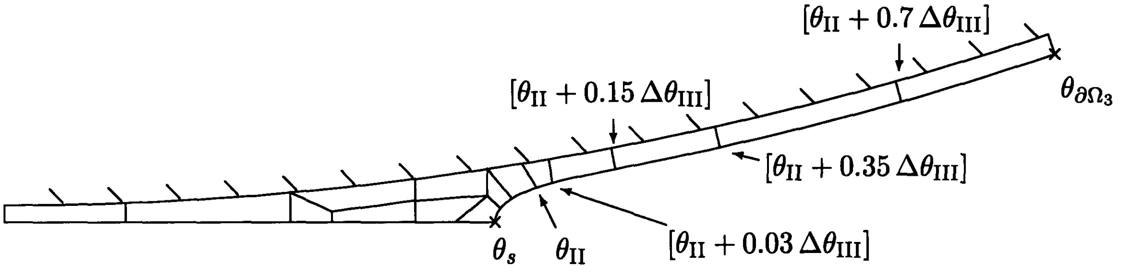
$[\theta_{\mathrm{II}} + 0.7\,\Delta\theta_{\mathrm{III}}]$
$[\theta_{\mathrm{II}} + 0.15\,\Delta\theta_{\mathrm{III}}]$
$\theta_{\partial\Omega_3}$
$[\theta_{\mathrm{II}} + 0.35\,\Delta\theta_{\mathrm{III}}]$
θ_s
θ_{II}
$[\theta_{\mathrm{II}} + 0.03\,\Delta\theta_{\mathrm{III}}]$

Figure 4-2: Representative information of mesh template for a two-dimensional domain discretization.

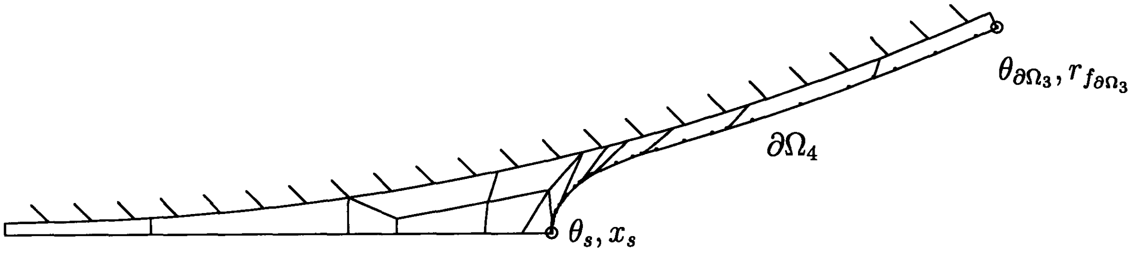
$\theta_{\partial\Omega_3}, r_{f\partial\Omega_3}$
$\partial\Omega_4$
θ_s, x_s

Figure 4-3: Step R1 of the two-dimensional remeshing procedure applied to the greatly distorted mesh of Fig. 4-1: extract relevant free-surface information (position of the free surface mesh nodes).

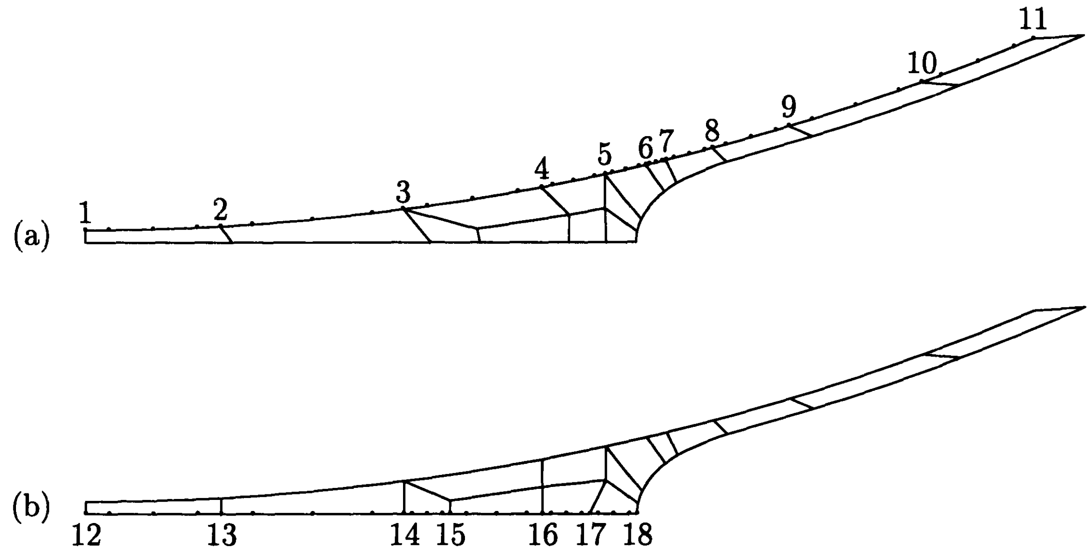

Figure 4-4: Step R3 of the two-dimensional remeshing procedure: position mesh nodes (a) on the rollers, and (b) on the mid-plane. (To aid in visualization, steps R5 and R6 were also performed.)

position of the end of the meniscus region, given by $\theta_{\text{II}} = \theta_s + 0.8\,\pi/180$, as shown in Fig. 4-2. The meniscus region length is thus $\Delta\theta_{\text{II}} = \theta_{\text{II}} - \theta_s$ and the film length is set to $\Delta\theta_{\text{III}} = \theta_{\partial\Omega_3} - \theta_{\text{II}}$

R3 Position element-edge boundary-nodes on the rollers ($\partial\Omega_2$) and on the mid-plane ($\partial\Omega_5$) based on the template information shown in Fig. 4-4 and Table 4.1. The element-edge internal-nodes are then positioned based on the element-edge boundary-nodes and the edge template as shown in Fig. 4-5.

R4 Discretize the free surface into curved segments based on the template information shown in Fig. 4-6 and Table 4.2. The angles corresponding to the beginning and end of a free surface segment are a function of θ_s, $\theta_{\partial\Omega_3}$, and the element under consideration. The mesh nodes are positioned along the free surface based on the high-order polynomial information extracted in step R1. The angle θ is used to parameterize the free-surface in the film region ($\theta \geq \theta_{\text{II}}$). Problems arise for $\theta < \theta_{\text{II}}$ though, and to remedy the problem another angle is used. The new angle is such that $\tilde{\theta} = 0$ where the free-surface intersects the mid-plane and

θ_1	0
θ_2	$.25\theta_s$
θ_3	$.59\theta_s$
θ_4	$.85\theta_s$
θ_5	$.87\theta_s$
θ_6	$\theta_{\mathrm{II}} - .25\Delta\theta_{\mathrm{II}}$
θ_7	$\theta_{\mathrm{II}} + .03\Delta\theta_{\mathrm{III}}$
θ_8	$\theta_{\mathrm{II}} + .15\Delta\theta_{\mathrm{III}}$
θ_9	$\theta_{\mathrm{II}} + .35\Delta\theta_{\mathrm{III}}$
θ_{10}	$\theta_{\mathrm{II}} + .70\Delta\theta_{\mathrm{III}}$
θ_{11}	$\theta_{\mathrm{II}} + \Delta\theta_{\mathrm{III}}$

x_{12}	0
x_{13}	x_2
x_{14}	x_3
x_{15}	$(2x_3 + x_4)/3$
x_{16}	x_4
x_{17}	$(x_4 + x_s)/2$
x_{18}	x_s

Table 4.1: Position of element-edge boundary nodes: (a) on the rollers, and (b) on the mid-plane.

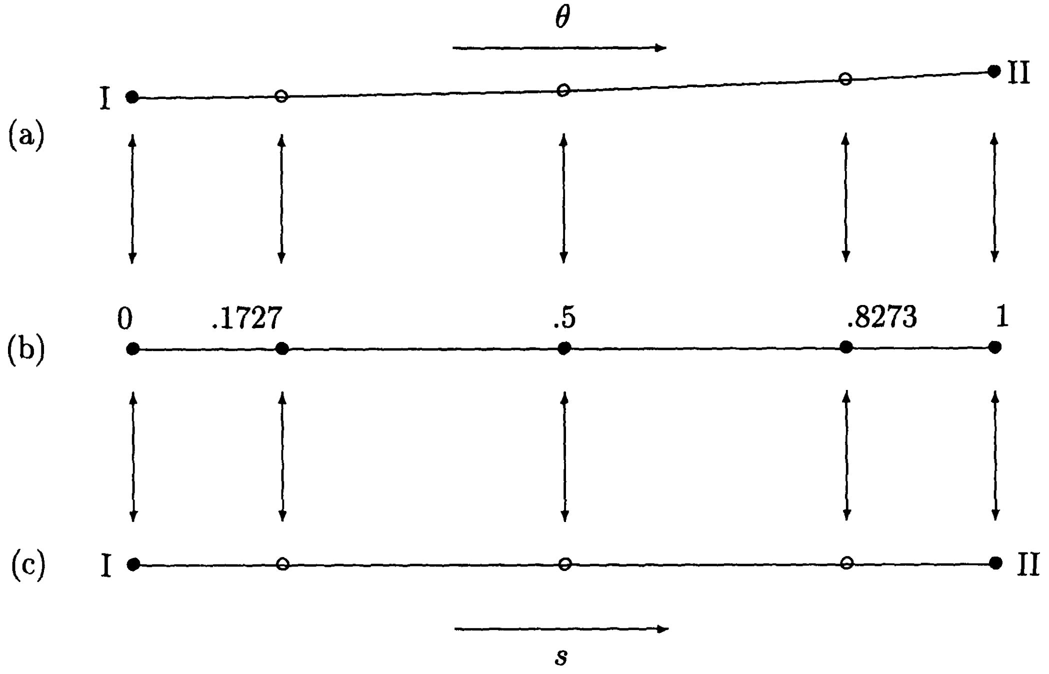
θ
I
II
(a)
0
.1727
.5
.8273
1
(b)
(c)
I
II
s

Figure 4-5: Position of internal element-edge nodes relative to the edge boundary nodes: (a) on the rollers, (b) edge template, and (c) on the mid-plane.

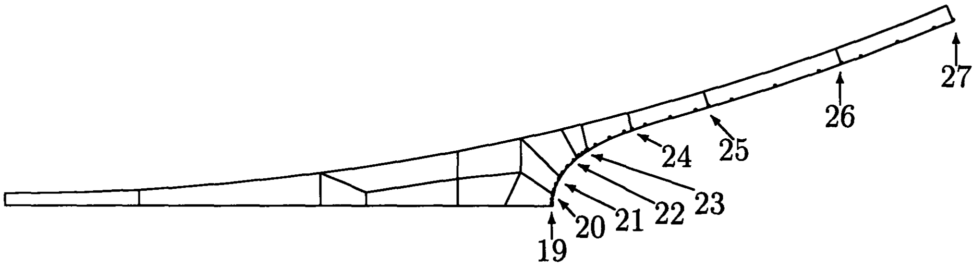

Figure 4-6: Step R4 of the two-dimensional remeshing procedure: discretize the free surface extracted in step R1, and position mesh nodes based on the edge boundary nodes and the downstream position.

$\tilde{\theta} = \theta_{\mathrm{II}}$ where $\theta = \theta_{\mathrm{II}}$. The angle used to parameterize the free-surface is given by:

$$\tilde{\theta} = \begin{cases} \theta & \text{for} \quad \theta \geq \theta_{\mathrm{II}} \\ \arctan\left(\frac{y}{\frac{D+H}{2}\tan\theta_{\mathrm{II}} - x}\right) & \text{for} \quad \theta < \theta_{\mathrm{II}} \end{cases} \tag{4.2}$$

which is a continuous single-valued parameterization of the free-surface.

If the outflow is moved away from the nip, information is not available to position the nodes; to get around this problem, the film thickness is assumed constant and equal to $f_{\partial\Omega_3}$, independent of θ, for all the mesh nodes in this region.

R5 Construct inter-element edges as well as the remaining external edges, the inflow

$\tilde{\theta}_{19}$	0
$\tilde{\theta}_{20}$	$.25\theta_{\mathrm{II}}$
$\tilde{\theta}_{21}$	$.60\theta_{\mathrm{II}}$
$\tilde{\theta}_{22}$	θ_{II}
$\tilde{\theta}_{23}$	$\theta_{\mathrm{II}} + .03\Delta\theta_{\mathrm{III}}$
$\tilde{\theta}_{24}$	$\theta_{\mathrm{II}} + .15\Delta\theta_{\mathrm{III}}$
$\tilde{\theta}_{25}$	$\theta_{\mathrm{II}} + .35\Delta\theta_{\mathrm{III}}$
$\tilde{\theta}_{26}$	$\theta_{\mathrm{II}} + .70\Delta\theta_{\mathrm{III}}$
$\tilde{\theta}_{27}$	$\theta_{\partial\Omega_3}$

Table 4.2: Position of element-edge boundary nodes on the free surface ($\partial\Omega_4$).

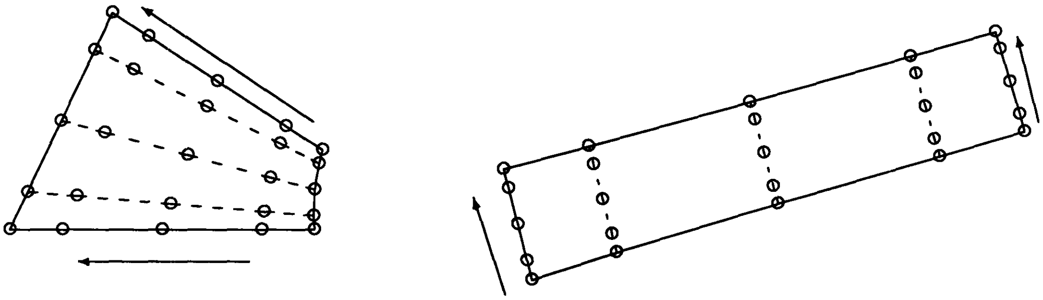

Figure 4-7: Step R6 of the two-dimensional remeshing procedure: Blending algorithm for the position on the internal mesh (collocation) nodes for: (a) near quadrangular element, and (b) high aspect ratio element .

($\partial\Omega_1$) and outflow boundaries ($\partial\Omega_3$), as straight segments.

R6 Position intra-element nodes based on the element boundary nodes and a blending interpolation. The blending algorithm is a function of the aspect ratio of the element in consideration and of the shape of element boundary. Care was placed to avoid elements that had two adjacent curved (non-internal) edges and thus a linear blending suffices; in addition, the linear blending guarantees non-singular Jacobians since it originates from any one of the curved edges. Two examples are shown in Fig. 4-7.

R7 Map field quantities onto the new mesh. This step is not needed (or used) for the creeping two-dimensional problem but, as is seen below, it will be used in the solution of the three-dimensional problem. The mapping of the fluid velocity and pressure fields onto the new mesh is necesary for flows of $Re \neq 0$ since the previous flow field is used a first guess for the non-linear fluid flow solve.

A bi-linear interpolation scheme is used to compute the field value on the new mesh based on the mesh nodes of the original mesh that are closest to the target node on the new mesh. Spectral accuracy is lost due to the bi-linear interpolation but proved not to be detrimental to the three-dimensional solution

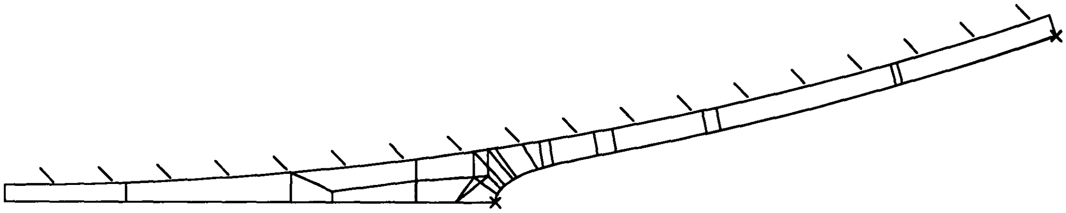

Figure 4-8: Example of remeshing for a not overly deformed domain. The original and final meshes are overlaid.

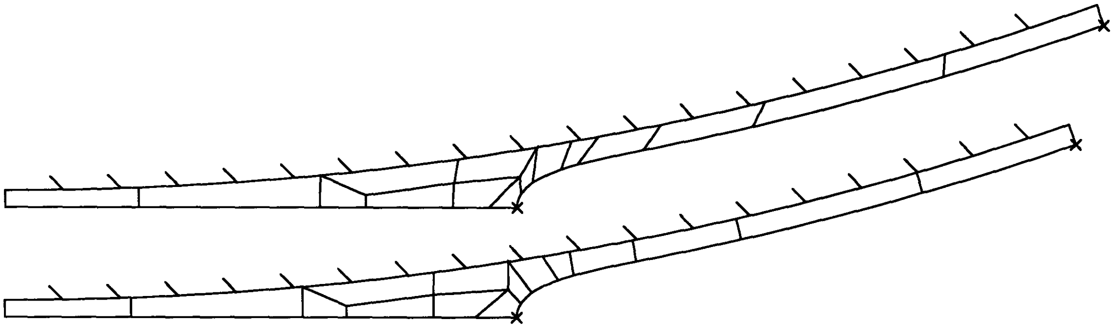

Figure 4-9: Remeshing of greatly distorted elements: top–original mesh; bottom–new mesh.

procedure.

An example of the effects a complete remeshing procedure is shown in Fig. 4-8. This particular discretization has 15 spectral elements; the order of the interpolant in each direction in each element is 5, resulting in approximately 1 500 total degrees-of-freedom (velocity, pressure, and geometry unknowns). The computational cost associated with this *two-dimensional* remeshing is small compared to the fluid flow solution, so remeshing can be performed every few iterations, as shown in Fig. 4-8, even if not strictly required. If remeshing is performed only when the mesh elements are greatly distorted, the effects of remeshing are more easily visualized, as shown in Fig. 4-9.

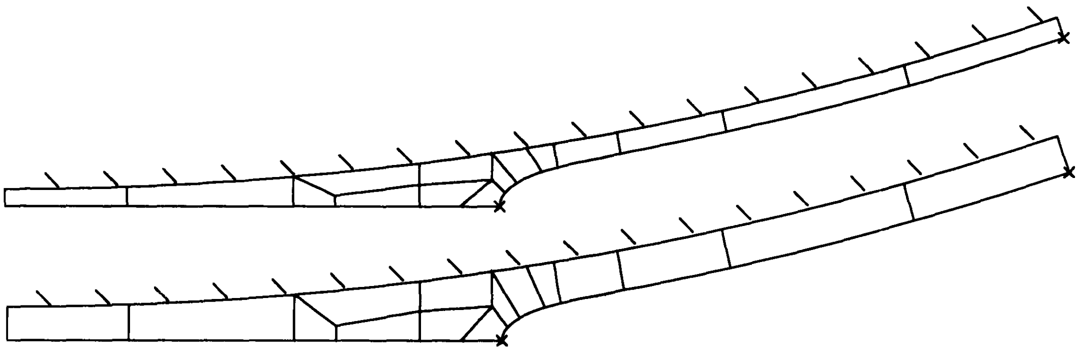

Figure 4-10: Remeshing-continuation for a change in roller separation.

4.3 Extension of Remeshing: Continuation

The modular nature of the remeshing procedure allows for the implementation of simple continuations schemes useful when performing parameter studies that include changes in geometric conditions. For example, if the solution for a new $\{Ca, D\}$ pair is desired, the existing solution for a different geometry D (and Ca) can be used to construct an initial estimate for the desired solution: to wit, the nodes on the rollers are moved in the radial direction to the desired gap during step R4 of the remeshing procedure. An example of a continuation remeshing instigated by a change in the gap between rollers is shown in Fig. 4-10.

Chapter 5

Numerical Methods for Three-dimensional Flows

In the previous chapter, we presented the methods used to generate the steady two-dimensional base states required as a point of departure for the three-dimensional simulations. We now present the methods used to obtain the three-dimensional steady ribbed states. We again summarize the numerical methods adopted, discuss the treatment of any non-conventional boundary conditions, and present the remeshing and continuation algorithms developed.

5.1 Numerical Methods

The numerical methods adopted for the simulation of the *unsteady* three-dimensional free surface fluid flow problem comprise: variational description of the curvature in three space dimensions[37]; arbitrary Lagrangian-Eulerian description of the time-dependent domain[18, 36]; spectral element spatial discretization [36, 49, 53]; semi-implicit[36] fractional time-stepping[54]; and parallel solution [25, 26] of the implicit (pressure and viscous) operators by a preconditioned [54] conjugate gradient[53, 54] algorithm. As mentioned previously, the variational description of the curvature provides a surface-intrinsic natural (weak) condition for continuity of the surface tangent across elemental boundaries, and does not require either a global coordinate system, orthogonal local coordinate systems, or a C^1 free-surface description. The spectral element spatial discretization allows for simplified domain decomposition and a high-order representation of both the fluid flow and flow geometry which exploits regularities in the solution. The spectral element spatial discretization coupled with the semi-implicit treatment has a reduced overall workload (even greater than in two-dimensions) than a low-order finite element discretization for a fixed error requirement. In addition, the semi-implicit approach allows for the implicit treatment of those components of the governing equations amenable to fast iterative solution via preconditioned conjugate gradient iteration (to wit, the Stokes problem, which is further implicitly split into viscous and pressure sub-steps), while permitting explicit treatment of those terms not readily amenable to fast iterative solution, in our case the free-surface kinematic condition and geometry-evolution operator. An important limitation, as described below, is that the explicit treatment of the domain evolution does, however, place restrictions on the maximum allowable step size that can be used in the time integration of the governing equations[35, 36]. The time step criterion proposed by Ho[35] is too restrictive for the creeping flows ($Re \ll 1$) considered, since the criterion is based on the accurate description of free-surface inertial waves. It was determined that for most of the three-dimensional cases considered, the time step can be increased by a factor of 10 without loss of stability (generation of free-surface wiggles). To accurately track the evolution from the unstable two-dimensional steady-states to the stable three-dimensional steady ribbed states requires a great number of time steps, on the order of 10^5 in some cases.

The numerical methods described above were implemented in a commercial fluid-dynamics code, NEKTON$^{\text{TM}}$, by Nektonics Inc. The commercial coded served as the starting point for the methods we used and developed.

5.1.1 Treatment of Boundary Condition at Inflow

The boundary condition at inflow, $\partial\Omega_1$, is applied in a similar fashion to the two-dimensional case; in effect, we assume that the total volumetric flowrate, Q, is not greatly affected by the downstream appearance of ribs[14] and thus the pressure at the inflow is kept constant and equal to the two-dimensional case. The boundary condition allows for changes in the flow rate which would signal problems with the assumption; great changes in the flow rate were not observed for most of the range of parameters considered confirming the validity of our assumption.

5.1.2 Treatment of Boundary Condition at Outflow

The boundary condition at outflow, however, presents several difficulties in the three-dimensional case. In particular, in three space dimensions, the sliding mesh, described in step S3, and the uniform pressure condition, Eq. (2.4), imposed in the two-dimensional case is no longer stable; a spanwise perturbation to the free surface near the outflow will grow. The constant pressure imposed in the spanwise direction creates a positive pressure gradient normal to the free surface just upstream of outflow which was shown to be enough for the growth of the perturbation. More complex outflow boundary conditions must be pursued. For lack of a better approach, we impose the more Draconian – but stable – condition that the free surface thickness at outflow, $f^{3D}_{\partial\Omega_3}$, is uniform in z and equal to the two dimensional leveled film thickness, f_{IV} (in the limit $D \to \infty$).

The deleterious effect of this boundary condition is limited to a small region (in fact, one spectral element) upstream of the outflow boundary, as will be shown in Chapter 7. The free surface transforms from the possibly ribbed geometry to the uniform geometry in this last spectral element. This change in geometry is accompanied by a change in the spanwise velocity profile which can extend up to the second spectral element upstream of the outflow for the cases where ribs are of great amplitude near outflow. As observed in Chapter 3, the flow fields of the meniscus and leveling regions are matched over what we termed the transition region which has an extent of the same order of the film thickness. Similarly, we argue that the outflow condition implemented imposes another velocity field with which the leveling flow field must be matched. Since the outflow condition used also imposes a non-zero downstream pressure gradient near outflow, due to the changing free-surface geometry, the matching takes place over a distance greater than the film thickness.

5.1.3 Domain Decomposition and Downstream Extent

A typical discretization of the three-dimensional domain is shown in Fig. 5-1. The three-dimensional mesh is an extruded two-dimensional mesh with several levels of elements and depth λ in the extrusion direction, z. This particular mesh has 4 levels, 60 spectral elements, and elemental interpolants of order 5 (in each spatial direction), resulting in approximately 50 000 degrees-of-freedom (velocity, pressure, and geometry unknowns). To identify the discretization of the domain, we use the triad {number of elements per level, number of levels, order of the interpolant}, which for Fig. 5-1 is $\{15, 4, 5\}$. After the extrusion of the two-dimensional mesh, the downstream extent of the domain considered is modified according to the wavelength of the rib that is studied following procedures similar to those described in step R2 of the two-dimensional remeshing procedure. The leveling of ribs is a function of the wavelength of the rib and in order to guarantee sufficient extent of the leveling region we set the position of outflow given by $\theta_{\partial\Omega_3}$ based on the λ of the domain considered: if $\theta_{\partial\Omega_3} < 2\,\lambda/D$ we set $\theta_{\partial\Omega_3} = 2\,\lambda/D$ in order to cover some of the leveling region. If $\theta_{\partial\Omega_3} > 2\,\lambda/D$, we do not modify the downstream extent of the domain. The above criterion proved adecuate for all the cases considered except for the cases of great amplitude ribs in large spanwise domain for which the decay of the slowest wavenumber of the rib profile did not agree with the theoretical predictions.

5.2 Remeshing Procedure

The arbitrary Lagrangian-Eulerian description of the time-dependent three-dimensional domain avoids frequent remeshing, which, in the three-dimensional case, is rather expensive. However, global remeshing procedures become necessary when the free surface deforms greatly, as can be the case when tracking the complete evolution from an unstable two-dimensional steady state to a stable three-dimensional steady state for $Ca \gg Ca_c$. The three-dimensional remeshing procedure is a direct extension of the two-dimensional procedure, but now involves an additional template for the discretization in the z direction. An overview of the procedure, $\mathrm{R}^{3\mathrm{D}}$, follows:

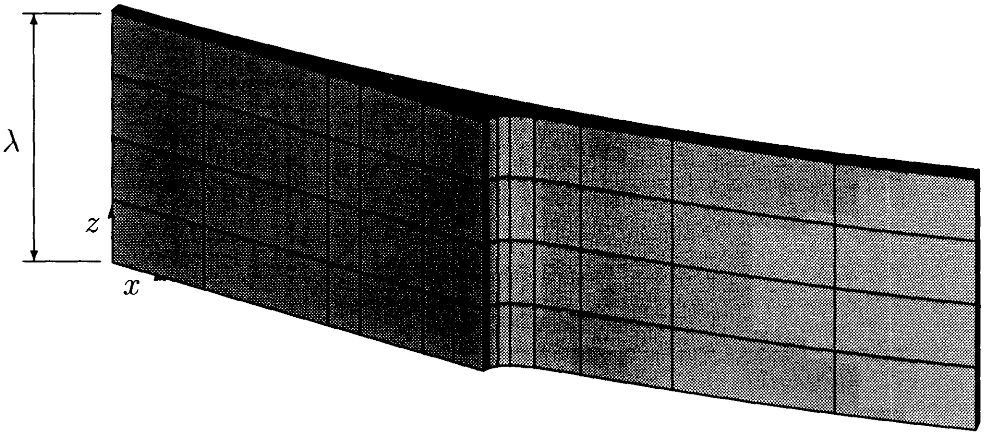

Figure 5-1: Typical three-dimensional discretization of an extruded two-dimensional domain: sixty spectral elements arranged in four levels.

R1^{3D} Extract necessary information from the current three-dimensional mesh: the piecewise polynomials that define $\partial\Omega_4 \bigcap \partial\Omega_5$; the position, $\left(x_s^{3D}, z_s^{3D}\right)$, of the mesh nodes on $\partial\Omega_4 \bigcap \partial\Omega_5$; and the position, $\left(x_c^{3D}, z_c^{3D}\right)$, of the mesh node on $\partial\Omega_4 \bigcap \partial\Omega_5$ where a change of curvature arises. We calculate from this information a measure of the steepness of the ribs,

$$\Delta z^{3D} = 2\,\frac{\left|\arg\max_{z_s^{3D}\in[0,\lambda]} x_s^{3D}\left(z_s^{3D}\right) - z_c^{3D}\right|}{\lambda}. \tag{5.1}$$

We later use this information to determine the relative sizes of elements in the spanwise direction.

R2^{3D} Discretize the domain in the z direction based on the spanwise template and Δz^{3D}; different templates are used for different number of spanwise levels. The template determines the z position of the element boundary sides normal to the extrusion direction. An example of a spanwise template is shown in Fig. 5-2. The other templates used are presented in Table 5.1 where the relative spanwise sizes of the elements are presented as a function of Δz^{3D}.

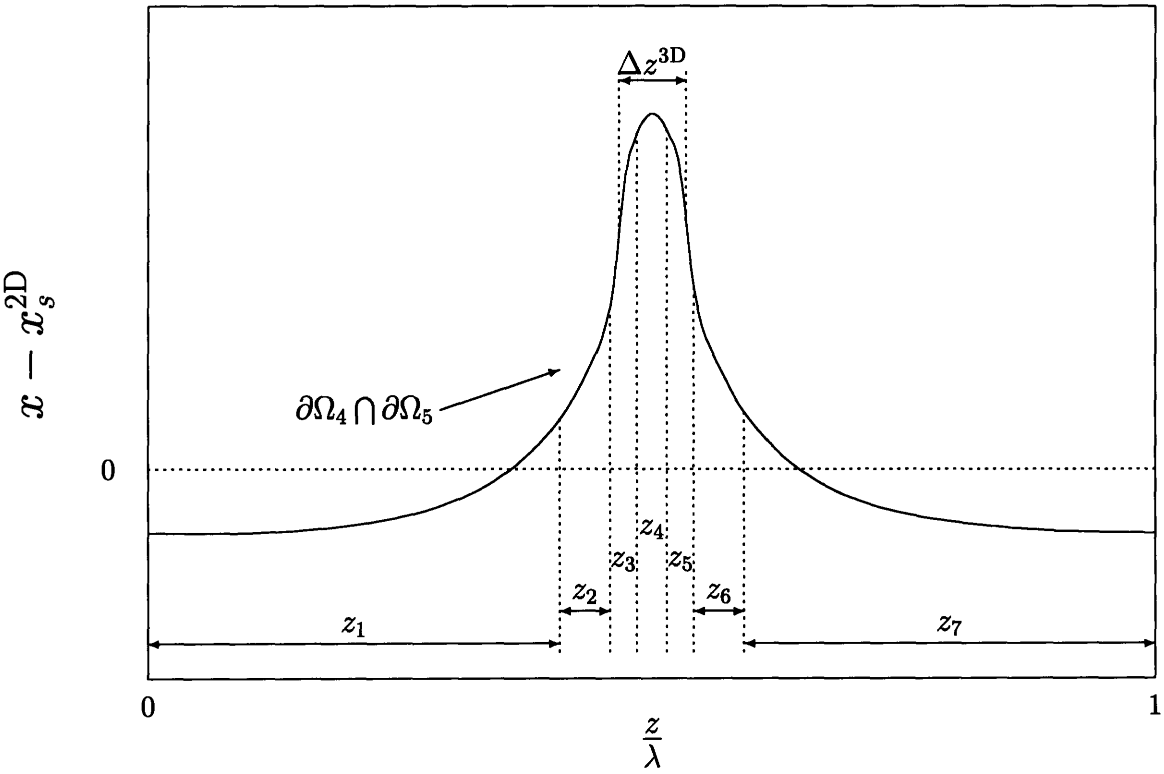

Δz^{3D}
$\partial\Omega_4 \cap \partial\Omega_5$
$x - x_s^{2D}$
0
z_1
z_2
z_3
z_4
z_5
z_6
z_7
0
1
$\frac{z}{\lambda}$

Figure 5-2: Discretization template for mesh consisting of 7 levels in the spanwise direction.

(a)

$\overset{\frac{z_1}{\lambda}}{\frac{1}{2}}$	$\overset{\frac{z_2}{\lambda}}{\frac{1}{2}}$

(b)

$\overset{\frac{z_1}{\lambda}}{\frac{1-z_2}{2}}$	$\overset{\frac{z_2}{\lambda}}{\Delta z^{3\mathrm{D}}}$	$\overset{\frac{z_3}{\lambda}}{\frac{1-z_2}{2}}$

(c)

$\overset{\frac{z_1}{\lambda}}{\frac{1-\sum_{i=2}^{3} z_i}{2}}$	$\overset{\frac{z_2}{\lambda}}{.8\,\Delta z^{3\mathrm{D}}}$	$\overset{\frac{z_3}{\lambda}}{.8\,\Delta z^{3\mathrm{D}}}$	$\overset{\frac{z_4}{\lambda}}{\frac{1-\sum_{i=2}^{3} z_i}{2}}$

(d)

$\overset{\frac{z_1}{\lambda}}{\frac{1-\sum_{i=2}^{4} z_i}{2}}$	$\overset{\frac{z_2}{\lambda}}{.8\,\Delta z^{3\mathrm{D}}}$	$\overset{\frac{z_3}{\lambda}}{\Delta z^{3\mathrm{D}}}$	$\overset{\frac{z_4}{\lambda}}{.8\,\Delta z^{3\mathrm{D}}}$	$\overset{\frac{z_5}{\lambda}}{\frac{1-\sum_{i=2}^{4} z_i}{2}}$

(e)

$\overset{\frac{z_1}{\lambda}}{\frac{1-\sum_{i=2}^{5} z_i}{2}}$	$\overset{\frac{z_2}{\lambda}}{\Delta z^{3\mathrm{D}}}$	$\overset{\frac{z_3}{\lambda}}{.5\,\Delta z^{3\mathrm{D}}}$	$\overset{\frac{z_4}{\lambda}}{.5\,\Delta z^{3\mathrm{D}}}$	$\overset{\frac{z_5}{\lambda}}{\Delta z^{3\mathrm{D}}}$	$\overset{\frac{z_6}{\lambda}}{\frac{1-\sum_{i=2}^{5} z_i}{2}}$

(f)

$\overset{\frac{z_1}{\lambda}}{\frac{1-\sum_{i=2}^{6} z_i}{2}}$	$\overset{\frac{z_2}{\lambda}}{.75\,\Delta z^{3\mathrm{D}}}$	$\overset{\frac{z_3}{\lambda}}{.35\,\Delta z^{3\mathrm{D}}}$	$\overset{\frac{z_4}{\lambda}}{.4\,\Delta z^{3\mathrm{D}}}$	$\overset{\frac{z_5}{\lambda}}{.35\,\Delta z^{3\mathrm{D}}}$	$\overset{\frac{z_6}{\lambda}}{.75\,\Delta z^{3\mathrm{D}}}$	$\overset{\frac{z_7}{\lambda}}{\frac{1-\sum_{i=2}^{6} z_i}{2}}$

(g)

$\overset{\frac{z_1}{\lambda}}{\frac{1-\sum_{i=2}^{7} z_i}{2}}$	$\overset{\frac{z_2}{\lambda}}{.7\,\Delta z^{3\mathrm{D}}}$	$\overset{\frac{z_3}{\lambda}}{.3\,\Delta z^{3\mathrm{D}}}$	$\overset{\frac{z_4}{\lambda}}{.3\,\Delta z^{3\mathrm{D}}}$	$\overset{\frac{z_5}{\lambda}}{.3\,\Delta z^{3\mathrm{D}}}$	$\overset{\frac{z_6}{\lambda}}{.3\,\Delta z^{3\mathrm{D}}}$	$\overset{\frac{z_7}{\lambda}}{.7\,\Delta z^{3\mathrm{D}}}$	$\overset{\frac{z_8}{\lambda}}{\frac{1-\sum_{i=2}^{7} z_i}{2}}$

Table 5.1: Templates for the z position of the element-edge boundary nodes as a function of the number of levels: (a) 2 levels, (b) 3 levels, (c) 4 levels, (d) 5 levels, (e) 6 levels, (f) 7 levels, (g) 8 levels.

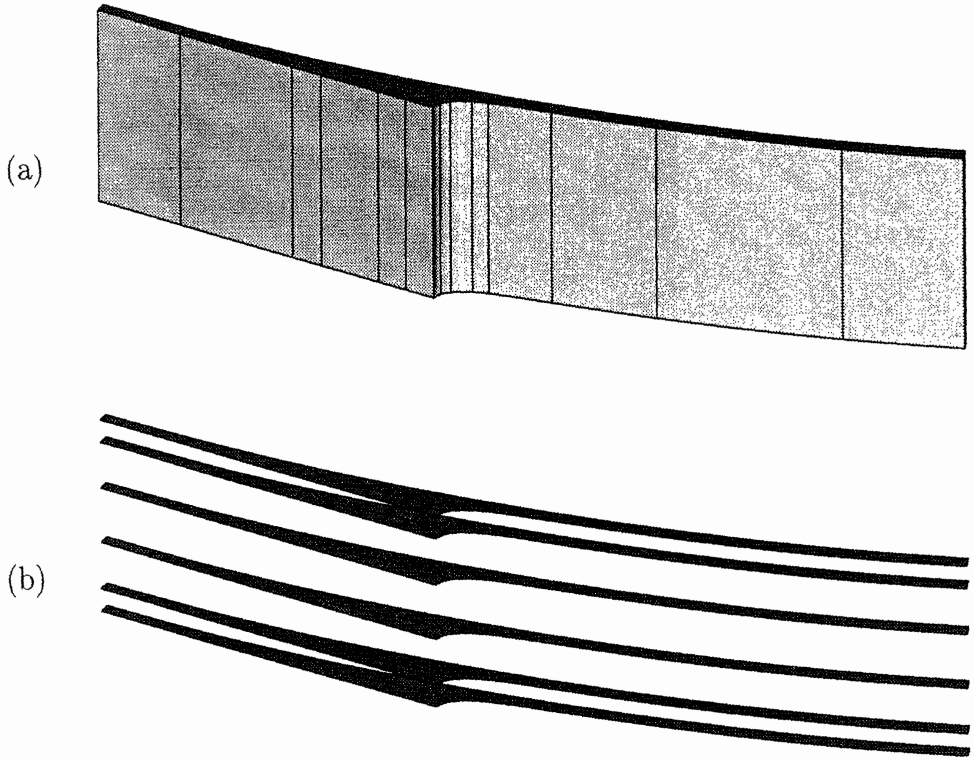

Figure 5-3: Three-dimensional domain and corresponding template slices (6) of the domain consisting of 15 elements in 1 level using interpolants of 5th order.

$\mathrm{R3}^{\mathrm{3D}}$ Discretize the individual levels based on the position of the element boundary sides normal to the extrusion direction; the z position of the internal nodes is determined using a template similar to that of Fig. 4-5 using the z coordinate as the parameterization parameter.

Slice the three-dimensional domain into z planes corresponding to the discretization performed in step $\mathrm{R2}^{\mathrm{3D}}$. Each slice is topologically equivalent to the two-dimensional domains described in Chapter 4 but include the spanwise velocity as an additional field quantity.

$\mathrm{R4}^{3\mathrm{D}}$ Apply the two-dimensional remeshing procedure R to each two-dimensional slice without changing the position of the outflow boundary (step R2). The spanwise velocity is also mapped onto the new mesh. In this step, more elements per level, or higher order interpolants can be used to increase the resolution.

$\mathrm{R5}^{3\mathrm{D}}$ Reconstruct three-dimensional mesh based on the two-dimensional remeshed slices and the template used in step R3.

Limitations

The remeshing procedure $\mathrm{R}^{3\mathrm{D}}$ does not allow for the study of re-entrant[67] ribs since, as shown in Fig. 5-4, slices with planes (constant z) of the three-dimensional domain are not topologically equivalent, since the rib geometry is not a single value function of z. Since the slices are not topologically equivalent, the two-dimensional remeshing procedure R is not applicable. The decoupled template scheme, consisting of a two-dimensional template and a spanwise template, obviously, cannot be extended to study re-entrant ribs. Global domain decomposition and field quantity mapping algorithms must be implemented in order to perform the remeshing of domains that have re-entrant ribs[67].

5.3 Numerical Procedure

To study the three-dimensional ribbed states, the two-dimensional steady flow field is first obtained using the procedures described in Chapter 4 . The geometry is then extruded in the spanwise direction to the desired domain depth λ and domain extent in the downstream direction. The free surface is then perturbed sinusoidally, with amplitude $A_o^{3\mathrm{D}}$ in the direction of the local free surface normal (which lies in the $x \times y$ plane since there is no spanwise curvature yet), and spanwise wavelength λ. The (nondimensional) initial amplitude of the perturbation $A_o^{3\mathrm{D}}$ is taken to be .01 in most cases. In some cases, a smaller amplitude for the perturbation was considered in order to study in detail the initial evolution from the unstable two-dimensional steady state. A blending interpolation is then performed in the last element in order to satisfy the

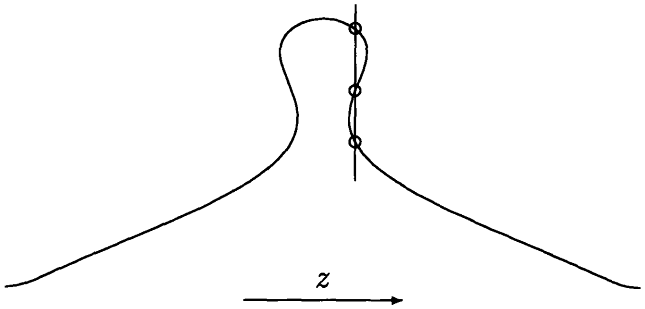

Figure 5-4: Schematic of re-entrant rib geometry for which the remeshing procedure can not be used since the rib geometry is not a single valued function of z.

boundary condition of $A_o^{3D} \rightarrow 0$ as $\theta \rightarrow \theta_{\partial\Omega_3}$. This geometry is then integrated in time. The stopping criterion is critical since rib growth can be relatively slow. If the perturbed geometry is integrated in time until the maximum velocity normal to the free-surface falls below a preset tolerance, say when $\max_{\partial\Omega_4 \bigcap \partial\Omega_5} u_i n_i < .0025$, the geometry in most cases can be deemed to be close enough to the actual steady state. This criterion fails for slightly supercritical Ca for which very small amplitude ribs are obtained since the magnitude of the velocity components on the free surface are small due to the large time constants associated with the rib growth. A better stopping criterion can be implemented based on Eq. (3.16). If an error of magnitude ε (e. g. $\varepsilon = .01$), is acceptable for the rib amplitude measured by A_s, since the time scale for approaching the steady state is known from Eq. (3.16), the corresponding limit on the normal velocity at the midplane can be estimated and scales as:

$$\max_{\partial\Omega_4 \bigcap \partial\Omega_5} u_i n_i < \frac{\varepsilon}{2\,Ca\,\frac{\lambda}{2\pi}} A_s \leq \lim_{t\rightarrow\infty} \frac{\varepsilon}{2\,Ca\,\frac{\lambda}{2\pi}} A_s \tag{5.2}$$

where A_s is used as an estimate of the final total disturbance amplitude since this quantity is not known *a priori*. Another way to determine the stopping criterion is through an eigenvalue interpretation. The approach to the steady state can be considered as governed by a linear operator, $\mathcal{L}$ such that

$$u_{i,t} = \mathcal{L}_{ij}\, u_j \tag{5.3}$$

$$\mathcal{L}_{ij}\, uj = \lambda\, u_i \tag{5.4}$$

$$\mathcal{L}\, u_i = f_i \tag{5.5}$$

$$\Delta u_i \leq \frac{1}{\lambda_{\text{min}}} \Delta f_i \tag{5.6}$$

where Δu_i can be considered as the error in the velocity, λ_{min} is the smallest eigenvalue of the linear operator $\mathcal{L}_{ij}$ and is equal to the time scale given by Eq. (3.16), and Δf_i is the residual that from the steady state.

The computational time required to achieve a steady state, starting with the initial two-dimensional perturbed domain, is on the order of 50-600 hours on 16 nodes of an Intel i860 Hypercube and is a function of the capillary number Ca and the domain depth λ studied. The high computational cost is a direct consequence of the explicit treatment of the domain evolution and the resulting restrictive time step. In order to decrease the computational costs, semi-implicit procedures similar to those used in two dimensions should be pursued.

5.4 Extensions of Remeshing Procedure

Due to the modular nature of the remeshing procedure and the decoupling of the z direction template from the two-dimensional template several extensions or uses of the procedure can readily be effected.

5.4.1 Mesh Adaptation

Initially, when the free surface is not greatly deformed, relatively few levels of elements in the spanwise direction suffice; as the free surface deforms, more resolution is required. With this in mind, few levels can be used while the free surface is not greatly deformed and when the geometry requires it, the number of levels can be increased. This increase in resolution is readily effected by introducing a new template, with more levels, in step $R2^{3D}$ of the remeshing procedure R^{3D}. An example of this evolution, with time-varying spanwise resolution, towards the steady ribbed state is shown in Fig. 5-5.

In several cases, the simulations that required higher resolution to resolve the steady state were repeated starting from the initial extruded geometry with the infinitesimal spanwise perturbation, but using the high resolution throughout. The same steady states were achieved, and example is shown in Fig. 7-4, though at a prohibitively high computational cost. The ratio of the computational times required to achieve the steady states shown in Figs. 5-5 and 7-4, was on the order of 10.

5.4.2 Continuation

Once a steady ribbed state is obtained for a given geometry, capillary number, and wavelength, $\{D, Ca, \lambda\}$, instead of starting from the perturbed extruded two-dimensional geometry to obtain the steady ribbed state at a different λ, continuation schemes and proper remeshing procedures reduce the computational cost to obtain a new steady ribbed state (different λ) to on the order of 50-200 hours of computer time. The simplest, yet effective, continuation method is to stretch (compress) the domain in the spanwise direction by scaling the z position and the spanwise velocity, u_3, by the ratio $\lambda_{\text{new}}/\lambda_{\text{old}}$ where λ_{new} is the desired wavelength and λ_{old} is the wavelength of the steady state already obtained as shown in Fig. 5-6. This approach is successful since ribs do not radically change topology, and due to the creeping nature of the flow, any incompatibilities between the free surface geometry and the flow field will be eliminated rapidly. In addition to stretching, an efficient method for the study of ribbed states is that of replication. The steady ribbed state obtained for $\lambda/2$ (or thereabouts and then properly stretched) is replicated in order to create an initial condition (ribbed) that now has a spanwise length of λ and twice the degrees of freedom as shown in Fig. 5-7.

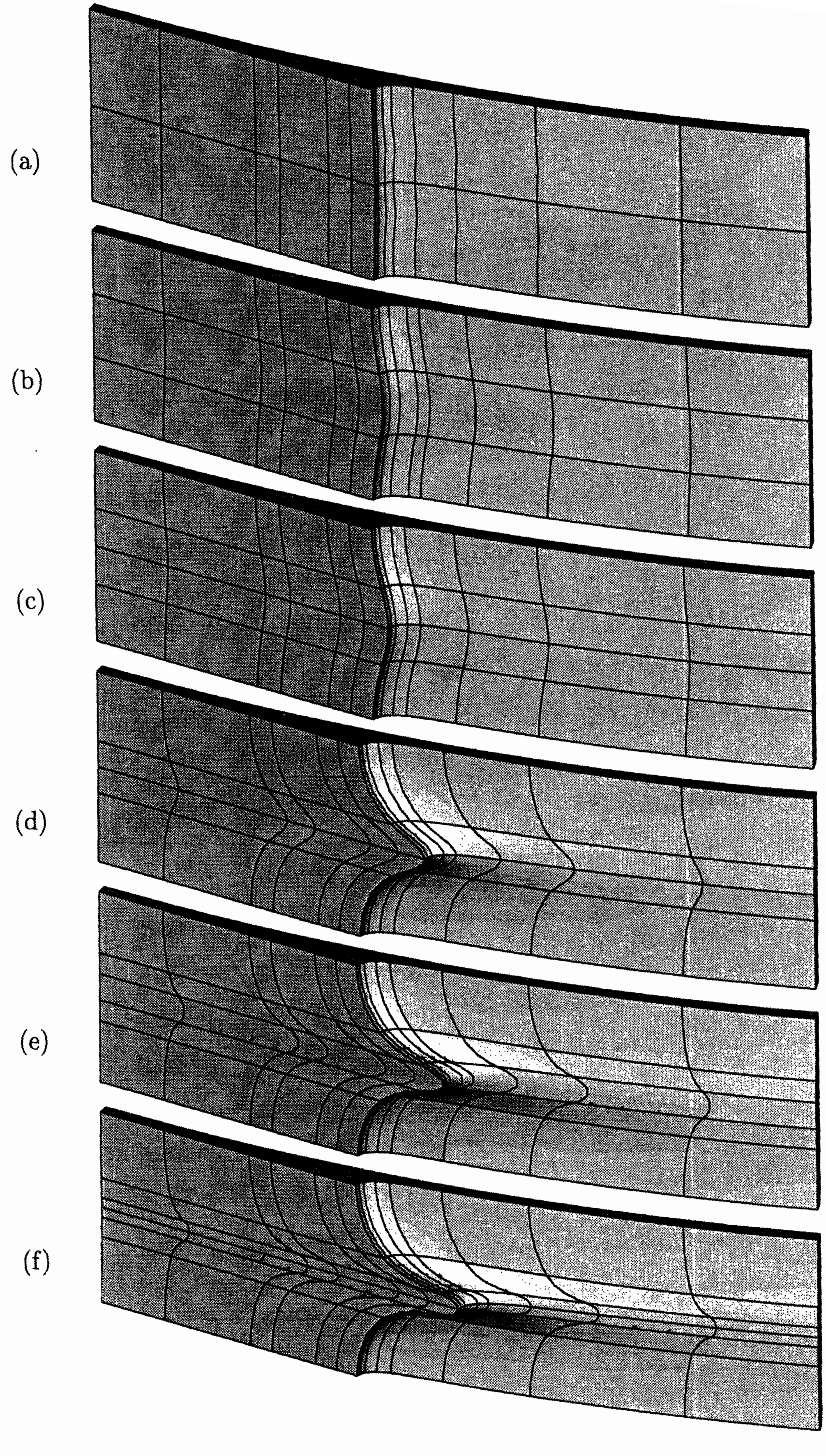

Figure 5-5: Evolution to a steady three-dimensional ribbed-state displaying the adaptive spanwise template, for $\lambda = 10$, $D = 200$ and $Ca = 3.14$.

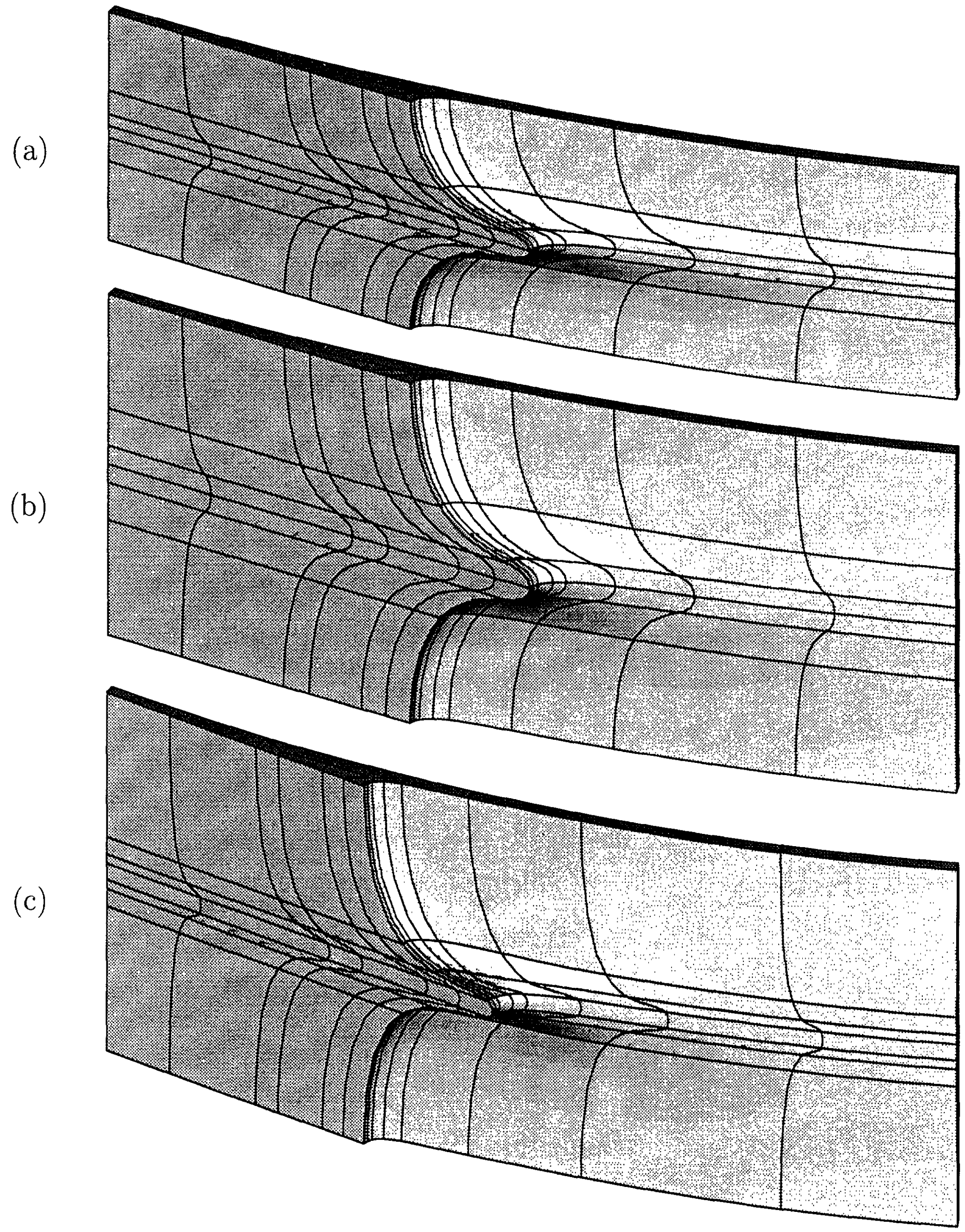

Figure 5-6: Example of continuation scheme to generate initial condition for $\lambda = 15$ (b) based on the steady-state for $\lambda = 10$ (a). The initial condition was integrated until a steady-state was achieved (c), for $\lambda = 15$, $D = 200$ and $Ca = 3.14$.

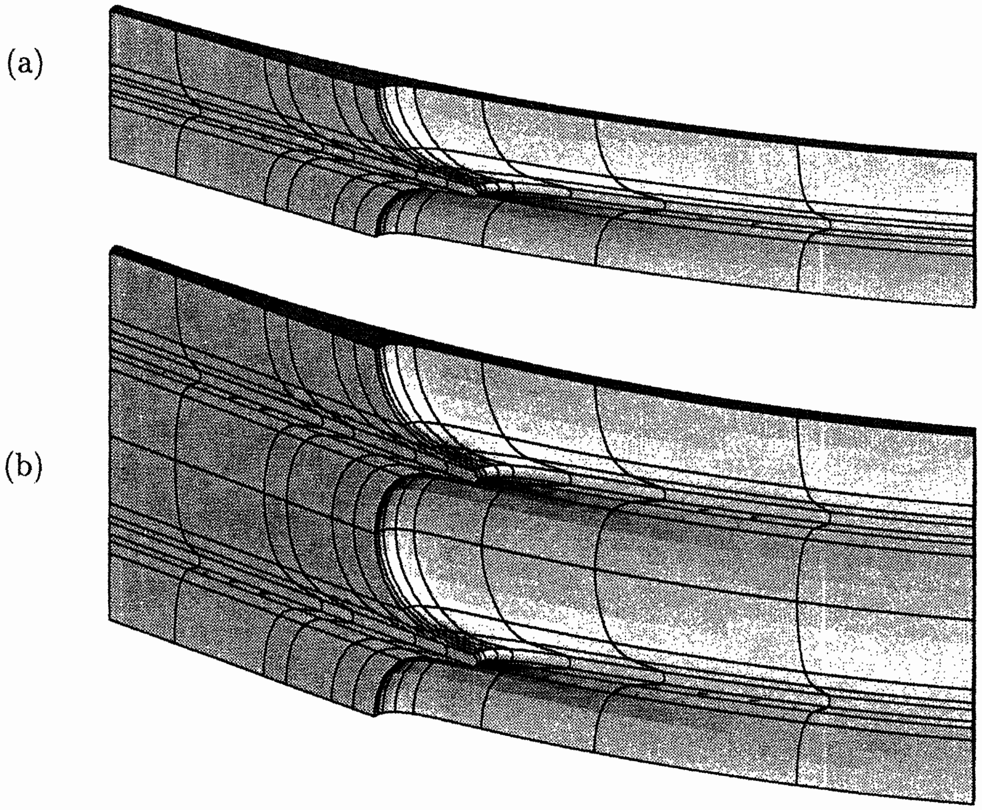

Figure 5-7: Example of continuation scheme to generate initial condition with two ribs of total spanwise length λ (b) based on the replication of the steady ribbed state for spanwise length $\lambda/2$ (a) for $D = 200$ and $Ca = 3.16$.

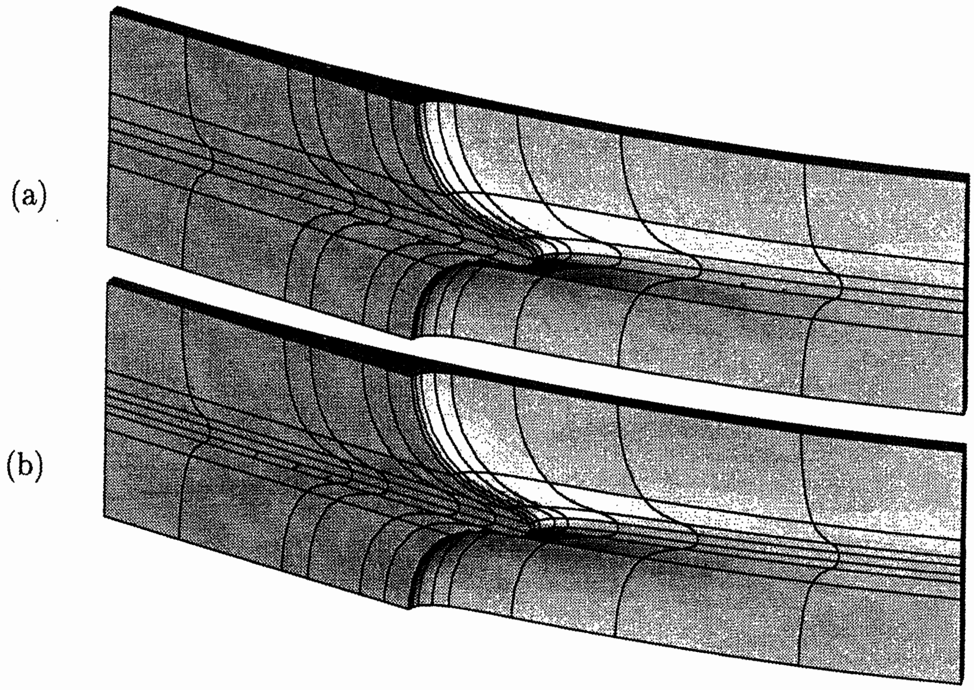

Figure 5-8: Example of continuation used for verification of the steady three-dimensional ribbed-state for $\lambda = 10$, $D = 200$, and $Ca = 3.14$ obtained using $\{15, 6, 5\}$ by continuation using a higher resolution, in this case $\{15, 7, 7\}$.

5.4.3 General Mesh Refinement

Another by-product of the remeshing procedures implemented is the relatively inexpensive verification of the accuracy of the results obtained. If desired, the computed steady ribbed states can be mapped onto a much finer mesh (more spanwise levels, and higher-order elemental interpolants), and then integrated further in time. If we do not observe significant changes in the meniscus geometry, we can conclude that the steady states obtained with the "coarse" mesh is, indeed, correct. An example of such a mapping to a finer mesh is shown in Fig. 5-8.

5.4.4 Limitations

Finally, it should be noted that the three-dimensional methods used for remeshing and continuation guarantee that the steady states obtained are correct but not uniqueness due to the non-linear nature of the problem as is confirmed in Chapter 7. In additio the remeshing methods used cannot study ribs that evolve into a re-entrant topology.

5.5 Limitations of Numerical Methods

In summary, the methods described above allow for the study of the evolution from the unstable two-dimensional steady-states to the stable three-dimensional ribbed steady-states via a time marching approach. The time marching scheme and the stopping criterion used allow for the possibility that after forming the steep ribs, an even "slower" process might begin not described by the mechanisms presented above and thus not captured by the stopping criterion implemented. We have developed remeshing algoritms to allow for the study of the greatly deformed geometries that arise but due to the limitations of the remeshing schemes re-entrant geometries cannot be studied which ave been observed experimentaly for certain flow conditions with non-Newtonian fluids. In order to decrease the excesive computational time, resulting from the explicit treatment of the kinematic condition of the free-surface, we developed a time-dependent spanwise resolution scheme that allows for the use of low-resolution (lower computational cost) when the free-surface is not greatly deformed and high-resolution only when required. An implicit treatment of the kinematic condition will relax the stability limitations on the time-step but on the other hand will increase the problem size and will not allow for the fast iterative solution via preconditioned conjugate gradient iteration.

Chapter 6

Two-dimensional results

In this chapter we first present qualitative results for the two-dimensional problem, and then perform quantitative comparisons with results reported by Coyle et al[12]. Our discussion is brief, intended only as a point of departure for the three-dimensional considerations.

We first discuss, qualitatively, the dependence of the flow geometry and flow field on the two governing parameters, the roll diameter to gap ratio, D, and the capillary number Ca. Figure 6-1 (a-c) shows the dependence of meniscus geometry on the capillary number Ca as the rollers are brought closer together, from $D = 40$ (a), to $D = 200$ (b), and to $D = 1\,000$ (c), respectively. Figure 6-2 (a-c), on the other hand, shows the dependence of the meniscus geometry as the rollers are changed keeping the gap constant, for $D = 40$ (a), $D = 200$ (b), and $D = 1\,000$ (c), respectively. In both cases, increasing Ca, brings the meniscus closer to the nip. This movement is only gradual for high Ca while it is dramatic in the low Ca range. This last effect is more pronounced for larger gap separations (smaller D). The downstream migration of the meniscus with decreasing capillary number is accompanied by a qualitative change in the flow field: for low Ca, a recirculation region appears near the meniscus, as shown in Fig. 6-3 (a-c).

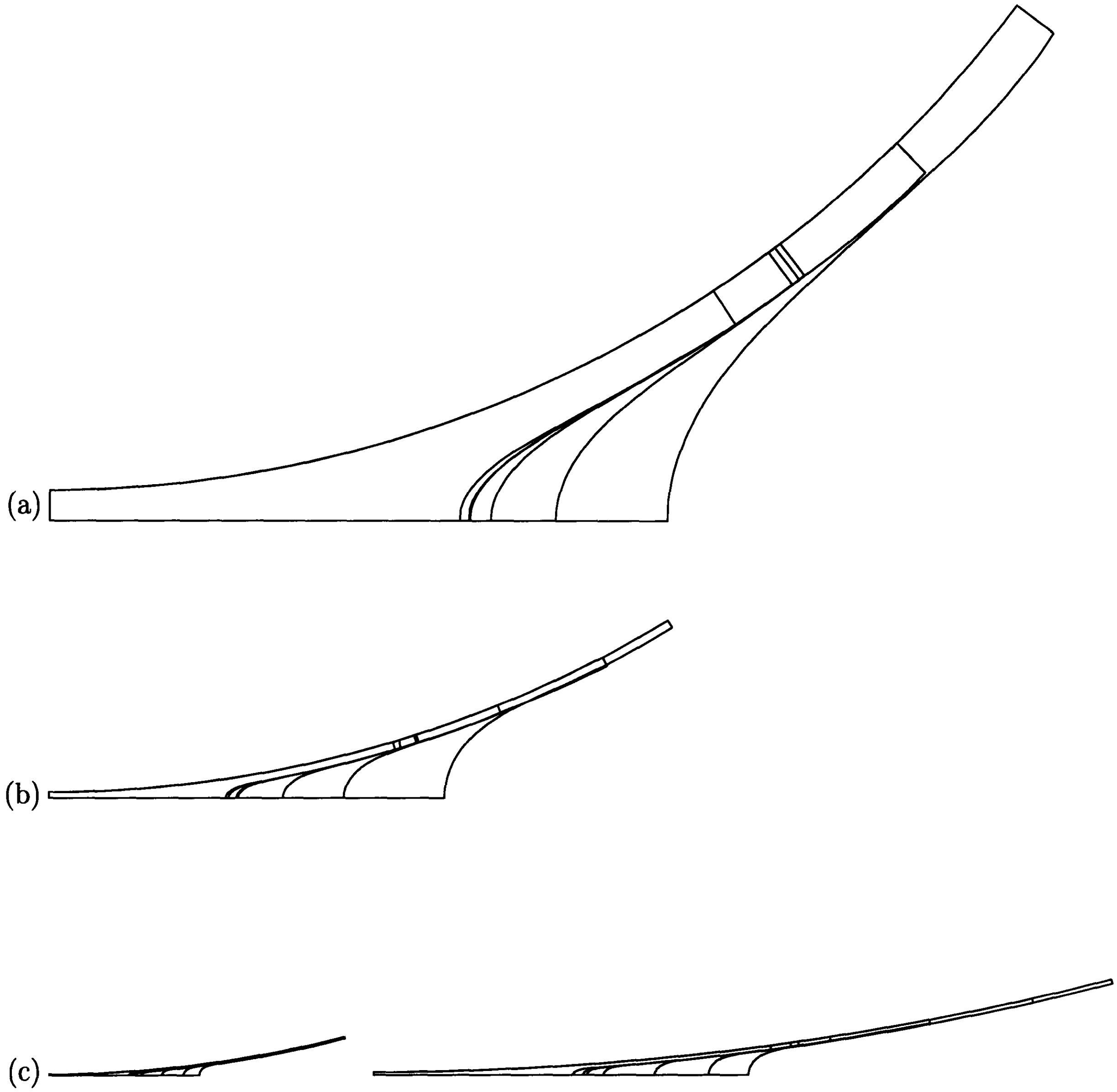

Figure 6-1: Two-dimensional steady meniscus geometries as the rollers are brought closer together: for (a) $D = 40$, (b) $D = 200$, and (c) $D = 1000$, as a function of capillary number: $Ca = .0316, .1, .316, 1, 3.16, 100$.

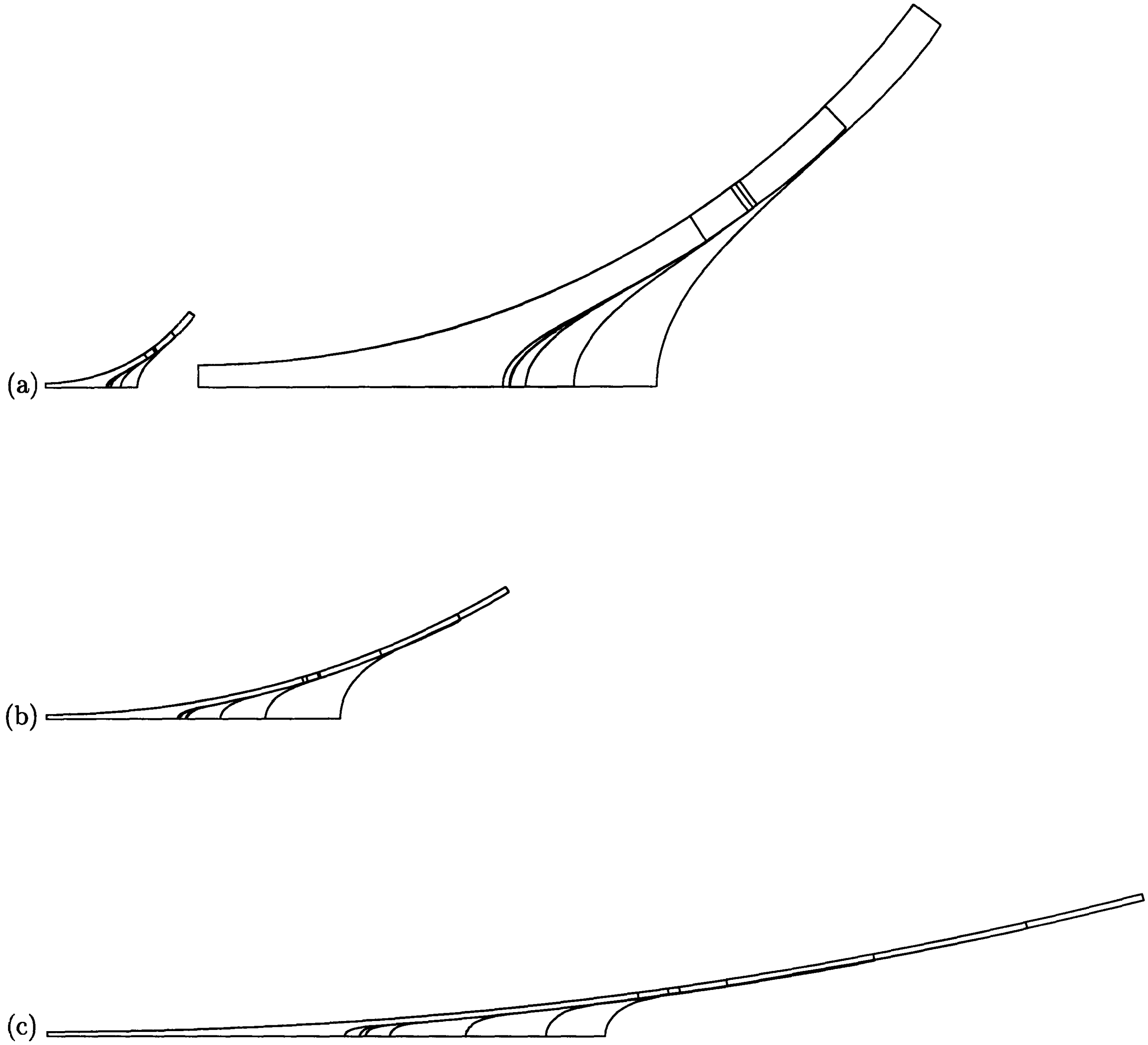

Figure 6-2: Two-dimensional steady meniscus geometries for equal gaps using different rollers: for (a) $D = 40$, (b) $D = 200$, and (c) $D = 1000$, as a function of capillary number: $Ca = .0316, .1, .316, 1, 3.16, 100$.

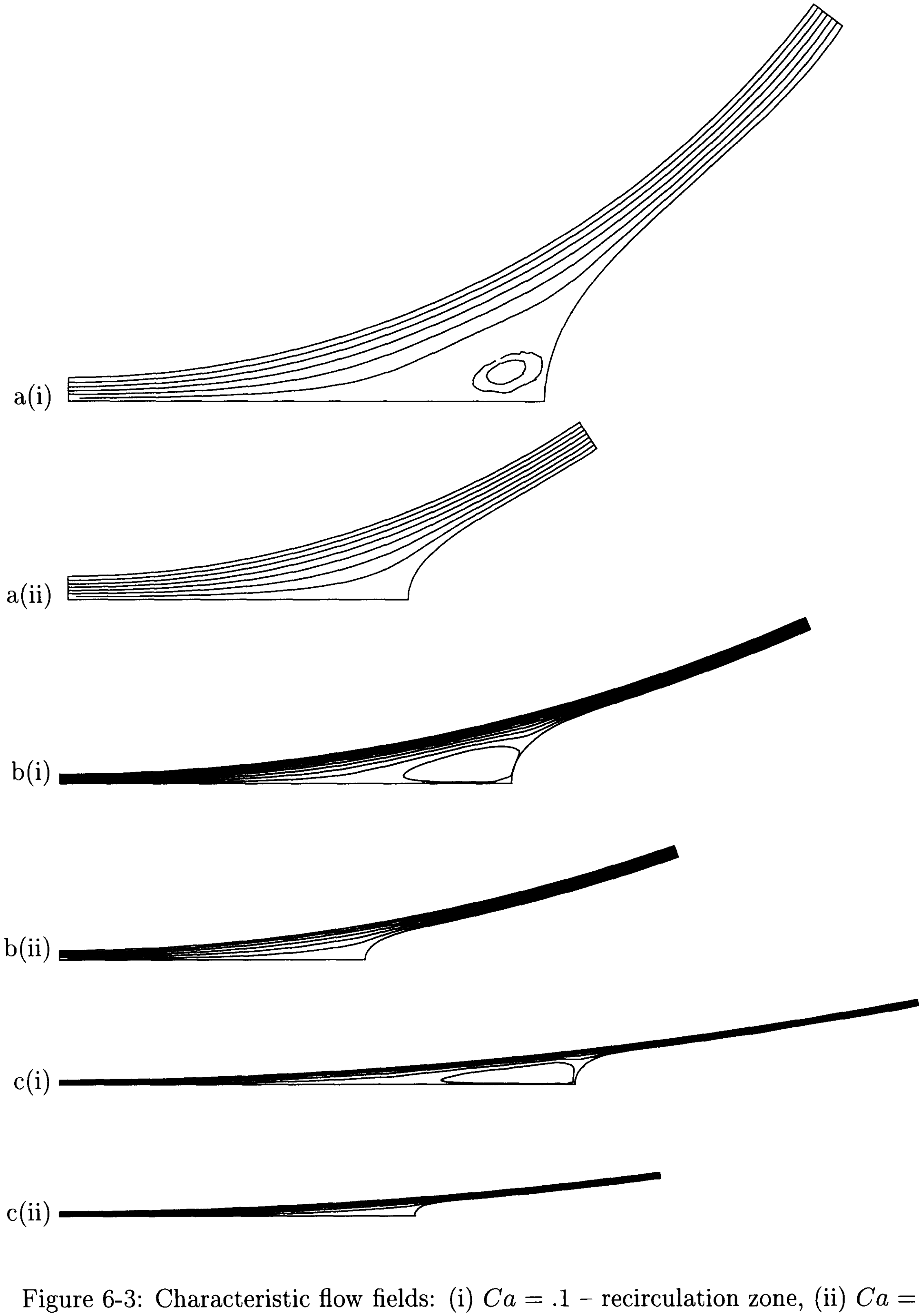
a(i)
a(ii)
b(i)
b(ii)
c(i)
c(ii)

Figure 6-3: Characteristic flow fields: (i) $Ca = .1$ – recirculation zone, (ii) $Ca = 1$ – no recirculation zone, for (a) $D = 40$, (b) $D = 200$, and (c) $D = 1000$.

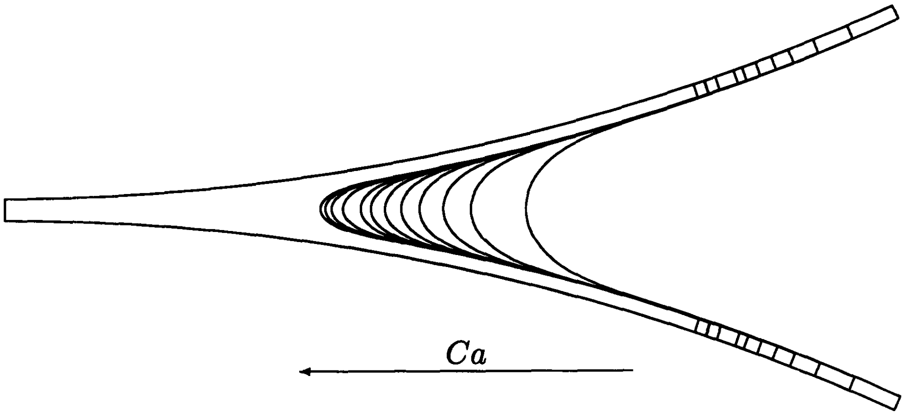

Figure 6-4: Two-dimensional steady meniscus geometry for full domain – no imposed symmetry – as a function of the capillary number $Ca = .05 \rightarrow 100$ and $D = 200$.

As described in Chapter 4, we also performed calculations using the full domain, not considering the symmetry of the flow fields. Representative results are shown in Fig. 6-4, the two-dimensional steady meniscus geometry for $D = 200$ as a function of Ca. The meniscus geometry obtained for the full domain does not exhibit noticable differences compared to the results for the symmetrized domains (always less than the tolerance used to determine the steady state). The computational time to obtain the steady state, on the other hand, was on the order of 2 to 8 times longer compared to the symmetric case and was a function of the Ca: more gains in computational time we obtained for the higher Ca which is in agreement with the fact that the solver is more efficient for smaller Ca.

We now turn to three quantitative measures of the flow field and geometry: the volume flowrate through the nip, Q; the location of the stagnation point on the splitting meniscus, $x_s^{2\mathrm{D}}$; and the location of the first stagnation point downstream from the nip along the symmetry plane, $x_o^{2\mathrm{D}}$. The dependence of the flowrate Q on the capillary number Ca, for $D = 40$, 200 and 1000, is shown in Fig. 6-5. Figure 6-5 shows the weak dependence of the flowrate, and thus the nip pressure, through Eq. (2.11), on the capillary number Ca and on the geometric parameter D. With increasing capillary number Ca there is a monotonic decrease in the flowrate Q. This property is also observed with increasing D, though it is not as great.

The location of the splitting meniscus is shown in Fig. 6-6 as a function of the capillary number Ca for $D = 40$, 200, and 1000. The position of the meniscus, $x_s^{2\mathrm{D}}$, is scaled by the geometric factor $\sqrt{2\,D}$, which appears in lubrication theory analysis. For most of the range, this factor represents the effect of D. When the recirculation sets in, the three curves no longer collapse. This can be explained by observing that the one-dimensional assumption used in lubrication theory analysis breaks down.

Figure 6-7 shows the location of the first stagnation point downstream from the nip along the symmetry plane, $x_o^{2\mathrm{D}}$, as a function of the Ca and different geometries D. To determine the onset of the recirculation zone in the flow field, Fig. 6-7 need just be compared with Fig. 6-6. When the two plots overlap, no recirculation is present, and while the two plots do not coincide, a recirculation zone is present. For high Ca, only one stagnation point is observed along the symmetry plane, $\partial\Omega_5$, that is, the stagnation point observed on the splitting meniscus is the first stagnation point observed downstream of the nip. As the capillary number is decreased, near $Ca \sim .8$, a second stagnation point arises, signaling the presence of a recirculation zone. The location of the first stagnation point downstream of the nip is weakly dependent on Ca indicating that it is mainly determined by the viscous pressure gradient in the fluid. Once a recirculation zone appears, the position of the first stagnation point is slightly altered though not greatly as a function of the Ca.

Finally we validate our results by comparing them with those reported by Coyle et al[12]. Coyle et al[12] compare their results based on finite element analysis with results based on asymptotic analysis. Qualitatively our results are in agreement, and as can be seen in Table 6.1 and Fig. 6-8, there is quantitative agreement as well.

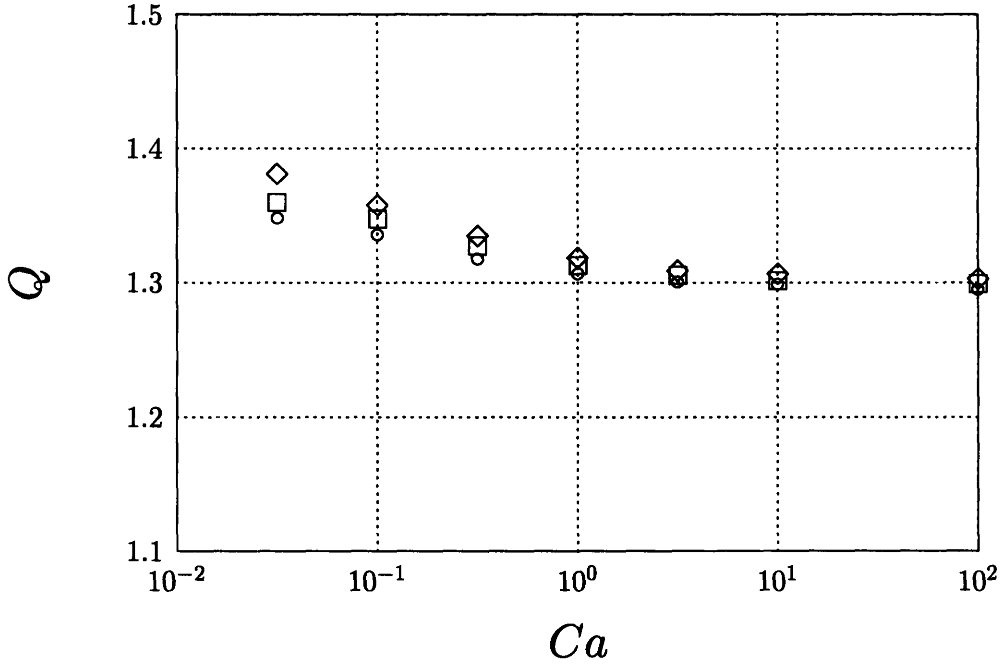

Figure 6-5: Non-dimensional volume flowrate, Q, as a function of Ca for $D = 40$ (◇), $D = 200$ (□), and $D = 1000$ (○).

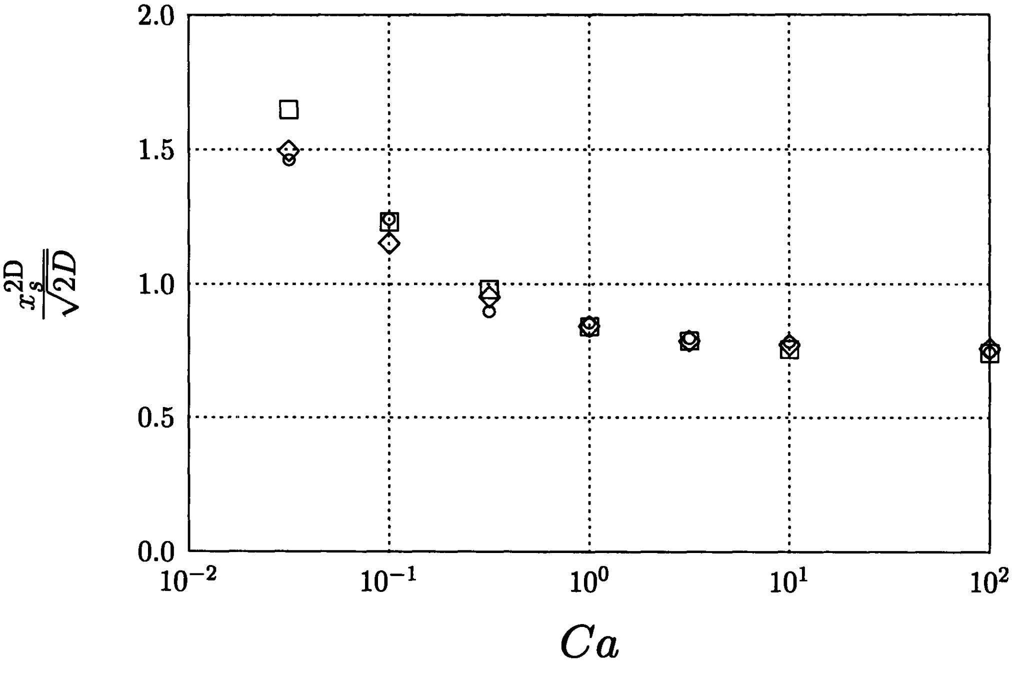

Figure 6-6: Film split location, x_s^{2D}, as a function of $Ca = .0316, .1, .316, 1, 3.16, 100$ for $D = 40$ (◇), $D = 200$ (□), and $D = 1000$ (○).

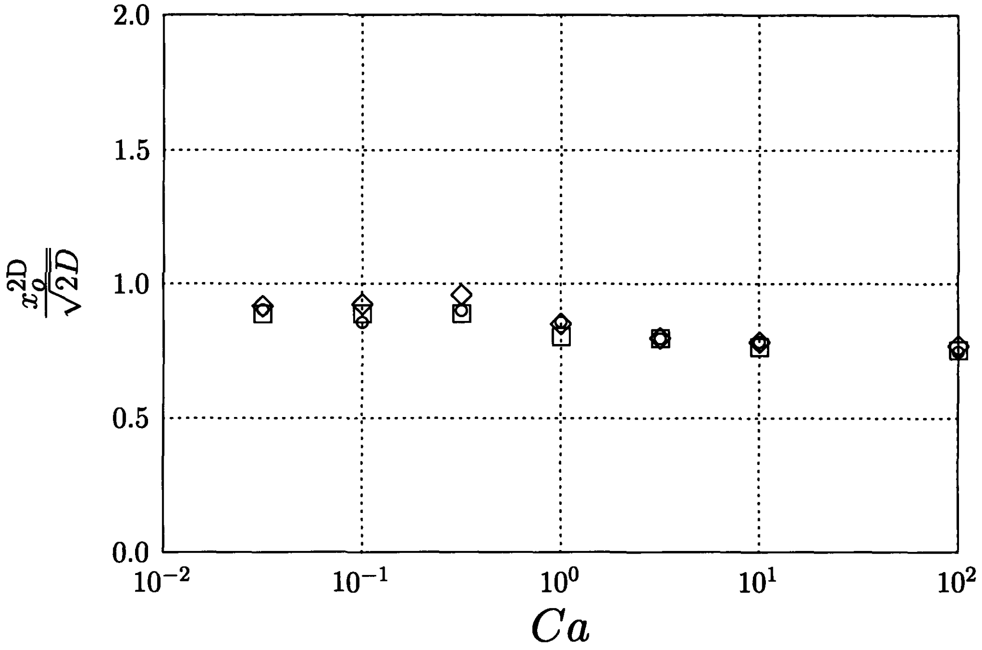

Figure 6-7: Position of first stagnation point downstream from nip, x_o^{2D}, as a function of Ca for $D = 40$ (◇), $D = 200$ (□),and $D = 1000$ (○).

	Current	Coyle et al[12]	
	$D = 500$	Asymptotic Analysis	Finite Elements
Q	1.2955	1.290	1.293
x_s^{2D}	.729031	.7230	.7290

Table 6.1: Flowrate, Q, and position of the splitting meniscus, x_s^{2D}, in the limit of $Ca \gg 1$.

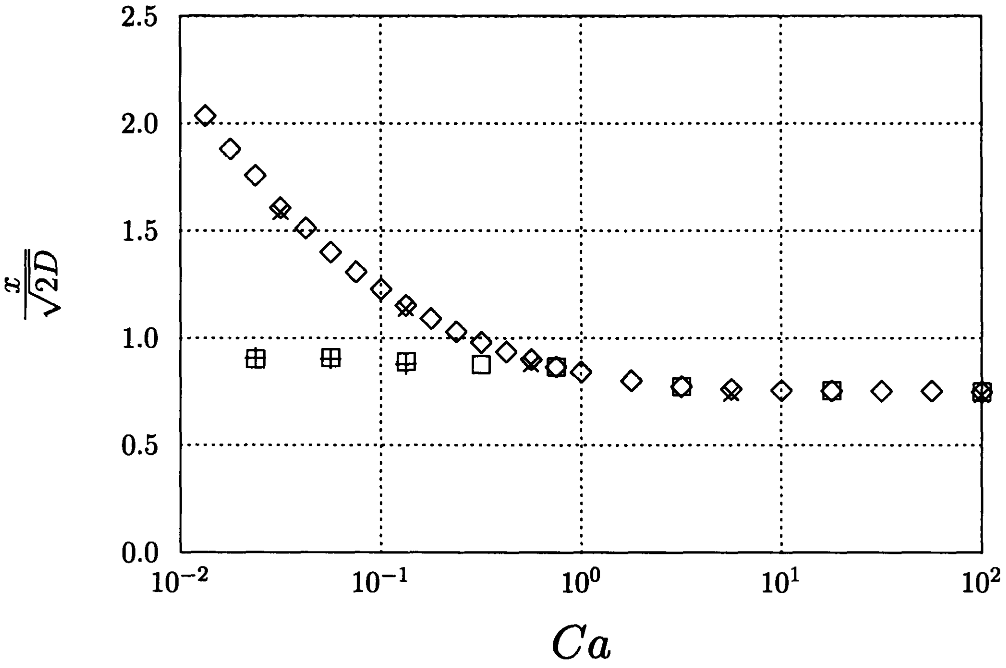

Figure 6-8: Film split location, x_s^{2D}, as a function of Ca for $D = 200$: this study ◇; Coyle et al[12] ×. First stagnation point downstream from nip, x_o^{2D}: this study □, Coyle et al[12] +.

Chapter 7

Three-dimensional results

In this chapter we present simulation results for the unsteady three-dimensional free-surface fluid flow problem. The calculations serve the purpose of validating and quantifying the model of Chapter 3, and of demonstrating our three-dimensional simulation methodology. We first compare the short-time behavior predicted by our simulations with the results based on linear stability theory reported by Coyle et al[14]. We then present the evolution from a perturbed unstable two-dimensional steady flow geometry to a stable three-dimensional steady ribbed state, and compare these results with the "predictions" of the analysis of Chapter 3. Finally, we present steady ribbed results for selected spanwise periodicity lengths, λ, and supercritical capillary numbers, $Ca > Ca_c$.

7.1 Nonlinear Evolution to Steady Ribbed States

7.1.1 Comparison with Linear Stability

Coyle et al[14], based on linear stability analysis of symmetric forward-roll coating, report the critical capillary number, Ca_c, and the critical wavelength, λ_c, for different geometries, as defined by D. In addition, for a limited combination of D and Ca, they present the growth-rates, γ, of the infinitesimal perturbations as a function of their wavenumber $\beta = \pi/\lambda$. Coyle et al[14] mention that there are some limitations on the accuracy of the growth-rates predicted far from marginality ($\gamma = 0$) due to approximations performed in their numerical procedure; terms arising from the time derivatives from the momentum equations were neglected. The procedure implemented by Coyle el al[14] follows closely that of Ruschak[58]. Both Coyle el al[14] and Ruschak[58] claim that the approximations are valid as long as the resulting time constant for the growth of the disturbance is long compared to that of the base flow. As will be confirmed below, this approximation is valid for the cases we considered ($Re \ll 1$) since the time constants associated with disturbance growth (or decay) are relatively large and thus, the reported growth-rates should be small and relatively accurate. We use the information presented by Coyle et al[14] to compare the short-time behavior of our non-linear simulations with predictions of the short-time behavior based on linear stability analysis. We note that our methods are not an efficient means to determine marginal stability or growth-rates due to the fact that the time constants get larger (and thus more computation) as marginality is approached; this phenomena is commonly refered to as critical slowing.

We present results for $D = 40$, $Ca = 15$, and $\lambda = \lambda_c = 9$ which Coyle et al[14] report to be unstable ($Ca = 15 > Ca_c = 7$ and $\beta_c = \pi/\lambda_c = \pi/9$ for $D = 40$); the reported growth rate (appropriately scaled) for the spanwise periodic disturbance of wavenumber $\beta = \beta_c = \pi/9$ is approximately $\gamma \cong .01$ (see Fig. 5 of Coyle et al[14]). The initial geometric (and velocity) perturbation we impose on the extruded two-dimensional steady state geometry (see Chapter5) does not correspond to the eigenfunction with wavenumber $\beta = \beta_c$, but rather to a linear combination of eigenfunctions of wavenumber $\beta = m\,\beta_c$ for $m = 1, \ldots, \infty$. Due to this, the initial growth of the imposed perturbation will not correspond to that given by linear stability analysis. However, the eigenfunction with $\beta = \beta_c$ will be preferentially amplified and thus we should observe, after some time, growth rates relatively close to that predicted by linear stability.

We look at the evolution of the disturbance at the midplane as measured by the "total" disturbance amplitude given by $A_s = \left(\max x_s^{3D} - \min x_s^{3D}\right)/2$ (this is possible since the profile at the midplane remains mostly monochromatic). We plot in Fig. 7-1 the evolution of the amplitude A_s as a function of time. Initially, the disturbance exhibits growth greater than that indicated by linear stability analysis. As mentioned above, this can be attributed to the fact that the initial disturbance is not spatially equal to the eigenfunction of wavenumber β_c; it does not exhibit the exponential decay of amplitude in the downstream direction described by Coyle et al[14], but rather it is of constant, and finite, amplitude (initially). The initial "corrective" growth saturates and we observe slower growth with a second change in the growth-rate near $t = 16$. We determined the quantity $\mathrm{d}A_s/\mathrm{d}t$ in the two sub-intervals by performing a least-squares fit to the data in the intervals $t \in [2, 18]$ and $t \in [15, 40]$, respectively. We did not estimate using more advanced techniques the appropriate intervals, but rather determined them by inspection. The growth-rate in what would be the interval for linear growth is determined to be $\gamma = .0107$ which is in good agreement with the growth-rate predicted by linear stability. As mentioned above, after the initial linear growth, the disturbance continues to grow but at a different rate until it eventually reaches a steady state as shown in Fig. 7-1. The final approach to the steady state geometry, given by $\mathrm{d}A_s/\mathrm{d}t$, can be estimated using Eq. (3.16) as .0233. This is in good agreement with our simulation result for the interval $t \in [15, 40]$ which is determined to equal .0292, again by a least squares fit. The two-regime growth is observed in most of the simulations performed (see also Fig. 7-3) as was "predicted" in Chapter 3.

In order to remove the discrepancy with in linear growth interval, specially near $t = 0$, the initial spatial and velocity perturbations to the two-dimensional geometry and flow field respectively, should equal the eigenfunctions corresponding to linear stability analysis (which are unknown to us).

7.1.2 Meniscus Evolution Towards the Steady State

To allow for adequate visualization of the meniscus and the ribs during the evolution towards the steady state, we now present results for $D = 200$; the critical conditions for this geometry reported by Coyle et al[14] are $Ca_c = .32$ and $\beta_c = \pi/\lambda_c = \pi/30$. We first present results for the following set of parameters:

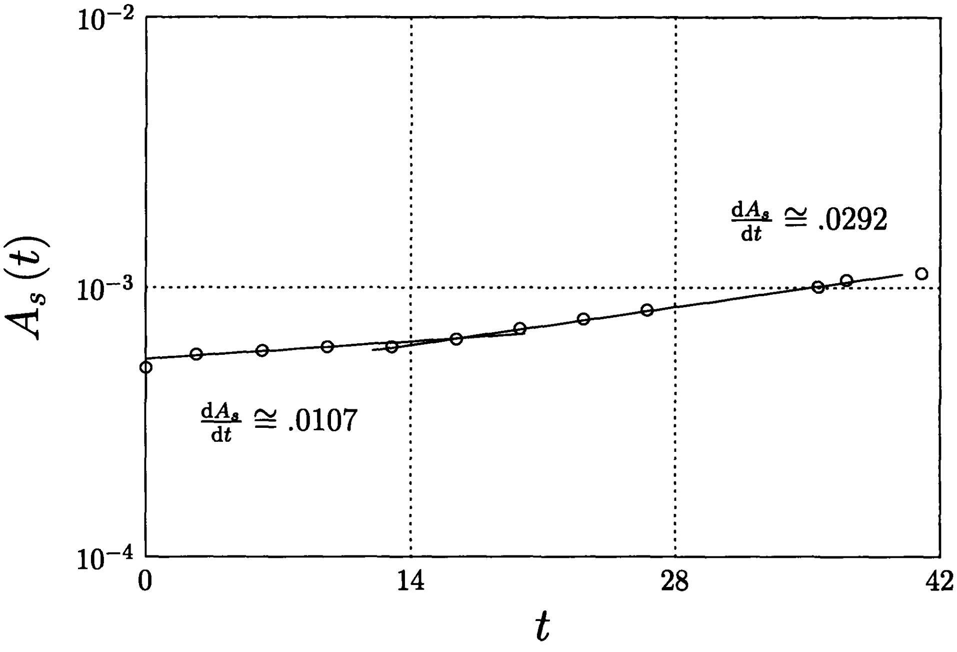

Figure 7-1: Evolution of the meniscus amplitude at the midplane, measured by A_s ($\circ$) for $D = 40$, $Ca = 15$, and $\lambda = 9$, from the slight perturbation to the unstable two-dimensional steady state geometry. A least squares fit of the data for $t \in [2, 18]$ results in a growth rate of $\gamma = .0107$ as indicated by the solid line which is in agreement with that reported by Coyle et al[14]. The growth of the disturbance as it approaches the steady state determined using a least squares fit is given by .0292 in the interval $t \in [15, 40]$ and is in agreement with the value of .0233 given by Eq. (3.16). The resolution used to obtain this result was $\{15, 4, 5\}$.

$D = 200$, $Ca = 5 \gg Ca_c = .32$, and $\lambda = \lambda_c/2 = 15$ (note that $\beta = 2\,\beta_c$ is presumed to be, and is in fact, an unstable mode). The result presented below was originally obtained considering the full non-symmetrized domain and subsequently repeated for the symmetric domain. The results for the evolution of the meniscus profile are virtually indistinguishable. The downstream evolution, in what we term the film region, due to the imperfect symmetry of the initial condition, exhibited non-symmetric transients (of small magnitude) while the original fluid was washed out by the action of the rollers but after this time the flow geometry was symmetric. When the steady states were attained, in other words when the stopping criteria were first satisfied, the two geometries (unsymmetric and symmetric) where again virtually identical. The gain in computational time considering the symmetric domain, for equal resolution, was on the order of 4 for this particular simulation. This gain can be attributed to a decrease in the degrees of freedom, and the improvement in the conditioning of the problem. Since the two results do not differ greatly, we concentrate on discussing the symmetric domain results.

The evolution of the meniscus geometry from the unstable two-dimensional steady state to the stable three-dimensional ribbed steady state is shown in Fig. 7-2. The profiles correspond to the intersection of the free surface with the symmetry plane, $\partial\Omega_4 \bigcap \partial\Omega_5$, for different times. For the resolution $\{15, 7, 5\}$, with approximately 150 000 degrees-of-freedom, the free-surface-velocity-based stopping criterion is satisfied near $t = 64.2$, and thus we deem the geometry to have achieved a steady state. To verify the steady three-dimensional geometry obtained, this solution is then mapped (see Chapter 5) onto a finer mesh $\{15, 8, 7\}$ with approximately 350 000 degrees-of-freedom, and further integrated in time until the stopping criterion was again satisfied, and thus a new steady state is achieved, at $t \cong 66$; the two geometries differ only slightly, leading us to hazard that the results are, indeed, correct. The relaxation time constant associated with finding the new steady state after the mapping onto the fine mesh is large due to the steepness of the ribs. Noise is introduced during remeshing, predominantly at the higher wavenumbers. For ribs that are smaller in amplitude, and thus not as steep, the higher resolution steady state is readily obtained after the

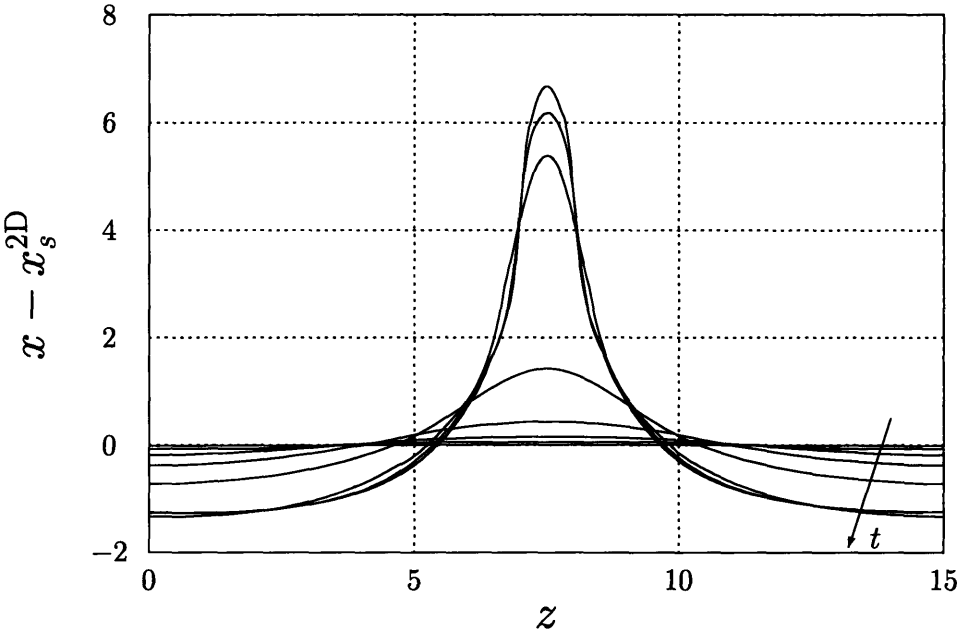

Figure 7-2: Evolution of the meniscus profile at the midplane, $\partial\Omega_4 \cap \partial\Omega_5$, for $D = 200$, $Ca = 5$, and $\lambda = 15$, from the slight perturbation to the unstable two-dimensional steady state position x_s^{2D}, to the three-dimensional stable steady state: $t = 0$, 20, 30, 40, 50, 58.4, 61.6, 64.2.

mapping.

During the evolution to the three-dimensional ribbed state, the average position of $\partial\Omega_4 \cap \partial\Omega_5$, $\overline{x}_s^{3D} = \int_0^\lambda x_s^{3D} dz/\lambda$, does not differ significantly from the meniscus position for the two-dimensional problem, x_s^{2D}; furthermore, the flowrates through the nip for the two-dimensional and three-dimensional flows differ only slightly, less than 1% (note that we do not impose the flowrate through the nip, but rather, impose the pressure at the nip and let the solution procedure determine the flowrate for the value of the imposed nip pressure). Negligible differences between the two-dimensional flowrate and that of the ribbed states is observed in all the results obtained, confirming that, for the range of D, Ca, and λ considered, the total volume flowrate through the nip is not greatly affected by the presence of ribs. The greatest change in flowrate ($<$ 1%) was observed when the ribs present were of great amplitude, $A_s > 3$, indicating that possibly for even more supercritical Ca, ribs can have an effect on the total flowrate and thus the resulting film thickness.

For highly supercritical Ca, as the rib achieves finite amplitude the higher spanwise harmonics will achieve significant amplitude (they initially have a very small amplitude), giving rise to the steepening of the ribs as the steady state is approached. The evolution of the profile $\partial\Omega_4 \bigcap \partial\Omega_5$ can be used to quantify the growth of the various components of the disturbance to the free surface. Figure 7-3 shows the evolution of several amplitudes: the disturbance amplitude given by $A_s = \left(\max x_s^{\mathrm{3D}} - \min x_s^{\mathrm{3D}}\right)/2$; and the amplitudes of the first three Fourier modes, A_1, A_2, A_3, respectively, obtained by performing a Fourier transform of the profile $\partial\Omega_4 \bigcap \partial\Omega_5$. During most of the evolution toward the steady state, the higher wavenumber modes are not noticeable; they do become important, however, when approaching the steady state, in agreement with the steepening of the rib observed in Fig. 7-2. The "fluctuation" after $t = 58.4$ is a direct consequence of a change in the template for the z direction from 6 levels to 7 levels; the increase in resolution filters higher wavenumbers from the profile and this has but a transient effect. The remeshing procedure results in a discrete jump of small magnitude that should be observed in Fig. 7-3 after every new mesh. To avoid confusion, the geometry used to generate the plots was the one before the remeshing procedure. The effects of remeshing are observed during the transient which follows the remeshing; for example, after $t = 58.4$ there is a transient increase in the amplitude of the main low-wavenumber mode and a decrease in the corresponding amplitudes of the higher wavenumber modes which is clearly observed in Fig. 7-2. Similar changes in the high wavenumber content are associated with remeshing and become important when the rib profile is steep, in other words, when the rib profile contains higher wavenumbers. The shown in Fig. 7-2 is

For our initial condition, many of the possible wavenumbers, $\beta = m\,2\,\beta_c = m\,\pi/15$ for at most $m = 1, \ldots, 32$, are linearly unstable. Since we expect that for short times the nonlinear interaction is small, the unstable modes will each grow at approximately the rate determined by linear stability analysis. The fastest growing mode will, initially, not necessarily correspond to $m = 1$ which is the case in Fig. 7-3 where the growth-rate for the mode corresponding to $m = 3$ is greatest. Despite the faster initial growth of higher wavenumber modes, due to the nonlinear interaction between

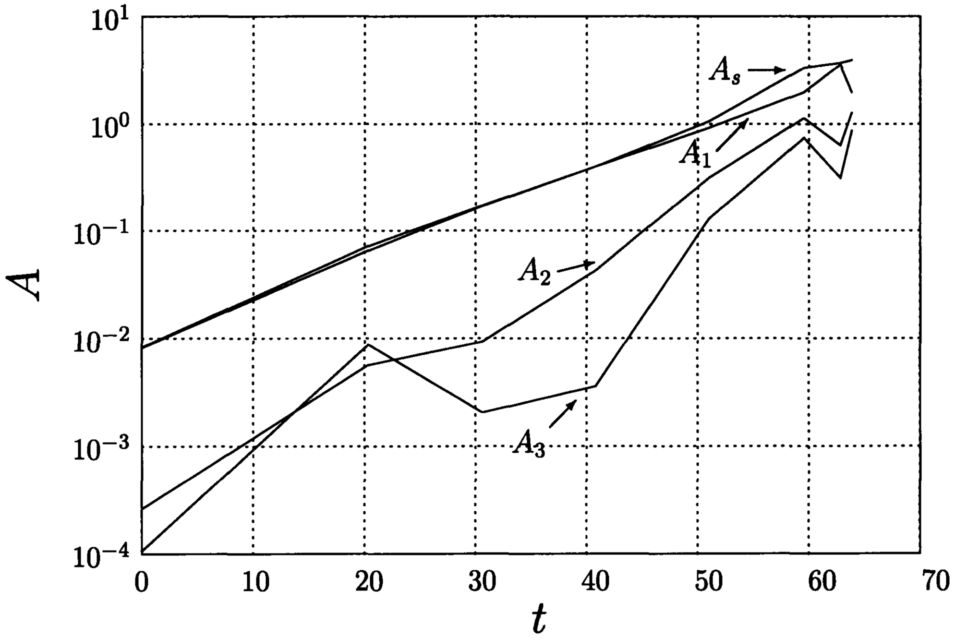

Figure 7-3: Time evolution from the perturbed unstable two-dimensional steady state profile to the three-dimensional stable steady state, for $D = 200$, $Ca = 5$, and $\lambda = 15$, of the meniscus profile amplitude at the mid-plane, $A_s = \left(\max x_s^{3\mathrm{D}} - \min x_s^{3\mathrm{D}}\right)/2$, and of the first three Fourier modes of the profile A_m, associated with $\beta = m\,2\beta_c = m\,\pi/\lambda$ for $m = 1, 2, 3$. (Note the fluctuation near the steady state is due to a remesh from six to seven levels.)

the modes when they achieve finite amplitude, for this particular highly supercritical Ca we obtain great harmonic content in the steady-state. In the steady-state, the $m = 1$ mode is dominant; by this we mean that the amplitude of this mode is greatest compared to the amplitudes of the other modes. This, as will be seen below in Figs. 7-13 and 7-14, is not always the case, it depends on the value of Ca and the history of the flow, to name a few of the determining factors.

As mentioned in Chapter 5, in order to verify the independence of the evolution towards the steady-state with regard to resolution, selected cases were repeated using the final (high) resolution throughout. An example of such a high resolution simulation is shown in Fig. 7-4 which is a repetition of the simulation shown in Fig. 5-5. The ratio of the computational time required to perform the simulation shown in Fig. 7-4 compared to the time to perform the simulation shown in Fig. 5-5 obtained using adaptive spanwise resolution was on the order of 10; the supercomputer (16 nodes of an Intel i860 hypercube) time required for the high resolution simulation was approximately 800 hours compared to approximately 80 hours for the adaptive resolution simulation. It is worthwhile to remember, that without the remeshing techniques presented in Chapter 5 neither simulation could of followed the complete evolution to the steady-state since the mesh distorts greatly near the meniscus. The remeshing was performed on a serial workstation and required on the order of 100 additional hours for both the high and adaptive resolution simulations.

7.2 Properties of the Steady Ribbed State

With the previous results, we confirmed the unstable nature of the two-dimensional steady flow geometry for the supercritical Ca considered, and followed the evolution to the three-dimensional steady ribbed state. We now concentrate on the structure of the stable three-dimensional steady ribbed state in order to observe and quantify the coupling between the meniscus instability and the ribs downstream, and to compute the lengths of the regions identified in Chapter 3.

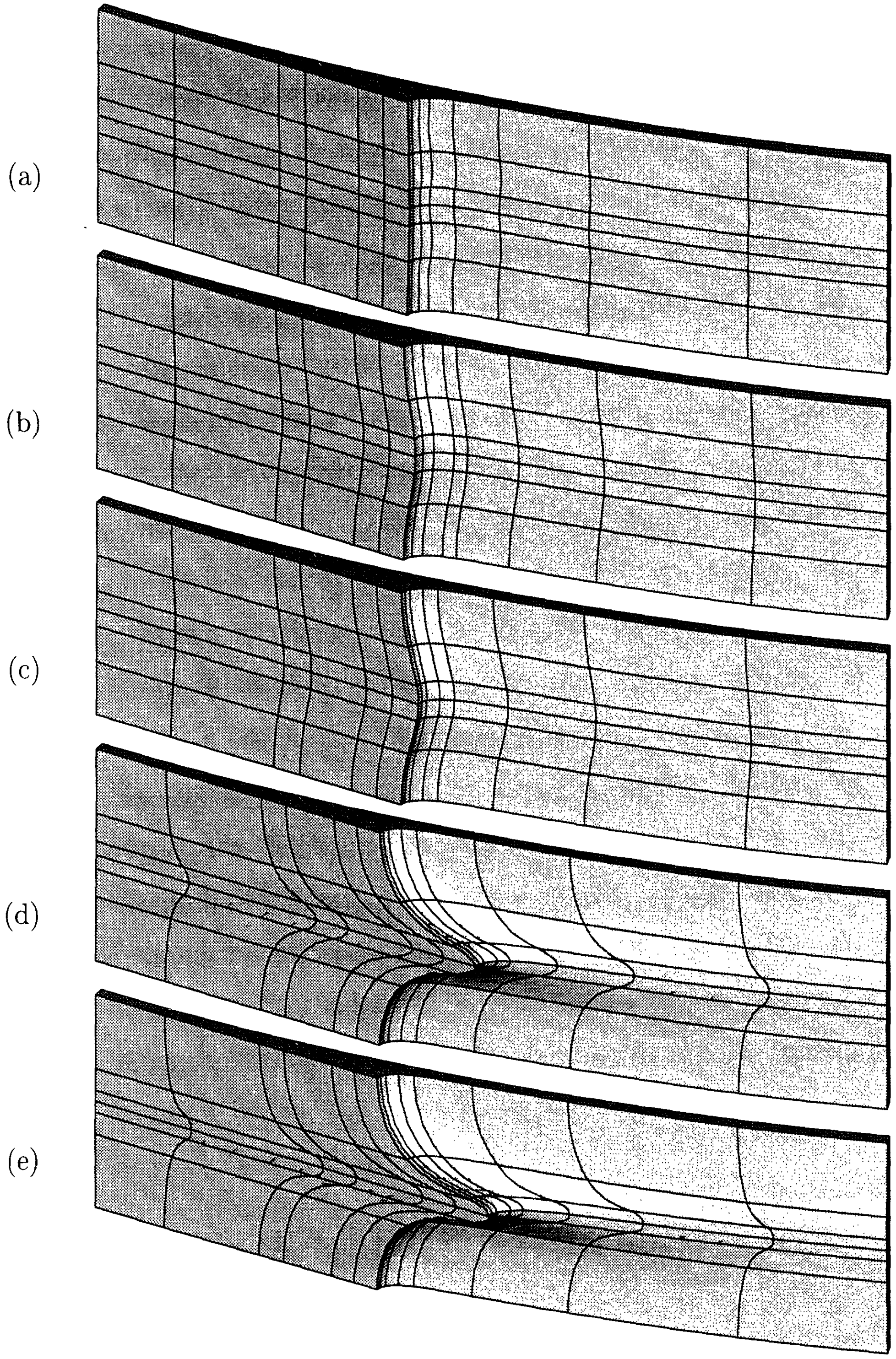

Figure 7-4: Evolution to a steady three-dimensional ribbed-state for $\lambda = 10$, $D = 200$, and $Ca = 3.14$ obtained using "high" resolution throughout the simulation, $\{15, 7, 7\}$. The steady state is identical to the steady ribbed-state shown in Fig. 5-5 obtained using adaptivity in the z direction allowing for lower resolutions during the transients.

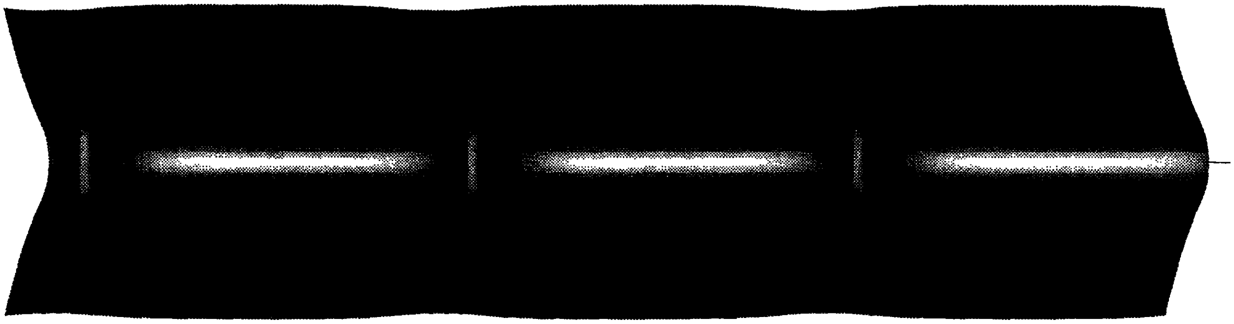

Figure 7-5: View of spanwise periodic stable three-dimensional steady ribbed free-surface geometry for $D = 200$, $Ca = 5$, and $\lambda = 15$.

7.2.1 Meniscus Geometry and Downstream Ribs

In Fig. 7-5 we present a view of the stable three-dimensional free-surface steady-state geometry obtained for the previous set of parameters; to aid visualization, the computational domain Ω of spanwise wavelength $\lambda = 15$ is replicated threefold in z and then reflected along the symmetry plane $\partial\Omega_5$ in order to simulate two rollers. Note the fluid is opaque, thus making only the free-surface visible. The ribs are seen to be very steep, and of very large amplitude in the meniscus region; experimental observations of such steep ribs are commonplace (e.g. Dowson and Taylor[19], Fig. 16).

As described in Chapter 3, the meniscus geometry controls the free surface profile everywhere, and thus we expect to observe ribs downstream from the meniscus. As the view and lighting in Fig. 7-5 do not clearly show the ribs downstream on the rollers, we show in Fig. 7-6 profiles of the steady three-dimensional free-surface at different downstream locations θ. Figure 7-7 shows how the amplitude of the rib, given by $A = (\max f - \min f)/2$, decreases with distance from the nip; note the significant, but localized, effect of the outflow boundary condition on the flow geometry ($A \to 0$ as $\theta \to \theta_{\partial\Omega_3} \cong 22.63°$). The localized outflow effect suggests that other (incorrect) outflow conditions could be used with similar localized results.

7.2.2 Transition of Flow Fields: Helical to Leveling

The decrease in amplitude of the ribs for increasing θ indicates the transformation of the spanwise fluid flow pattern from a rib-sustaining helical flow field to the convergent field of the leveling film. Figure 7-8 shows the dependence of the free-surface spanwise velocity on the downstream position; clearly, between $\theta = 13°$ and $\theta = 15°$ the nature of spanwise velocity profile changes — the spanwise velocity no longer feeds the crest of the rib, but rather, begins to drain fluid from it. This change occurs in what we term the transition region, which is seen to be of a characteristic length $L_t = .75$ for the complete flow field; this estimate for L_t was determined by tracking the max (min) of the free-surface spanwise velocity profile as the fluid moves downstream and performing a least squares fit in the interval $\theta \in [13°, 15°]$. If instead, we concentrate on the length scales associated with the transformation of the flow characteristics of the individual Fourier modes of the spanwise velocity profile, they occur at different approximate locations within the interval $\theta \in [11°, 17°]$. We can extract the length scale associated with each transition by following the amplitude (keeping track of the appropriate sign) of the spanwise velocity mode as it goes through its corresponding transition and by performing a least squares fit on the extracted data. We present the results in Table 7.1; we observe that the quantity L_t is of order 1 and that lower wavenumbers exhibit longer transition lengths, L_{t_m}, than the higher wavenumbers in agreement with our discussion in Chapter 3.

After the transition (of the complete flow-field), the spanwise velocity rapidly converges to the flow profile of a leveling film. This is observed in Fig. 7-9, in which slices of the domain Ω corresponding to the meniscus, transition, and leveling regions show the different flow fields "predicted" by the schematic in Fig. 3-6. Downstream of

L_t	L_{t_1}	L_{t_2}	L_{t_3}	L_{t_4}	L_{t_5}
.75	1.21	1.96	1.27	1.01	1.10

Table 7.1: Transition length, L_t, for the spanwise velocity profile and that of the individual Fourier modes of the spanwise velocity profile, L_{t_m}, of wavenumber $\beta = m\pi/15$ and $m = 1, \ldots, 5$ for $D = 200$, $Ca = 5$, and $\lambda = 15$.

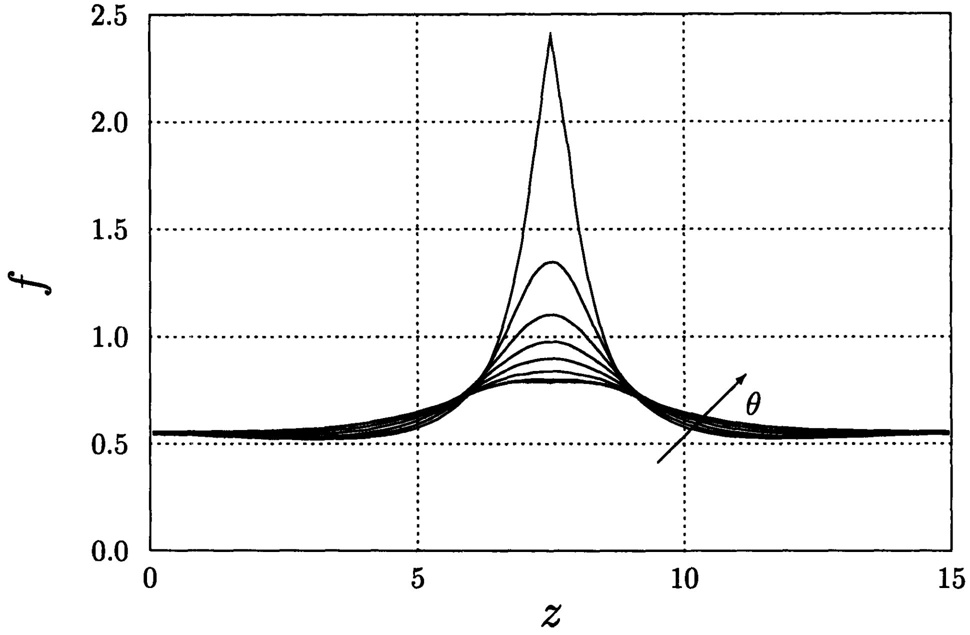

Figure 7-6: Steady free-surface profiles for $D = 200$, $Ca = 5$, and $\lambda = 15$, as a function of downstream position: $\theta = 12°, 13°, 14°, 15°, 16°, 17°, 18°, 19°$. (Note that the sharp profile for $\theta = 12°$ is an artifact of the radial projection.)

$\theta = 15$, in what we called the leveling region, the ribs exhibit a flow that drains fluid from the crest of the rib but, in some cases, the flow near the bottom of the trough still corresponds to a flow that drains fluid from the trough as shown in Fig. 7-9. This is due to the fact that the transition regions for the individual velocity Fourier components ocurr at different downstream locations, and though the flow field no longer sustains the rib, depending on the wavenumber content of the spanwise velocity profile, regions where fluid is drawn from the trough of the rib can be observed downstream of the transition region.

7.2.3 Leveling of Ribs

We now turn to the leveling region and study the leveling of the nonlinear ribs (not monochromatic) as a final measure of confirmation of the behavior described in Chapter 3. The leveling problem to first order is linear, at least for small amplitude ribs, and thus the interaction between wavenumbers can be overlooked. We thus extract

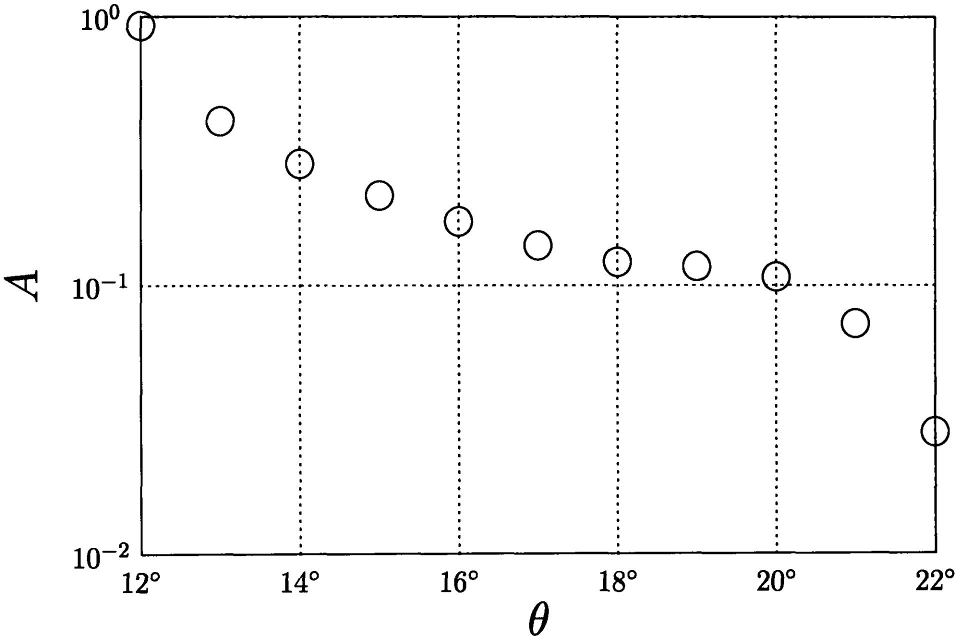

Figure 7-7: Evolution of rib amplitude A (○) for $D = 200$, $Ca = 5$, and $\lambda = 15$, as a function of the roller angle θ. The effect of the outflow boundary condition is clear: $A \to 0$ as $\theta \to \theta_{\partial\Omega_3} \cong 22.63°$.

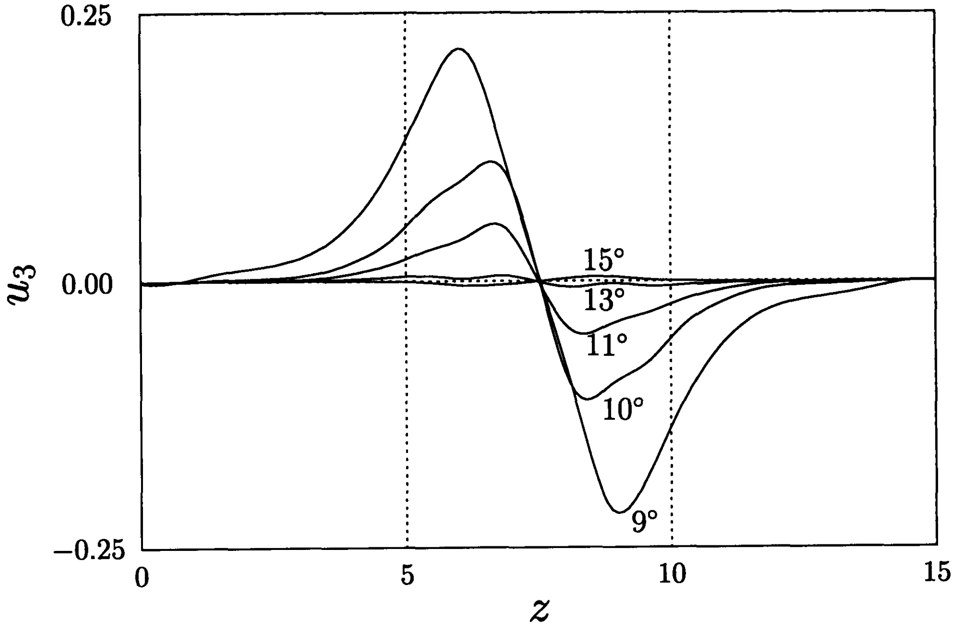

Figure 7-8: Steady free-surface (or on $\partial\Omega_5$) spanwise velocity, u_3, profiles at different downstream positions for $D = 200$, $Ca = 5$, and $\lambda = 15$: $\theta = 9°$, $10°$, $11°$, $13°$, $15°$.

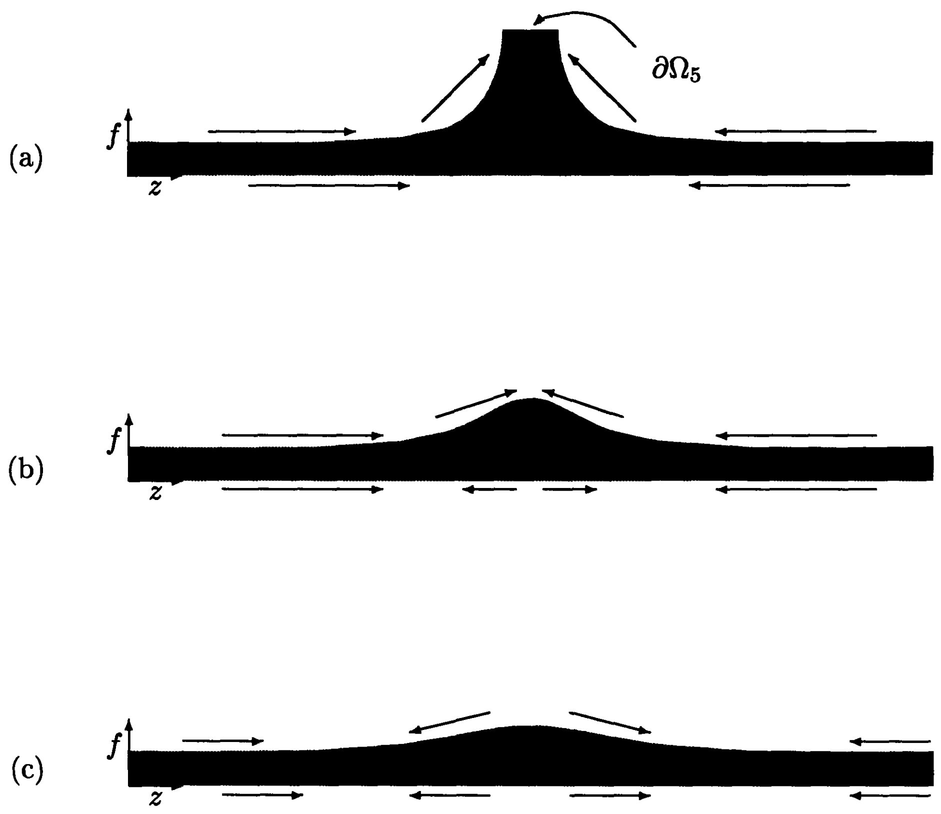
(a)
f
z
$\partial\Omega_5$
(b)
f
z
(c)
f
z

Figure 7-9: Characteristic spanwise velocity, u_3, contours for $D = 200$, $Ca = 5$, and $\lambda = 15$, for: (a) Meniscus region, $\theta = 11°$; (b) Transition region, $\theta = 13°$; (c) Leveling Region, $\theta = 15°$. Legend: Grey $u_3 > 0$; Black $u_3 < 0$; arrows indicate direction of flow.

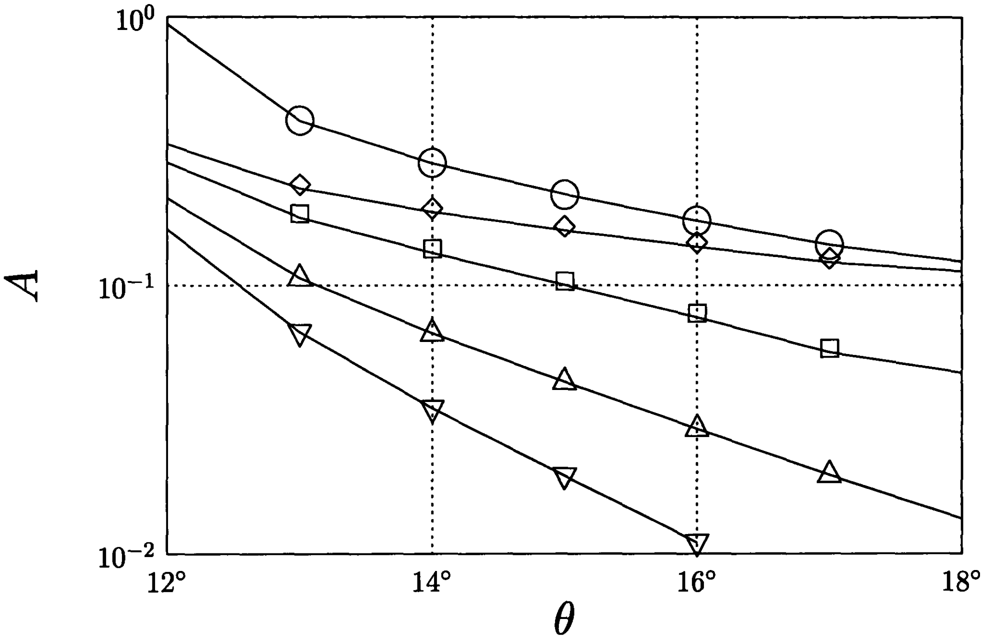

Figure 7-10: Dependence of rib amplitude A (○), and of the amplitude of the profile Fourier modes with wavenumber $\beta_{f_{\rm IV}} = m\,2\pi\,f_{\rm IV}\lambda = m\,2\,f_{\rm IV}\,2\,\beta_c$, $m = 1$ (◇) , 2 (□) , 3 (△) , and 4 (▽) , as a function of roller angle θ for $D = 200$, $Ca = 5$, and $\lambda = 15$.

the wavenumber decay from the sequence of free-surface profiles in Fig. 7-6; this is achieved by performing the Fourier transform of the film profiles, and following the amplitude of each wavenumber individually as the ribs move downstream. Figure 7-10 shows the dependence of the rib amplitude, A, and that of individual wavenumbers, A_m, $m = 1, \ldots, 4$, as a function of the roller angle, θ.

In Fig. 7-10, the absolute value of the slopes are a measure of the distance over which the individual mode amplitudes will persist. As the ribs move downstream, the total rib amplitude asymptotically approaches, from above, that of the lowest wavenumber since, as predicted by the model, higher wavenumbers decay at a faster rate. This is better observed in Fig. 7-11, in which the magnitudes of the individual slopes, L_ℓ, calculated in the leveling region sufficiently upstream of outflow (to avoid intrusive outflow effects), are plotted as a function of the corresponding film wavenumber, $\beta_{f_{\rm IV}} = m\,2\pi\,f_{\rm IV}/\lambda = m\,2\,f_{\rm IV}\,2\,\beta_c$. The results are in good agreement with the prediction of Eq. (3.7). The distance over which the ribs persist, if measured

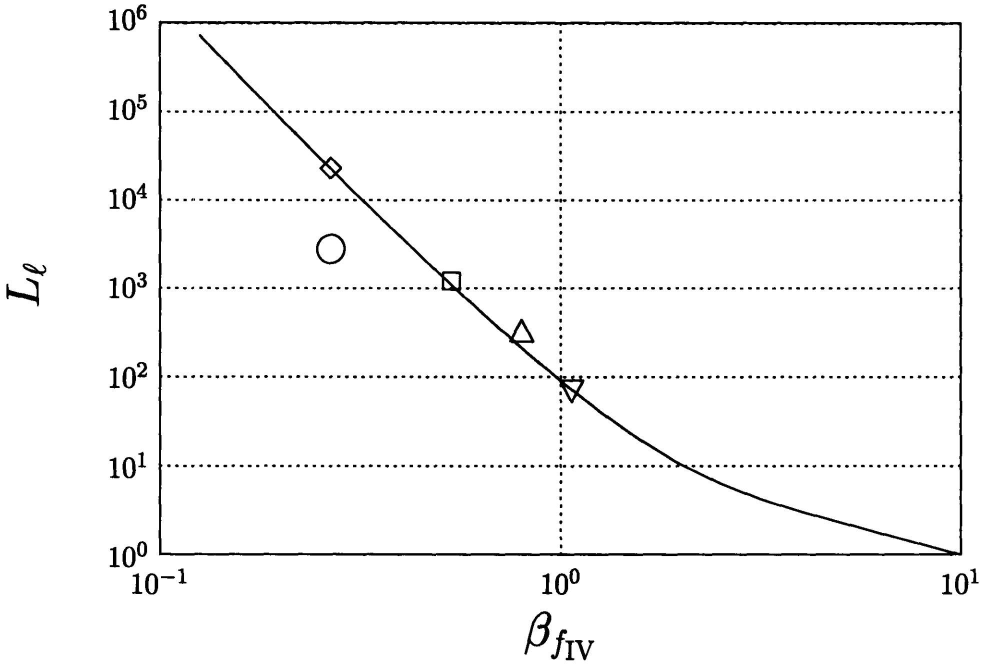

Figure 7-11: Leveling region length, L_ℓ, for the rib, (○), and the first four Fourier modes of the rib profile associated with wavenumbers $\beta_{f_{\rm IV}} = m\,\frac{2\pi f_{\rm IV}}{\lambda} = m\,2\,f_{\rm IV}\,2\,\beta_c$, $m = 1$ (◇) , 2 (□) , 3 (△) , and 4 (▽) for $D = 200$, $Ca = 5$, and $\lambda = 15$.

by considering the decay of the total rib amplitude, is obviously smaller than that of the lowest wavenumber component of the profile since it is the result of a "weighted average" of the individual distances of the wavenumbers that are present. This needs to be taken into account, since using the decay of the total amplitude of the ribs could lead to erroneous results (showing greater decay rates and thus less persisting ribs) if the rib profile were not monochromatic. For correct experimental verification of these predictions, the complete rib profile would have to be determined at different downstream locations, or measurements of the total amplitude would have to be made sufficiently downstream in order for the rib profile to be monochromatic. Hasegawa and Sorimachi[33] report measurements of the amplitudes of ribs assuming a specific rib profile but do not specify the downstream location of the measurement. Without this critical piece of data, comparisons cannot be made with theory nor with our simulation results. The rib amplitude reported by Hasegawa and Sorimachi[33] is a lower bound of the magnitude of the mid-plane rib profile amplitude and can serve as a check (at least as an order of magnitude check) of the amplitude on the rollers. Our numerical results do not contradict the reported experimental results of Hasegawa and Sorimachi[33].

7.3 Steady Ribbed States

The results presented above are all for one combination of the governing parameters, $D = 200$, $Ca = 5$, and $\lambda = 15$. We now illustrate parametric trends by presenting representative results for steady ribbed flow geometries for $Ca = .5, .75, 1, 1.77, 3.16$, and 5, and $\lambda \in (0, \lambda_c]$ (recall that for $D = 200$ $Ca_c = .32$ and $\lambda_c = 30$). Note that when considering $\lambda = \lambda_c$ we are ensured, at least for slightly supercritical Ca, that the most unstable mode (in the linear sense) will have wavenumber $\beta_c = \pi/\lambda_c$ and will be the only mode present in the steady state (due to the lack of non-linear excitation of the higher wavenumber modes). For Ca much greater than Ca_c, the fastest growing mode will have a greater wavenumber than β_c, various wavenumbers will be present in the steady state (since they are linearly unstable or are excited by the mode of wavenumber β_c) and, in addition, the wavenumber of the dominant mode in the steady state (measured by the amplitude of the corresponding Fourier component) will not necessarily correspond to β_c.

As mentioned previously, for most of the results obtained, the average position of $\partial\Omega_4 \bigcap \partial\Omega_5$, $\overline{x}_s^{\mathrm{3D}} = \int_0^\lambda x_s^{\mathrm{3D}} dz/\lambda$, does not differ significantly from the meniscus position for the two-dimensional problem, x_s^{2D}; furthermore, the flowrates through the nip for the two-dimensional and three-dimensional flows differ only slightly, less than 1%. This confirms, that for the range of D, Ca, and λ considered, the total volume flowrate through the nip is not greatly affected by the presence of ribs. The greatest change in flowrate (1%) was observed when the ribs present were of great amplitude, $A_s > 3\,H$, indicating that possibly for even more supercritical Ca, ribs can have an effect on the total flowrate and thus the resulting film thickness.

We first present in Fig. 7-12 results for for $D = 200$ and $\lambda = \lambda_c$ as a function of increasing supercritical Ca. The increase in Ca can be interpreted as an increase in the speed of the rollers maintaining constant fluid properties. As the speed is increased, in addition to the migration of the mean location of the meniscus towards the nip as described in Chapter 6, there is a monotonic increase in rib amplitude. The increase in rib amplitude with greater Ca is observed in all of the domain widths studied. Parallel to the increase in amplitude, there is an increase in harmonic content of the rib profile demonstrated by the steepening of the ribs. A good way of visualizing the harmonic content of the rib profiles is by extracting the amplitudes of the Fourier modes of each profile. Figures 7-13 and 7-14 show the amplitudes of the Fourier modes as a function of their corresponding wavenumber for moderately supercritical and highly supercritical Ca, respectively. The rib profiles for the moderately supercritical Ca are predominantly monochromatic (Fig. 7-13), few Fourier modes have finite amplitude while the profiles for highly supercritical Ca ($Ca \gg Ca_c$) exhibit greater harmonic content (Fig. 7-14), many Fourier modes have finite amplitudes in the steady-state. We observe convergence of the meniscus profiles as Ca is increased to a very steep geometry similar to the convergence observed in the two-dimensional meniscus position shown in Fig. 6-6. This is confirmed in Fig. 7-14 where the difference in harmonic content is mostly in the higher wavenumbers while the two profiles exhibit almost identical low wavenumber content. We suspect that for even greater Ca the profile will not differ much for that of $Ca = 5$ but may exhibit greater overall amplitude as a result of the increase in the high wavenumber modes present in the steady-state. However, we do expect differing characteristics of the steady state geometries as the Ca is increased from criticality for values less than $Ca = 5$. We now present the influence of the domain width on the ribbed geometry for various supercritical Ca.

7.3.1 Moderately Supercritical Steady Ribbed States

We refer to moderately supercritical Ca as those Ca for which the steady state geometries are mostly monochromatic and thus do not exhibit great harmonic content. Figure 7-15 shows, for $D = 200$ and $Ca = .5$, the steady state profiles of $\partial\Omega_4 \bigcap \partial\Omega_5$ as a function of spanwise periodicity $\lambda = \lambda_c/2^{n-1}$ for $n = 1, \ldots, 3$. First, we observe that the high-wavenumber cutoff is less than $4\,\beta_c = \pi\, 4/30$ since the rib amplitude for

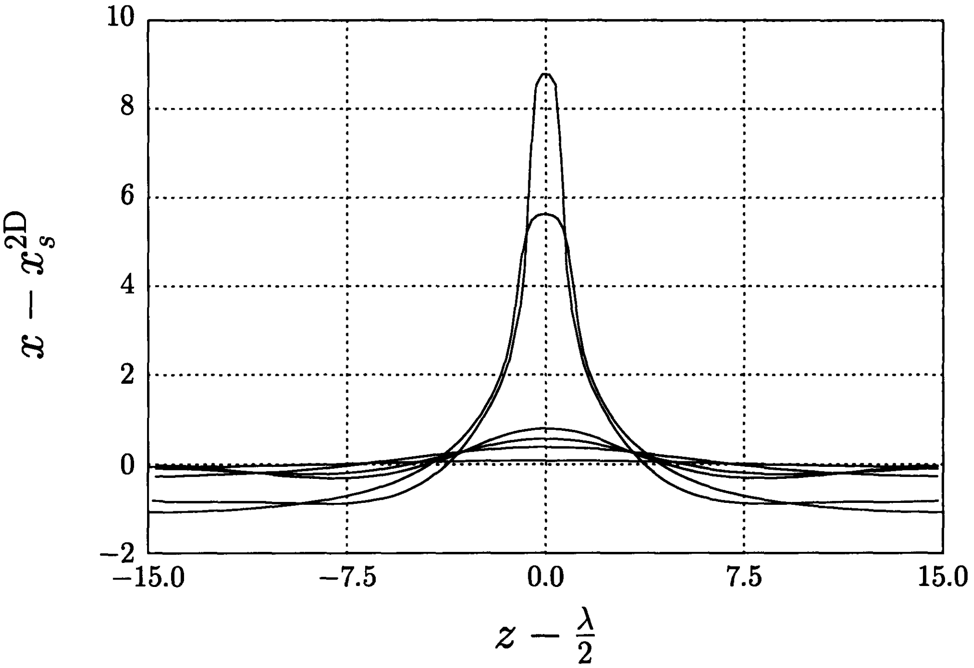

Figure 7-12: Steady state profiles of $\partial\Omega_4 \bigcap \partial\Omega_5$ for $D = 200$, $\lambda = \lambda_c = 30$ and $Ca = .5$, .75, 1, 1.77, 3.16, and 5. The ribs exhibit increasing amplitude, A_s, and harmonic content with increasing Ca (roller velocity).

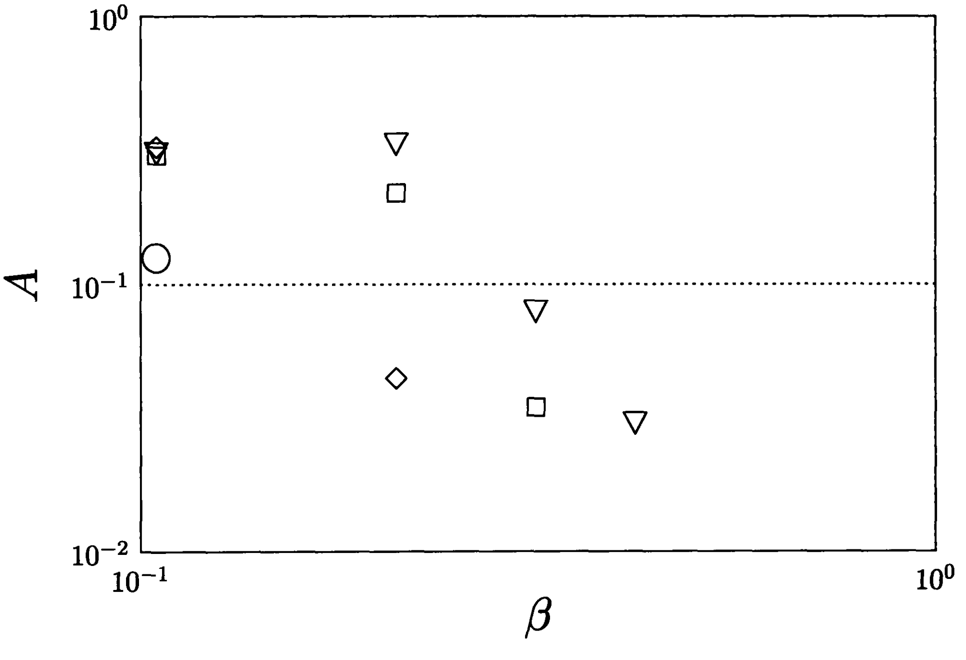

Figure 7-13: Amplitude of the Fourier modes of the steady-state profiles of $\partial\Omega_4 \bigcap \partial\Omega_5$ for $D = 200$, $\lambda = 30$, and $Ca = .5$ (○), .75 (◇), 1 (□), and 1.77 (▽) as a function of the corresponding Fourier mode wavenumber $\beta = m\,\beta_c$.

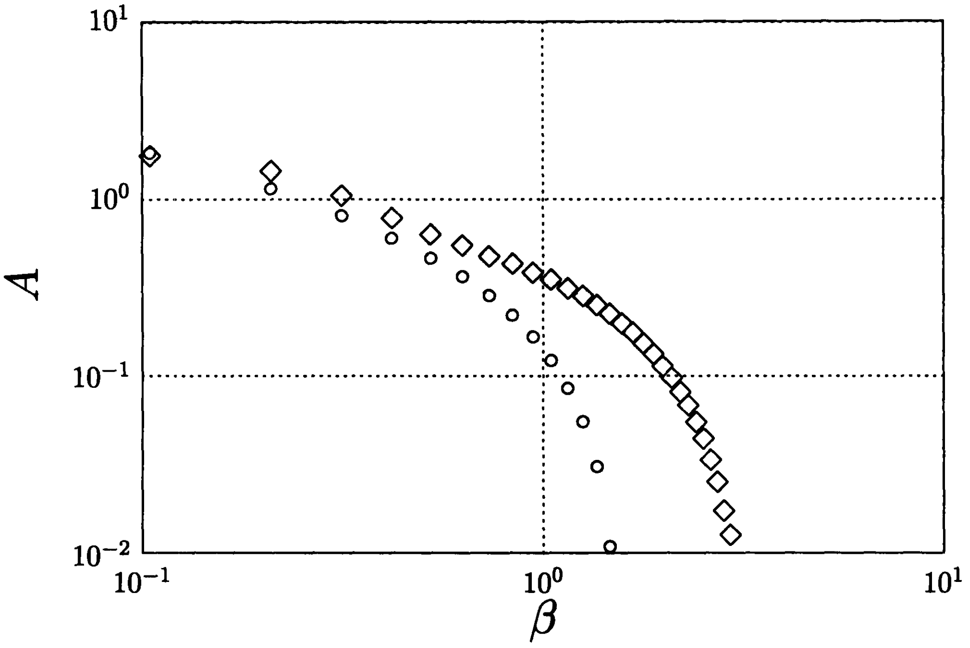

Figure 7-14: Amplitude of the Fourier modes of the steady-state profiles of $\partial\Omega_4 \bigcap \partial\Omega_5$ for $D = 200$, $\lambda = 30$, and $Ca = 3.16$ (○) and 5 (◇) as a function of the corresponding Fourier mode wavenumber $\beta = m\,\beta_c$.

$\lambda = \lambda_c/4$ vanishes. Second, we note that in the interval $\lambda \in (0, \lambda_c]$, there is an increase rib amplitude with increasing λ as is expected since for such a mildly supercritical Ca, β_c should still be the wavenumber of the fastest growing mode over all wavenumbers. To observe the low-wavenumber cutoff, a domain larger than λ_c must be considered. First, a domain with $\lambda = 2\,\lambda_c$ was integrated in time from the perturbed (one-rib of wavelength $\lambda = 2\,\lambda_c$) two-dimensional geometry. Instead of observing a growing disturbance with wavenumber $\beta_c/2$, the amplitude of this disturbance mode decayed and other wavenumbers were observed to grow. As a second attempt to find the steady "one-rib" geometry with $\lambda = 2\,\lambda_c$ the steady ribbed geometry for λ_c was stretched to the right length and integrated in time; again, the "one-rib" geometry disappeared and gave way to several ribs of varying amplitude. Given these "failures", a domain for which $\lambda = 2\,\lambda_c$ was constructed by replicating the (near) steady-state obtained for $\lambda = \lambda_c$ and translating it in the spanwise direction a distance equal to λ_c to obtain a domain with two ribs and a total spanwise dimension of $\lambda = 2\,\lambda_c$ following proce-

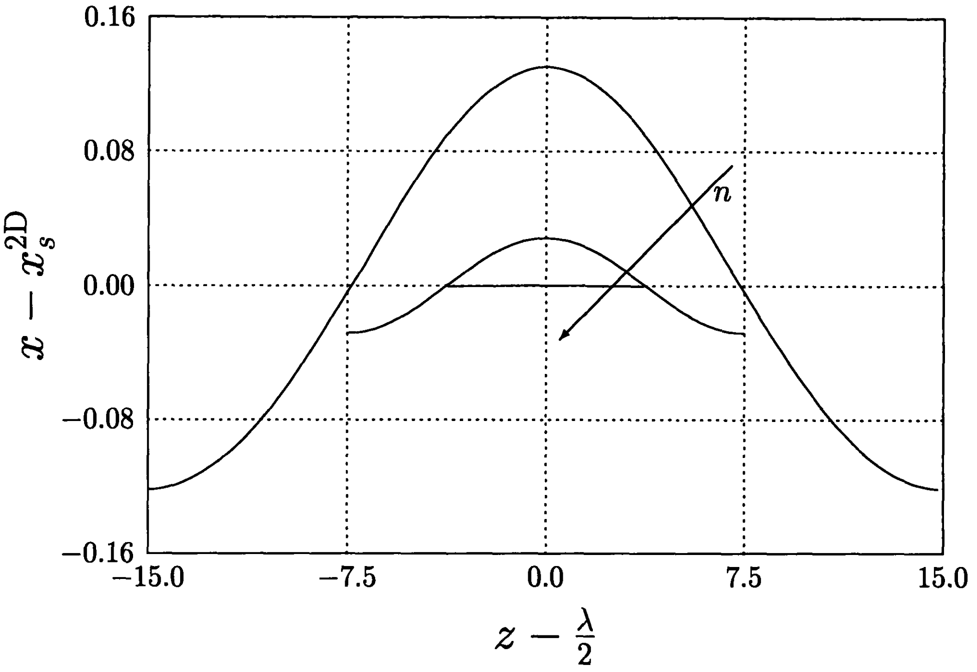

Figure 7-15: Steady state profiles of $\partial\Omega_4 \bigcap \partial\Omega_5$ for $Ca = .5$, $D = 200$, $\lambda = \frac{30}{2^{n-1}}$, and $z \in [0, \lambda]$ for $n = 1, \ldots, 3$.

dures described in Chapter 5. This domain was then integrated in time resulting in negligible changes in the geometry. This new steady-state geometry is presented in Fig. 7-16. The steady state rib profile contains negligible amounts of the wavenumber $\beta = \pi/60$ (present through non-linear interactions) leading us to conclude that the low-wavenumber cutoff for $Ca = .5$ is greater than $\beta = \beta_c/2 = \pi/60$ and that the non-linear interaction of the modes present with the mode of wavenumber $\beta_c/2$ is small. The procedure was repeated, but now instead of starting from the replicated steady-state for $\lambda = \lambda_c$, a state from the evolution to the steady geometry was used to construct the initial condition (shown in Fig. 7-16) and integrated in time. The same "two-rib" steady-state was again obtained.

Similar results to those presented in Fig. 7-15 are shown in Figs. 7-17, 7-18, and 7-19 for $\lambda \in (0, \lambda_c]$ and $Ca = .75$, 1, and 1.77, respectively. In Fig.7-17, that is for $Ca = .75$, we do not observe the monotonic increase of total rib amplitude for increasing λ throughout. This indicates the shifting of the fastest growing wavenumber towards higher values as reported by Coyle et al[14]. The profiles are mostly monochromatic

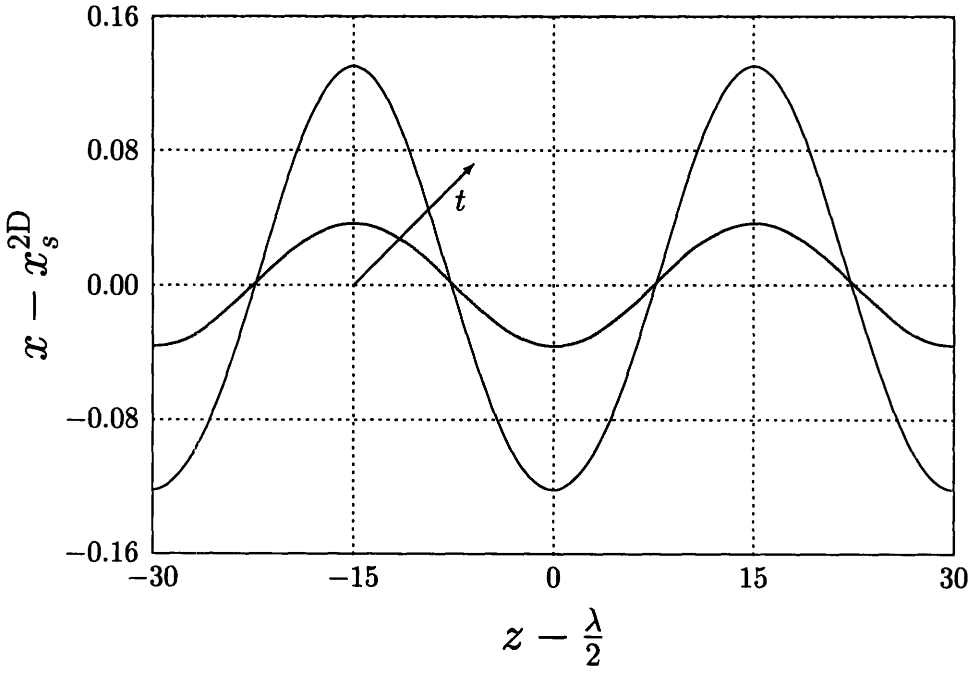

Figure 7-16: Steady state profile of $\partial\Omega_4 \bigcap \partial\Omega_5$ for $D = 200$ and $Ca = .5$ for $\lambda = 2\,\lambda_c = 60$ (solid line) and initial condition based on an intermediate unsteady-state for $\lambda = \lambda_c = 30$ (dashed line). The profile was obtained by replicating the $\lambda = \lambda_c = 30$ geometry and translating it to fit the domain of depth $\lambda = 60$.

and the dominant wavenumber of the steady-state profile still corresponds to $\beta = \pi/\lambda$ (by dominant we mean that the corresponding profile Fourier mode has the greatest amplitude). In Fig. 7-13 we confirm that the steady-state profile for $\lambda = \lambda_c = 30$ and $Ca = .75$ ($\diamond$) is monochromatic consisting of mostly the mode of wavenumber β_c and only slightly of the mode of wavenumber $2\,\beta_c$. There is very little nonlinear interaction between modes and no nonlinear excitation of linearly stable modes by the linearly unstable that have finite amplitude.

If the Ca is increased further, say to $Ca = 1$, the profile corresponding to $\lambda = \lambda_c$ shown in Fig. 7-18, exhibits two crests of differing amplitudes. We conjecture that this phenomena is observed due to the shifting of the fastest growing mode to higher wavenumbers and the lack of nonlinear interaction between the modes. The mode corresponding to β_c is still the dominant mode in the steady-state as observed in Fig. 7-13 ($\square$) but now the amplitude of the modes of wavenumbers β_c and $2\,\beta_c$ are comparable. The mode of wavenumber $3\,\beta_c$ has but a slight contribution to the profile. There are still very few modes present in the profile and all that are present are linearly unstable.

Figure 7-19 shows the steady-state profiles for $Ca = 1.77$. Again we observe two crests of differing amplitudes for the steady-state profile corresponding to $\lambda = \lambda_c$. However, now the mode corresponding to $2\,\beta_c$ is dominant in the steady-state as shown in Fig. 7-13; the amplitude of the mode of wavenumber $2\,\beta_c$ is greater than that of the mode of wavenumber β_c. We observe that there is a little nonlinear excitation of the linearly stable modes since they are present, though in a very small amount in the steady-state profile (in this case we speak of the mode of wavenumber $8\,\beta_c$).

7.3.2 Multiplicity of Steady Ribbed States

In the previous section we observed how difficult (impossible) it was to obtain a one-rib steady-state for $\lambda = 2\,\lambda_c$, $Ca = .5$ and $D = 200$, and the ease with which a two-rib geometry was obtained. The obvious question should arise, is it possible to obtain a two-rib steady-state in a domain (or "box" size) with $\lambda = \lambda_c$? This would

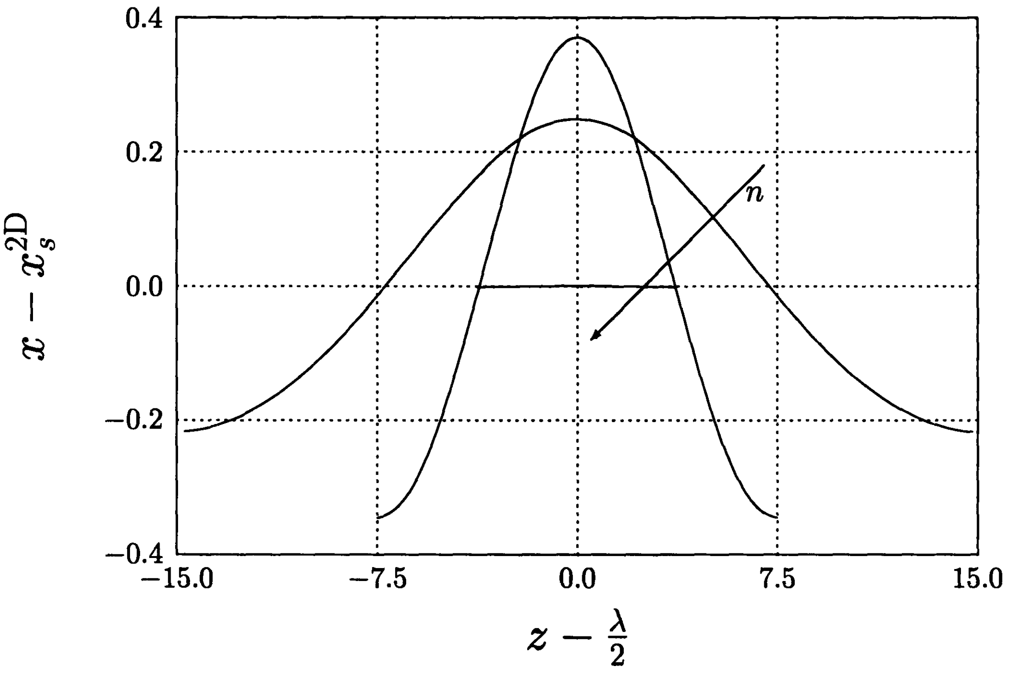

Figure 7-17: Steady-State profiles of $\partial\Omega_4 \bigcap \partial\Omega_5$ for $Ca = .75$, $D = 200$, $\lambda = \frac{30}{2^{n-1}}$, and $z \in [0, \lambda]$ for $n = 1, \dots, 3$.

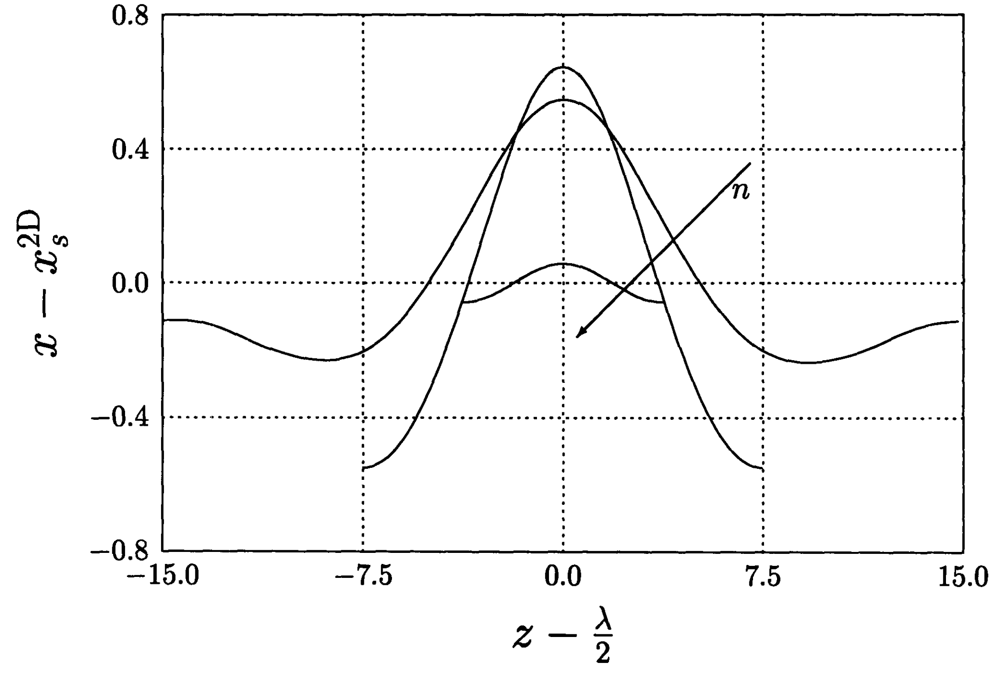

Figure 7-18: Steady-State profiles of $\partial\Omega_4 \bigcap \partial\Omega_5$ for $Ca = 1$, $D = 200$, $\lambda = \frac{30}{2^{n-1}}$, and $z \in [0, \lambda]$ for $n = 1, \dots, 4$.

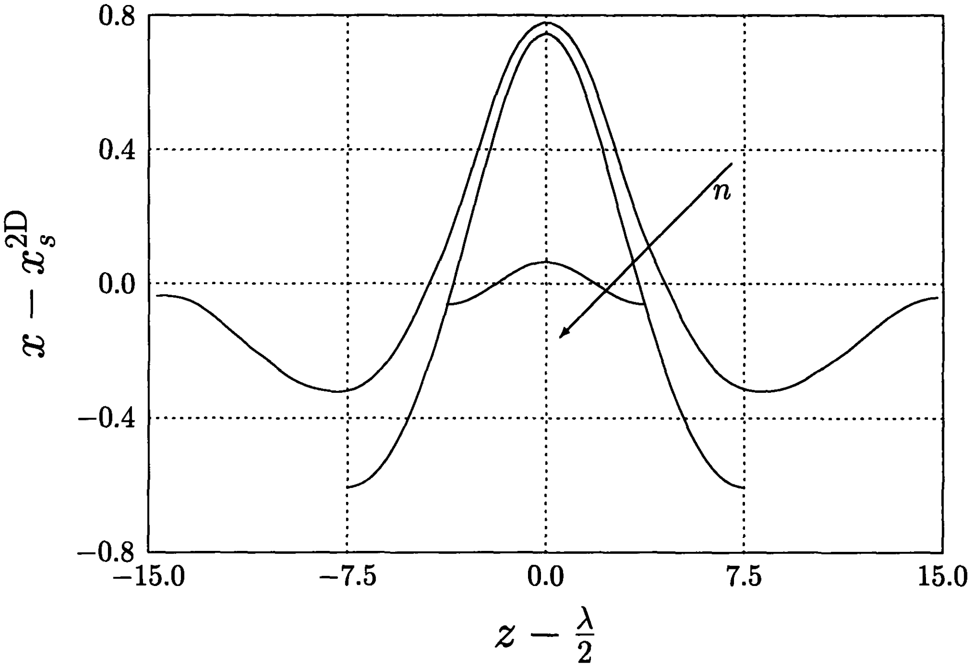

Figure 7-19: Steady-State profiles of $\partial\Omega_4 \bigcap \partial\Omega_5$ for $Ca = 1.77$, $D = 200$, $\lambda = \frac{30}{2^{n-1}}$, and $z \in [0, \lambda]$ for $n = 1, \ldots, 4$.

indicate if multiple steady-states are possible or if the solution we obtain for $\lambda_c/2$, by artificially excluding the wavenumber β_c, suffers from a sub-harmonic instability to the disturbances of wavenumber β_c. We concentrate, mostly due to lack of computational resources, on studying the case mentioned above for $Ca = .5$. Following the same sequence used above to obtain a two-rib steady-state we observed the following:

1. Starting with the two-dimensional (infinitesimally) perturbed steady state, now with a two-rib initial disturbance (each rib of wavelength $\lambda_c/2$), the geometry does not always evolve into a two-rib steady-state (depending on the magnitude of the initial disturbance) but in most cases reaches the one-rib steady-state shown in Fig. 7-15 for $\lambda = \lambda_c$.

2. When a steady ribbed state at a $\lambda \neq \lambda_c$ is stretched (compressed) to construct an initial condition with $\lambda = \lambda_c$ and is integrated in time, the same one-rib steady-state for $\lambda = \lambda_c$ shown in Fig. 7-15 is obtained.

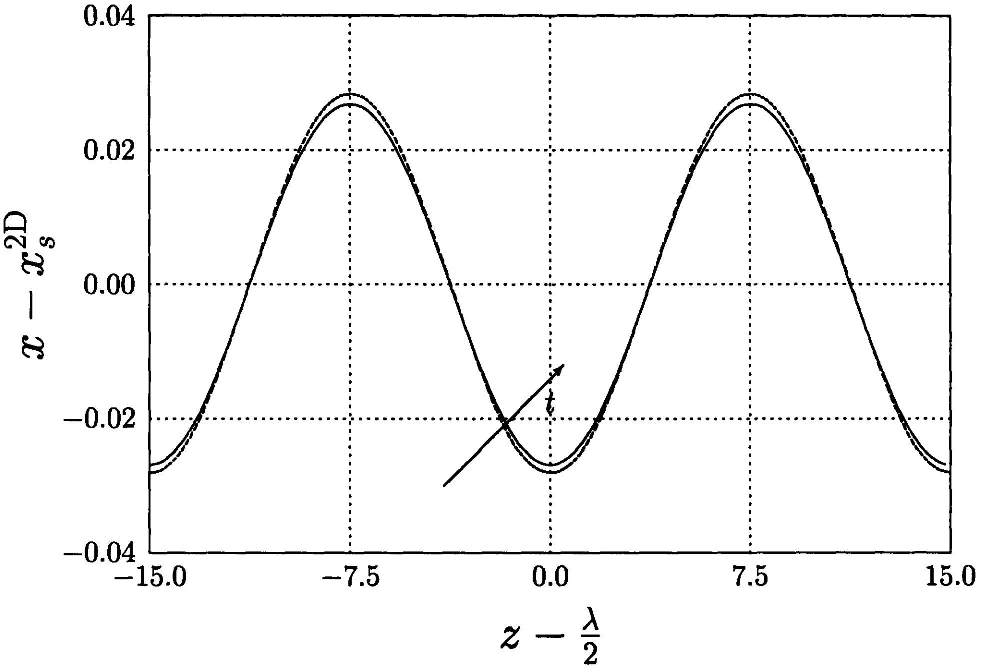

Figure 7-20: Steady state profile of $\partial\Omega_4 \bigcap \partial\Omega_5$ for $D = 200$ and $Ca = .5$ for $\lambda = \lambda_c = 30$ (solid line) and initial condition based on an intermediate unsteady-state for $\lambda = \lambda_c/2 = 15$ (dashed line). The profile was obtained by replicating the $\lambda = \lambda_c = 15$ geometry and translating it to fit the domain of depth $\lambda = 30$.

3. If the steady-state for $\lambda = \lambda_c/2$ is replicated to construct a finite amplitude two-rib initial condition in a "box" of $\lambda = \lambda_c$ and integrated in time, a two-rib steady-state is obtained as shown in Fig. 7-20.

4. If instead, the initial condition is not the exact one-rib steady-state geometry for $\lambda = \lambda_c/2$, but rather, the geometry obtained when the free-surface velocity stopping criterion is satisfied, the same two-rib steady-geometry is obtained as is the case in Fig. 7-20. In fact, a state far from the steady-state, but far from the perturbed two-dimensional geometry, proved to be sufficient.

The previous observations indicate that multiple steady ribbed geometries can be obtained numerically depending on the initial conditions, at least for $Ca = .5$. This would seem to indicate that the history of the flow will have an important effect on the observed ribbed states in physical setups and in addition that it may be possible to observe differing wavelengths of ribs in a long enough (in the spanwise direction) coating apparatus. For more supercritical Ca, multiple steady-states might exist but as we hint below, they should not be observed for highly supercritical Ca.

7.3.3 Highly Supercritical Steady Ribbed States

We refer to highly supercritical steady ribbed states as those that exhibit great harmonic content. The great harmonic content is a consequence of the increase in linearly unstable modes, the nonlinear interaction between modes and of the nonlinear excitation of linearly stable modes by the finite amplitude linearly unstable modes. Figures 7-21, and 7-22 show the steady-state profiles for $Ca = 3.16$ and $Ca = 5$, respectively.

We observe that the steady ribbed profiles are steep; Fig.7-14 shows that the profiles are not monochromatic, many modes of increasing wavenumbers are present in the steady-state, even a great number of modes that are linearly stable ($\beta > \beta_{\mathrm{H}}$). If we investigate the amplitude of the Fourier modes of the profile, we observe that the spectrum is full as shown in Fig. 7-14, with a continuous decay with increasing wavenumber with, again, a dominance of the mode corresponding to β_c and the presence in the steady-state profile of linearly stable modes since we observe finite amplitude Fourier modes with wavenumber greater than the high wavenumber cutoff $\beta_{\mathrm{H}} < 16\,\beta_c$ which we determined from Fig. 7-22. The fact that most modes present have great amplitude is indicative of great nonlinear interaction between modes.

7.3.4 Nonlinear Mode Interaction

For moderately supercritical Ca we observed very little nonlinear interaction between modes and no excitation of linearly stable modes. As the Ca was increased, a shifting towards higher wavenumbers was observed, still with very little nonlinear wavenumber interaction. This resulted in the two crest steady-state profiles that were observed for $\lambda = \lambda_c$ for $Ca = 1$ and $Ca = 1.77$, which consisted mostly of the modes that correspond to β_c and $2\,\beta_c$. For even more supercritical Ca, the nonlinear interaction between modes and the nonlinear excitation of linearly stable modes was clearly observed. We also observed multiple stable steady states for slightly supercritical Ca.

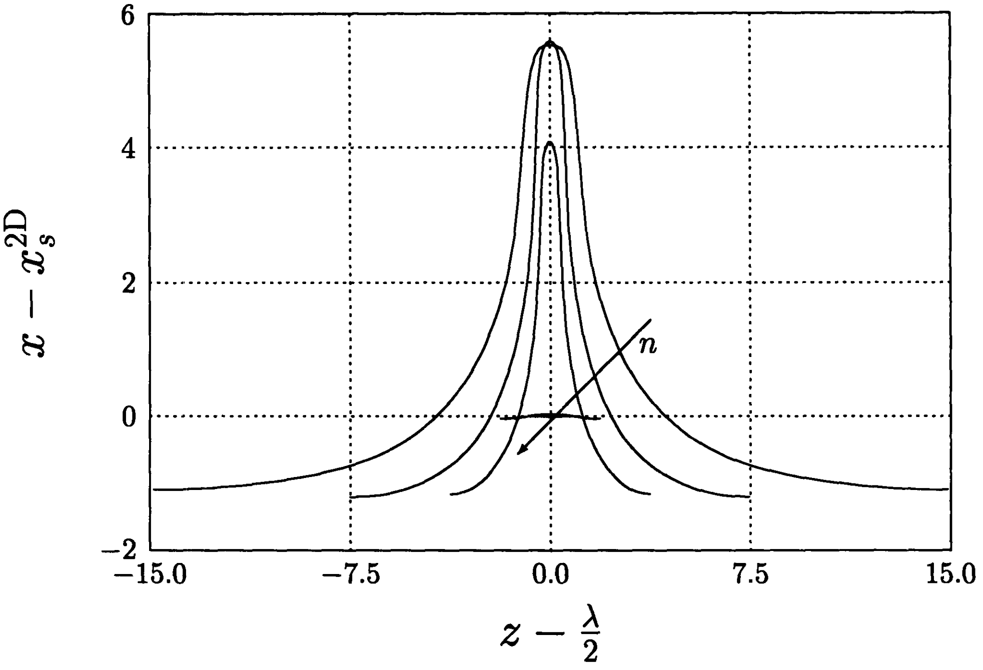

Figure 7-21: Steady-State profiles of $\partial\Omega_4 \bigcap \partial\Omega_5$ for $Ca = 3.16$, $D = 200$, $\lambda = \frac{30}{2^{n-1}}$, and $z \in [0, \lambda]$ for $n = 1, \ldots, 5$.

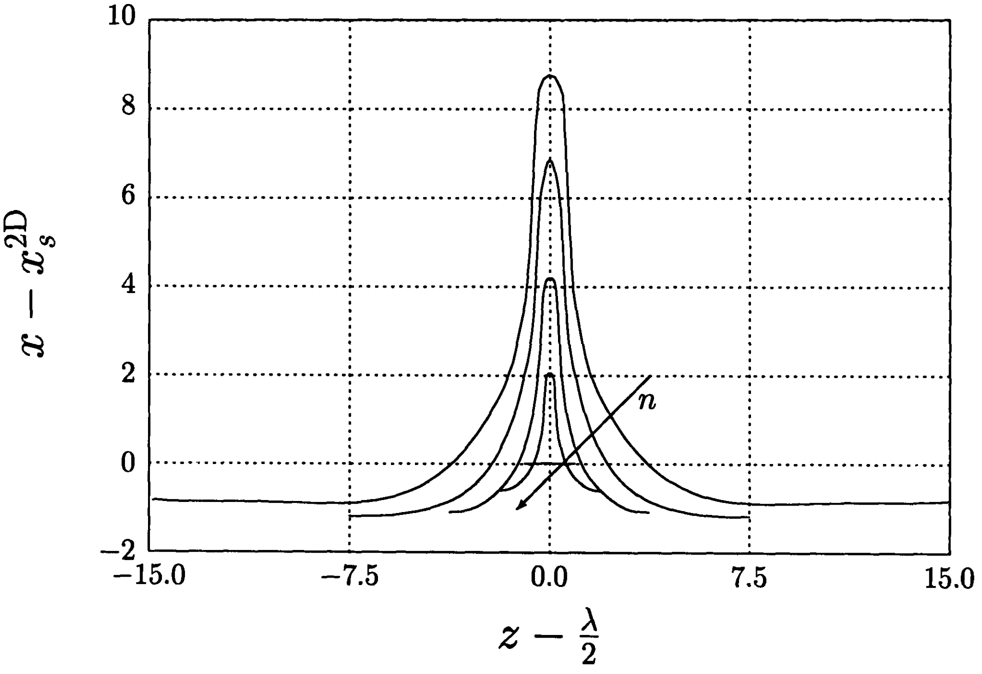

Figure 7-22: Steady-State profiles of $\partial\Omega_4 \bigcap \partial\Omega_5$ for $Ca = 5$, $D = 200$, $\lambda = \frac{30}{2^{n-1}}$, and $z \in [0, \lambda]$ for $n = 1, \ldots, 5$.

We conjecture that there are two competing phenomena that determine the three-dimensional ribbed geometry in the steady-state: the increase in the interval of linearly unstable modes $[\beta_{\mathrm{L}}, \beta_{\mathrm{H}}]$ and the shifting, within this interval, towards higher wavenumber of the fastest growing mode, and the increase of the nonlinear interaction between modes. The phenomena competition results in the following:

1. The rib amplitude for $\lambda = \lambda_c$ will be larger compared to that of smaller λ, for slightly supercritical Ca due to the lack of nonlinear interaction and the fact that the mode with $\beta = \pi/\lambda_c$ is the fastest growing mode.

2. As the Ca is increased, due to the shifting of the fastest growing mode to higher wavenumbers, the almost negligible increase of the interval of unstable wavenumbers, and the lack of nonlinear interaction between modes, we should (and do) observe monochromatic ribs which have a greater amplitude for a $\lambda < \lambda_c$ ($\lambda = \lambda_c/2$ as shown in Figs.7-18 and 7-19).

3. For sufficiently supercritical Ca, nonlinear mode interaction (and nonlinear excitation of linearly stable wavenumbers) should become important. The rib profiles should exhibit great harmonic content due to the excitation of the linearly stable modes. The nonlinear mode interaction should also begin to exhibit "back-scatter", excitation of lower wavenumber modes by high wavenumber modes, for sufficiently great Ca.

4. With sufficient nonlinear interaction between modes, more precisely due to the increase of cross-excitation between high and low-wavenumber modes, the total rib amplitude for $\lambda = \lambda_c$ should again be greater than that of ribs of $\lambda < \lambda_c$. The nonlinear interaction should overcome the shifting of the most unstable wavenumber. The above mentioned crossover is observed for $Ca = 3.16$ in Fig. 7-21, for which the rib amplitude for $\lambda = \lambda_c/2 = 15$ is almost equal to that of $\lambda = \lambda_c = 30$.

5. The crossover is confirmed in Fig. 7-22 which shows that the amplitude for $\lambda = \lambda_c = 30$ is again greater than that the amplitude for $\lambda < 30$.

6. For Ca beyond the crossover, we believe that the ribs for λ slightly larger than λ_c should be of greater amplitude and steeper than those observed in Fig. 7-22 due to the high harmonic content and nonlinear interaction between modes.

7. We observed that the steady state for $Ca = .5$ and $\lambda_c/2$ was stable and does not exhibit a sub-harmonic instability (to disturbances of wavenumber β_c). We believe that this is due to the limited non-linear interaction between the different modes. This indicates that for slightly supercritical Ca, multiple steady-states can be attained. On the other hand highly supercritical Ca, should not exhibit multiple steady states due to the great nonlinear interaction between modes. The nonlinear interaction should give rise to sub-harmonic instabilities, thus only allowing for one possible steady state.

8. The mode corresponding to $\beta = \beta_c/2$ is linearly stable for moderately supercritical Ca. This mode will eventually become unstable for sufficiently large Ca. Before this Ca is reached we believe that through nonlinear excitation from the mode of wavenumber $\beta = \beta_c$, the mode of $\beta = \beta_c/2$ will be present in the steady-state geometry similar to what occurs to the linearly stable high wavenumber modes that exhibit finite amplitudes in the steady states.

7.3.5 The Limit $\lambda \to \infty$ and End Effects

We have observed differing steady-state geometries as a function of the Ca, the spanwise periodicity λ, and the number of ribs present in this "box". We have artificially filtered low-wavenumber modes and not included end effects by imposing (numerically) a spanwise periodicity λ. When we considered a spanwise periodicity greater than λ_c, say $\lambda = 2\,\lambda_c$, we observed the effects of the low wavenumber cutoff predicted by linear-stability. We attempt in this section to answer the following questions: what wavelength of ribbing is observed in a real coating apparatus? and what, if any, role does finite roll length play in the wavelength selection process?

For slightly supercritical Ca, more specifically $Ca = .5$, we have shown the existence of multiple stable steady-states, though in order to find the lower-wavelength state, we required a non-physical procedure (non-inclusion of low-wavenumbers in order to initialize the flow field). This leads us to hazard that two (or possibly more) types of flow geometries could be observed in the steady-state:

1. Starting from a rib free flow field, that is $Ca < Ca_c$, if the speed of the rollers is increased gradually, we should observe the onset of ribbing with the critical wavenumber β_c and should result in ribs of wavelength λ_c (that is for an infinitely long roller pair). Since the increase in the speed of the rollers is only gradual, the geometries observed should resemble those observed in the main bifurcation for $\lambda = \lambda_c$. If the end of the rollers serve as barriers to the spanwise flow, that is, flow cannot flow off the rollers, the flow will try to accommodate an integer number of ribs (the ribs near the roller ends will be slightly distorted as reported by Coyle et al[14]). This will force a rib wavelength near λ_c but not necessarily equal to λ_c. End effects thus play a secondary role in this case.

2. If on the other hand, the increase of the speed of the rollers (Ca) is performed drastically, the resulting initial condition will be sufficiently different from the steady-state and enough disturbances will be present in the flow, that the smaller wavelength steady-states (what we termed two-rib) could be observed, at least over some of the extent of the rollers. In addition, the lower wavelength is already observed for $Ca = 1$ and 1.77 since the ribbed states for this set of parameters exhibits two-crests of differing amplitude.

3. If the speed of the rollers is decreased slowly from a value that exhibits a ribbed flow field (but only slightly supercritical), to another supercritical Ca, the wavelength should not change dramatically if the rollers have end-stops. If on the other hand fluid is not restricted from flowing in the spanwise direction, the wavelength should increase slowly following the increase in the fastest growing wavelength with decreasing Ca determined from linear stability analysis.

4. The local stability of the steady-state flow geometries lead us to believe that the different family of solutions can be accurately tracked. This indicates that if a

two-rib geometry is obtained and the speed of the rollers is decreased gradually, the two-rib geometry should still be observed (if the corresponding mode is still linearly unstable).

We conjecture that when considering domains of great extent, $\lambda \gg \lambda_c$, depending on the history of the flow geometry, multiple steady states can be observed, not necessarily occupying the complete domain, but possibly coexisting side by side. This should possible since the differences between the flow fields and the free-surface geometries are not great. The length of the rollers will play a weak role in determining the overall wavelength of the ribbing, decreasing in importance with increasing length of the rollers.

7.3.6 Transition Region and Leveling of Ribs: Revisited

The transition region length was determined for some of the ribbed geometries presented above and was observed to be of order one with similar wavenumber dependence to that observed in Table 7.1.

Following procedures similar to those used to construct Fig. 7-10, we collect in Fig. 7-23 the quantity $L_\ell / (Ca\, f_{\mathrm{IV}})$ for some of the ribbed geometries obtained. The quantity $L_\ell / (Ca\, f_{\mathrm{IV}})$ should now only be a function of Fourier mode film wavenumber $\beta_{f_{\mathrm{IV}}} = 2\pi\, f_{\mathrm{IV}}\, m/\lambda$, as confirmed in Fig. 7-23. We note that there is very good agreement with the predictions of Eq. 3.7, save at very low wavenumbers. We conjecture, but do not yet have conclusive evidence, that the latter is due to either poor signal to noise ratio (since the decay rates are very small) or outflow effects.

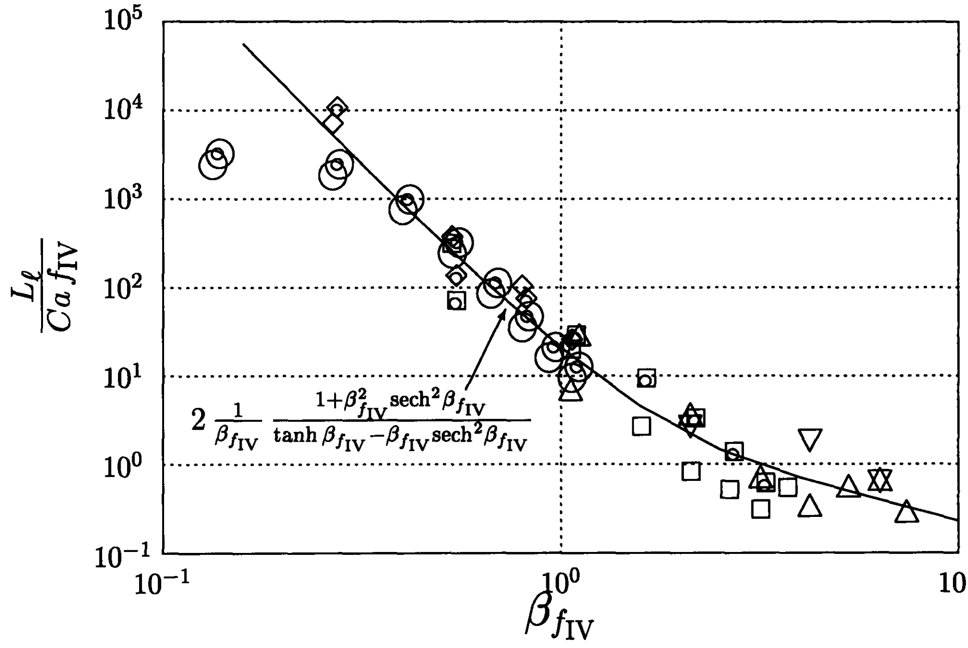

Figure 7-23: Leveling region length, L_ℓ, of the Fourier modes of the rib profile as a function of spanwise wavenumber, $\beta_{f_{IV}} = \frac{2\pi f_{IV}}{\lambda} m$, for $D = 200$, $\lambda = 30/2^{n-1}$, and capillary number $Ca = 1$, $n = 1$ (◎), 2 (◈), 3 (▣), 4 (◬), and $Ca = 5$, $n = 1$ (○), 2 (◇), 3 (□), 4 (△), 5 (▽).

Chapter 8

Conclusions

We have proposed a framework for understanding the formation, evolution, and spatial persistence of ribbing in symmetric forward roll coating, and have presented companion justificatory, quantifying parallel spectral element simulations of the full unsteady three-dimensional nonlinear free-surface fluid flow problem. The simulations corroborate all aspects of the proposed model, both as regard qualitative structure (the meniscus, transition, leveling, and leveled regions), and quantitative measures (initial growth given by γ, approach to the steady state, transition region length L_t and the length scale associated with leveling L_ℓ).

The relationship between downstream rib amplitude and the flow parameters is complex. As Ca increases, the meniscus region rib amplitude and harmonic content increase. For mildly supercritical Ca, the meniscus rib profiles (and thus the downstream rib profiles) are monochromatic while the ribs for highly supercritical Ca exhibit great harmonic content. In addition, linear stability results indicate that the dangerous wavenumber range, $[\beta_{\mathrm{L}}(Ca), \beta_{\mathrm{H}}(Ca)]$, grows to include higher wavenumbers — in particular, the wavenumber for the fastest growing mode shifts to greater values.

We have seen that rib persistence, L_ℓ, is an increasing function of Ca but a decreasing function of β. It is possible (e.g. for particular roller separations, D) that certain supercritical — high-velocity — operating conditions will yield viable product, that is, coatings with no significant ribbing on the downstream webs. Proper understanding of the instability-leveling competition, and of the process of wavelength selection, could suggest such operating conditions. For example, we observed that for moderately supercritical Ca ($Ca \sim 1$), the dominant wavenumber of the steady state profile did not correspond to β_c but rather to $2\,\beta_c$. In addition, we presented results of states for which linearly unstable low wavenumber modes are not present in the steady state. Selecting such operating conditions would result in ribs that persist less (faster decay as the ribs move downstream), say, than a slightly lower Ca for which the wavenumber content of the rib profile exhibited dominance of lower wavenumbers. Such operating conditions would be useful when a tolerance on the amplitude of the ribs on the downstream webs is specified at a given downstream location since the amplitude of the downstream ribs at a particular downstream location is a function of Ca, the wavenumber content of the ribs, and the amplitude of the ribs in the meniscus region.

Finally, the coupling of meniscus instability with the downstream appearance of ribs also suggests various near-meniscus strategies, such as the nylon-string prophylactic of Hasegawa and Sorimachi[33] or any other *knife* or blade coating equivalent[52].

8.1 Guidelines for Future Work

Future work should address certain shortcomings of our computational methods such as:

1. The explicit free-surface update, in order to decrease computational costs. Implicit methods for the treatment of the kinematic condition could be considered. Mixed methods such as extensions to three-dimensions of the two-dimensional methods used could provide for an increase in time-step size without a great increase in problem size.

2. The overly intrusive outflow boundary condition, in order to be able to more precisely quantify leveling.

3. The restrictive remeshing procedures, in order to study the evolution from one three-dimensional steady-state to another during which the meniscus geometry deforms even more. We observed during some of the transients re-entrant geometries for which our remeshing techniques failed. Elliptical domain decomposition techniques[67, 9, 7], could allow for automatic remeshing of re-entrant geometries. The use of such techniques would also require efficient algorithms for the mapping of the old field quantities onto the new mesh.

From the physical standpoint, several unresolved issues stand out:

1. We have shown that experimental measurements such as those performed by Hasegawa and Sorimachi[33] are, perforce, inaccurate since they assume a specific rib profile. In addition, when such measurements are reported, the downstream location of where the profile was measured must be included since without this information the data is almost useless.

2. We showed that history effects are important as is the case for nonlinear systems that can exhibit hysteresis [44]. A more thorough investigation of the nonlinear evolution between three-dimensional ribbed states and better understanding of the process of wavenumber selection in finite spanwise domains, say several multiples of λ_c[3], could provide insight into the selection of useful operation conditions that could otherwise not be observed.

3. The influence of non-Newtonian effects on the meniscus instability coupled with rib leveling.

4. The determination of the necessary conditions for the appearance of re-entrant ribs in symmetric forward-roll coating. We suggest in Chapter 5 that re-entrant ribs might arise without non-Newtonian effects even in the range of Ca that we consider, but due to the limitations of our remeshing procedures we could no determine if this is the case. In addition, the physics of the growth of the reentrant ribs could be too slow for our stopping criterion and thus this, too, might need revision. Re-entrant ribs are readily observed for other coating techniques[27]

thus their study in forward-roll coating might benefit from knowledge gathered in other geometries. Re-entrant geometries are characteristic of other types of defects observed in higher speed coating procedures.

Bibliography

[1] K. Adachi, T. Tamura, and R. Nakamura, *Coating flows in a nip region and various critical phenomena*, AIChE J., 34 (1988), pp. 456–464.

[2] K. Bathe, *Finite Element Procedures in Engineering Analysis*, Prentice-Hall, Englewood Cliffs, NJ, 1982.

[3] M. Bennet, K. Tsiveriotis, and R. Brown, *Nonlinear dynamics in periodically repeated sets of directional solidification cells*, Phys. Rev. B, 45 (1992), pp. 9562–75.

[4] E. L. Canedo and C. D. Denson, *Flow in driven cavities with a free surface*, AIChE J., 35 (1989), pp. 129–38.

[5] C. Canuto, M. Hussaini, A. Quaternoni, and T. Zang, *Spectral Methods in Fluid Dynamics*, Springer-Verlag, 1988.

[6] K. Christodolou, *Computational Physics of Slide Coating Flow*, PhD thesis, Dept. of Chemical Engineering and Materials Science, Univ. of Minnesota, 1989.

[7] K. Christodolou and L. Scriven, J. Sci. Comput., 355 (1988).

[8] ——, *The fluid mechanics of slide coating*, J. Fluid Mech., 208 (1989).

[9] ——, *Discretization of free surface flows and other moving boundary problems*, J. Comput. Phys., 99 (1992).

[10] E. Cohen and G. E.B., *Modern Coating and Drying Technology*, VCH Publishers, New York, 1992.

[11] D. Coyle, *Roll coating*, in Modern Coating and Drying Technology, E. D. Cohen and E. B. Gutoff, eds., VCH Publishers, N.Y.,N.Y., 1992, ch. 3, pp. 63–115.

[12] D. Coyle, C. Macosko, and L. Scriven, *Film splitting flows in forward roll coating*, J. Fluid Mech., 171 (1986).

[13] ——, *The fluid dynamics of reverse roll coating*, AIChE J., 36 (1990).

[14] ——, *Stability of symmetric film-splitting between counter-rotating cylinders*, J. Fluid Mech., 216 (1990).

[15] J. Coyne and H. Elrod, J. Lub. Tech., 92 (1970), p. 451.

[16] ——, A.S.M.E., (1971).

[17] P. de Gennes, X. Hua, and P. Levinson, *Dynamics of wetting: local contact angles*, J. Fluid Mech., 212 (1990), pp. 55–63.

[18] J. Donea, *Arbitrary lagrangian-eulerian finite element methods*, in Computational Methods for Transient Analysis, T. Belytschko and T. Hughes, eds., North Holland, 1983, ch. 10.

[19] D. Dowson and C. Taylor, *Cavitation in bearings*, Ann. Rev. Fluid Mech., 11 (1979), pp. 35–66.

[20] P. Drazin and W. Reid, *Hydrodynamic stability*, Cambridge University Press, 1981.

[21] E. Dussan, *On the spreading of liquids on solid surfaces: static and dynamic contact lines*, Ann. Rev. Fluid Mech., 11 (1979), pp. 371–400.

[22] E. Dussan V., *The moving contact line: the slip boundary condition*, J. Fluid Mech., 77 (1976), pp. 665–84.

[23] E. Dussan V. and S. Davis, *Stability in systems with moving contact lines*, J. Fluid Mech., 173 (1986), pp. 115–30.

[24] E. Dussan V., E. Rame, and S. Garoff, *On identifying the appropriate boundary conditions at a moving contact line: and experimental investigation*, J. Fluid Mech., 230 (1991).

[25] P. Fischer, *Spectral Element Solution of the Navier-Stokes Equations on High Performance Distibuted-Memory Parallel Processors*, PhD thesis, Massachusetts Institute of Technology, 1989.

[26] P. F. Fischer and A. T. Patera, *Parallel simulation of viscous incompressible flows*, Ann. Rev. Fluid Mech., 26 (1994), pp. 483–527.

[27] L. Fourtune, W.-J. Rappel, and M. Rabaud, *Phase dynamics near a parity-breaking instability*, Phys. Rev. E, 49 (1994).

[28] V. Gokhale, *Improved stability criterion for lubrication flow between counter-rotating rollers*, AIChE J., 29 (1983), pp. 865–6.

[29] H. Greenspan, *On the motion of a small viscous droplet that wets a surface*, J. Fluid Mech., 84 (1978), pp. 125–43.

[30] E. Gutoff and C. Kendrick, *Dynamic contact angles*, AIChE J., 28 (1982), pp. 459–66.

[31] E. B. Gutoff, *Avoid coating and drying defects*, Chem. Eng. Prog., (1993).

[32] V. Hakim, M. Rabaud, H. Thomé, and Y. Couder, *Directional growth in viscous fingering*, in New Trends in Nonlinear Dynamics and Pattern-Forming Phenomena, C. P. and P. Huerre, eds., vol. 237 of B, Plenum-Press, 1990.

[33] T. Hasegawa and K. Sorimachi, *Wavelength and depth of ribbing in roll coating and its elimination*, AIChE J., 39 (1993).

[34] B. Higgins and L. Scriven, *Capillary pressure and viscous pressure drop set bounds on coating bead operability*, Chem. Eng. Sci., 35 (1980), pp. 673–682.

[35] L. Ho, *A Legendre spectral element method for simulation of incompressible unsteady viscous free surface flows*, PhD thesis, Massachusetts Institute of Technology, 1989.

[36] L.-W. Ho and A. T. Patera, *A legendre spectral element method for simulation of unsteady incompressible viscous free-surface flows*, Comput. Meth. Appl. Mech. Eng., 80 (1990).

[37] ——, *Variational formulation of three dimensional viscous free-surface flows: Natural imposition of surface tension boundary conditions*, Int. J. Num. Meth. Fluids, 13 (1991).

[38] L.-W. Ho and E. Rønquist, *Spectral element solution of steady incompressible viscous free-surface flows*, in Proceedings of the international conference on spectral and high order methods for partial differential equations, Le Corum, Montpellier, France, 1992, North-Holland.

[39] L. Hocking, *Rival contact-angle models and the spreading of drops*, J. Fluid Mech., 239 (1992), pp. 671–681.

[40] K. Ishimi, H. Hikita, and M. Esmail, *Dynamic contact angles on moving plates*, AIChE, 32 (1986), pp. 486–92.

[41] H. S. Kheshgi, *Profile equations for film flows at moderate reynolds numbers*, AIChE J., 35 (1989), pp. 1719–27.

[42] S. Kistler and L. Scriven, *Coating flows*, in Computational Analysis of Polymers, J. Pearson and S. Richardson, eds., Barking, Essex,England, 1983, ch. 8, pp. 243–299.

[43] ——, *Coating flow theory by finite element and asymtotic analysis of the navier-stokes system*, Int. J. Num. Meth. Fluids, 4 (1984).

[44] ——, *The teapot effect: sheet-forming flows with deflection, wetting and hysteresis*, J. Fluid Mech., 263 (1994).

[45] K.-Y. LEE, L.-D. LIU, AND T.-J. LIU, *Minimum wet thickness in extrusion slot coating*, Chem. Eng. Sci., 47 (1992).

[46] B. LEVICH, *Physicochemical Hydrodynamics*, Prentice Hall, Englewood Cliffs, N.J., 1962.

[47] C. MILL AND G. SOUTH, *Formation of ribs on rotating rollers*, J. Fluid Mech., 28 (1967).

[48] S. ORCHARD, *On surface leveling in viscous liquids and gels*, App.Sci.Res., 11 (1962), pp. 451–464.

[49] A. T. PATERA, *A spectral element method for fluid dynamics: Laminar flow in a channel expansion*, J. Comput. Phys., 54 (1984), pp. 468–488.

[50] J. PEARSON, *The instability of uniform viscous flow under rollers and spreaders*, J. Fluid Mech., 7 (1960).

[51] E. PITTS AND B. GREILLER, *The flow of thin liquid films between rollers*, J. Fluid Mech., 11 (1961).

[52] F. PRANCKH AND L. SCRIVEN, *Elastohydrodynamics of blade coating*, AIChE J., 36 (1990).

[53] E. RØNQUIST, *Optimal spectral elements methods for the unsteady three-dimensional incompressible Navier-Stokes equations*, PhD thesis, Massachusetts Institute of Technology, 1988.

[54] E. RØNQUIST, *A domain decomposition method for elliptic boundary value problems: Application to unsteady incompressible fluid flow*, in Proccedings of the Fifth Conference on Domain Decomposition Methods for Partial Differential Equations, Norfolk, Virginia, 1991.

[55] K. RUSCHAK, *Limiting flow in a pre-metered coating device*, Chem. Eng. Sci., 31 (1976), pp. 1057–1060.

[56] ——, *A method for incorporating free boundaries with surface tension in finite element fluid flow simulators*, Int. J. Num. Meth. Eng., 15 (1980).

[57] ——, *Boundary conditions a a liquid/air interface in lubrications flows*, J. Fluid Mech., 119 (1982).

[58] ——, *A three-dimensional linear stability analysis for two dimensional free boundary flows by the finite element method*, Comp. Fluids, 11 (1983), p. 391.

[59] K. RUSCHAK, *Coating flows*, Ann. Rev. Fluid Mech., 17 (1985), pp. 65–89.

[60] P. G. SAFFMAN, *Viscous fingering in hele-shaw cells*, J. Fluid Mech., 173 (1986), pp. 73–94.

[61] P. G. SAFFMAN AND G. I. TAYLOR, *The penetration of a fluid into a porous medium or hele-shaw cell containing a more viscous liquid*, Proc. R. Soc. of London, A245 (1958).

[62] M. SAVAGE, *Cavitation in lubrication*, J. Fluid Mech., 80 (1977).

[63] M. SAVAGE, *Mathematical models for coating processes*, J. Fluid Mech., 117 (1982), pp. 443–55.

[64] G. STRANG AND G. J. FIX, *An Analysis of the Finite Element Method*, Prentice-Hall, 1973.

[65] G. I. TAYLOR, *Deposition of a viscous fluid on the wall of a tube*, J. Fluid Mech., 7 (1960).

[66] G. I. TAYLOR, *Cavitation of a viscous fluid in narrow passages*, J. Fluid Mech., 14 (1963).

[67] K. TSIVERIOTIS AND R. BROWN, *Boundary-conforming mapping applied to computations of highly deformed solidification interfaces*, Int. J. Num. Meth. Fluids, 14 (1992), pp. 981–1003.

[68] F. WANG AND G. DOMOTO, *Free surface taylor vortices*, J. Fluid Mech., 261 (1994).

[69] S. WEINSTEIN, E. DUSSAN V., AND L. UNGAR, *A theoretical study of two-phase flow through a narrow gap with a moving contact line: viscous fingering in a hele-shaw cell*, J. Fluid Mech., 221 (1990), pp. 53–76.